VOLUME 12 NUMBER 3-4 2025 ISSN 2409-6121; eISSN 2522-1361

Physical Sciences and Technology

National Nanotechnological Laboratory of Open Type
Institute of Experimental and Theoretical Physics

Physical Sciences and Technology is publishing two number in a year by al-Farabi Kazakh National University, al-Farabi ave., 71, 050040, Almaty, the Republic of Kazakhstan
website: http://phst.kaznu.kz/

Any inquiry for subscriptions should be send to:
Dr. Gauhar Mussabek, al-Farabi Kazakh National University
al-Farabi ave., 71, 050040, Almaty, the Republic of Kazakhstan
e-mail: journal.phst@gmail.com

SCOPE AND AIM

Physical Sciences and Technology provides an original paperback for the publication of peerreviewed research and review articles in all fields of Physics and related Technology. The topics, included in the scope, especially emphasize understanding of the physics underlying modern technology.

Subject areas may include, but are not limited to the following fields: Astronomy and Space Research, Theoretical Physics and Astrophysics, Plasma Physics and Related Technology, Chemical Physics and Related Technology, Condensed Matter Physics and Related Technology, Thermal physics and Related Technology, Nuclear Physics and Related Technology, Nanomaterials and Nanotechnology, Applied Atomic and Molecular Physics, Material Sciences and Related Technology, Electronics and Related Technology, Instrumentation, Photonics and Quantum Electronics, Signal processing.

The Journal is issued under the auspices of the National Nanotechnological Laboratory of Open Type and Institute of Experimental and Theoretical Physics and is published two times a year by the «Kazakh University» Publishing House. The International Editorial Board of the Journal consists of leading researchers from different countries of the world. The Journal is wide open for contributions that both lie at the far frontiers of contemporary physics and are particularly aimed at applications of the scientific principles of physics to modern technological problems.

IRSTI 29.19.22 https://doi.org/10.26577/phst20251221

Plasma treatment for producing hydrophobic and hydrophilic coatings on fabric surfaces

B.A. Kyrykbay[1, 2*], S.S. Ussenkhan[1, 2], Zh.E. Onaibergenov[2], N.E. Akhanova[1], A.U. Utegenov[2, 3] and S.A. Orazbayev[2, 3]

[1]Kazakh-British Technical University, Almaty, Kazakhstan
[2]Institute of Applied Sciences and Information Technologies, Almaty, Kazakhstan
[3]Al-Farabi Kazakh National University, Almaty, Kazakhstan
*e-mail: baglankyrykbaj44@gmail.com

(Received April 7, 2025; received in revised form September 15, 2025; accepted October 30, 2025)

This study examines the formation of hydrophilic and superhydrophobic surfaces using atmospheric-pressure plasma jets, with a particular emphasis on developing durable waterproof coatings for textile materials. The effects of plasma treatment on the structural and chemical properties of the substrates were analyzed, along with the influence of key technological parameters such as discharge power and the composition of the plasma-forming gas. Argon (Ar) was used as the primary plasma gas, while hexamethyldisiloxane (HMDSO) vapor served as the precursor for hydrophobic coating formation. Surface hydrophilicity was evaluated after one and ten treatment cycles using Ar plasma at a flow rate of 40 mL/s and a discharge power of 200 W. Superhydrophobic coatings were produced under similar plasma conditions, with a gas mixture of Ar + HMDSO introduced at 20 mL/min. Contact angle measurements were performed to assess changes in wettability and to quantify the hydrophilic or superhydrophobic character of the treated surfaces. The results demonstrate that plasma treatment enables effective tuning of surface hydrophobicity and that the resulting coatings exhibit stable performance when exposed to various liquids.

Keywords: surface treatments, liquid-solid interfaces, superhydrophobic, hydrophilic, fabric.
PACS number(s): (81.65.-b), (68.08.-p).

1. Introduction

In recent years, plasma technologies have attracted increasing attention due to their numerous advantages. Unlike traditional surface modification methods, plasma treatment does not require the use of liquid reagents and does not generate wastewater, making it an environmentally friendly approach. Moreover, the application of non-polymerizing plasma enhances the adhesion properties of materials and increases their hydrophilicity [1].

Significant advancements in atmospheric-pressure plasma processing technologies [2] have opened new opportunities for industrial implementation, making such processes more competitive compared to vacuum plasma methods [3]. These improvements enable processing under conditions typical of standard production equipment, without the need for vacuum generation or the use of expensive reactive gases such as argon or carbon tetrafluoride [4-8].

The application of plasma technologies allows for targeted modification of surface characteristics, including adhesion, surface energy, and wettability. However, despite substantial progress in atmospheric-pressure plasma (APP) treatment [9], the development of effective methodologies based on a single plasma source remains a critical challenge. Most studies to date have focused on individual aspects of surface modification, highlighting the need for a comprehensive approach to understanding the mechanisms that regulate surface properties. Controlling surface wettability plays a key role in various technological processes, including textile production [10-12], packaging materials [13], biomedical hydrophobic coatings [14-16], and filtration systems [17]. One of the most promising surface modification methods is atmospheric-pressure plasma jet treatment, which enables changes in material hydrophilicity and hydrophobicity without the use of aggressive chemical reagents [18-20]. This method is characterized by

high efficiency, the ability to achieve localized effects, and environmental safety.

Despite the active development of this field, several challenges remain, including the durability of the obtained coatings [21-27], the optimization of processing parameters, and the adaptation of the technology for industrial applications. This study investigates the mechanisms of hydrophobic and hydrophilic surface formation using atmospheric-pressure plasma jets, evaluates the effects of treatment conditions on fabric properties, and analyzes the stability of modified materials under external influences. The results obtained may contribute to the development of innovative functional coatings for various industrial applications.

2. Experimental section

The experimental setup designed for the study of hydrophilic and superhydrophobic coatings obtained using a plasma jet based on a high-frequency discharge at atmospheric pressure is schematically presented in Figure 1. The formation of the plasma flow was carried out using an RF generator, which provided a discharge between a copper conductor, insulated with quartz glass, and a grounded copper plate. A quartz tube with a length of 100 mm, an inner diameter of 3 mm, and an outer diameter of 10 mm was used for plasma generation. The power source was a high-frequency generator Seren-R 301 operating at a frequency of 13.56 MHz. Argon (Ar) was used as the main gas supplied to the system, while hexamethyldisiloxane (Purity: ≥99.0%) was used as the precursor. Since HMDSO is in a liquid state at room temperature, its dosing was performed through a bubbler. Gas flow regulation was ensured by a mass flow controller.

Main provision: In this study, hydrophilic and hydrophobic coatings were formed using a radio-frequency discharge method at atmospheric pressure. An analysis of their wetting properties was performed, and the dynamics of changes in coating characteristics during operation were examined. At a fixed power of the setup, the degree of hydrophilicity and hydrophobicity was tested in various experimental cycles, and the stability of the coatings on fabrics was evaluated under exposure to different types of liquids.

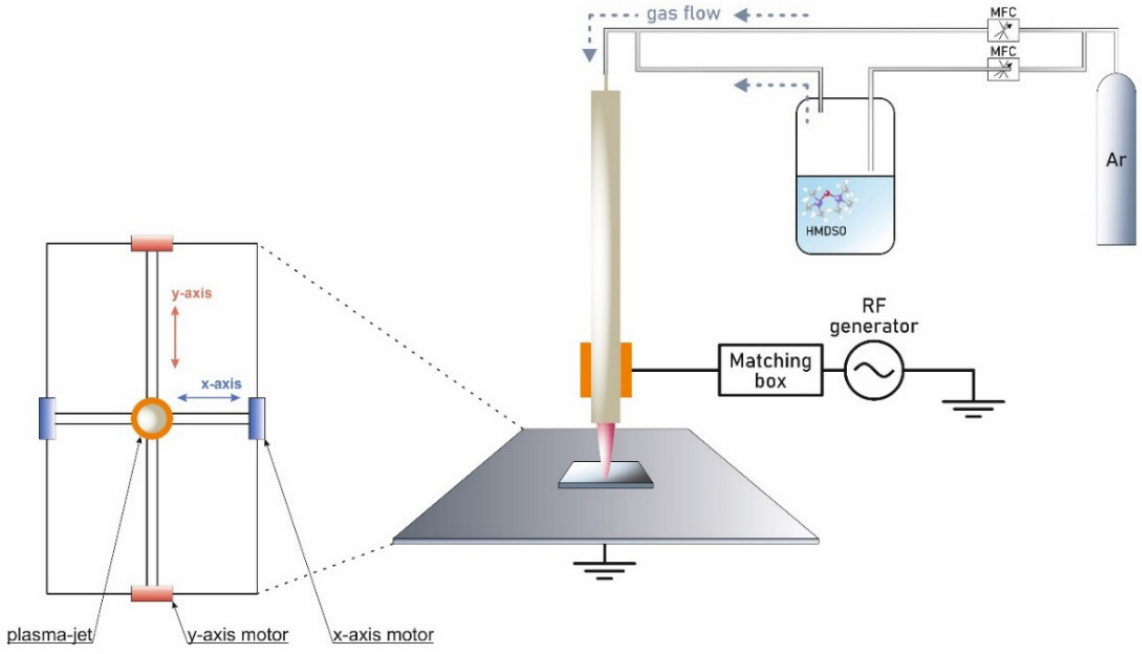

Figure 1 – Scheme of experimental setup.

3. Results an discussion

Experiments were conducted to determine the optimal conditions for the formation of hydrophilic and superhydrophobic coatings. In the initial stage, argon (Ar) was used as the sole gas medium to obtain hydrophilic surfaces. The dependence of the contact angle on the number of plasma treatment cycles was studied under the following parameters: a discharge power of 200 W, a pulse frequency of 1000 Hz, an Ar flow rate of 40 cm³/s, and a number of cycles ranging from 1 to 10. Figure 2a presents a graph of the relationship between the number of cycles and the contact angle. It was established that as the number of cycles increased, the treated surface exhibited more pronounced hydrophilic properties. This can be explained by the fact that prolonged exposure to argon plasma enhances hydrophilicity due to the removal of organic contaminants, surface activation, and an increase in the concentration of polar functional groups resulting from interactions with active plasma species.

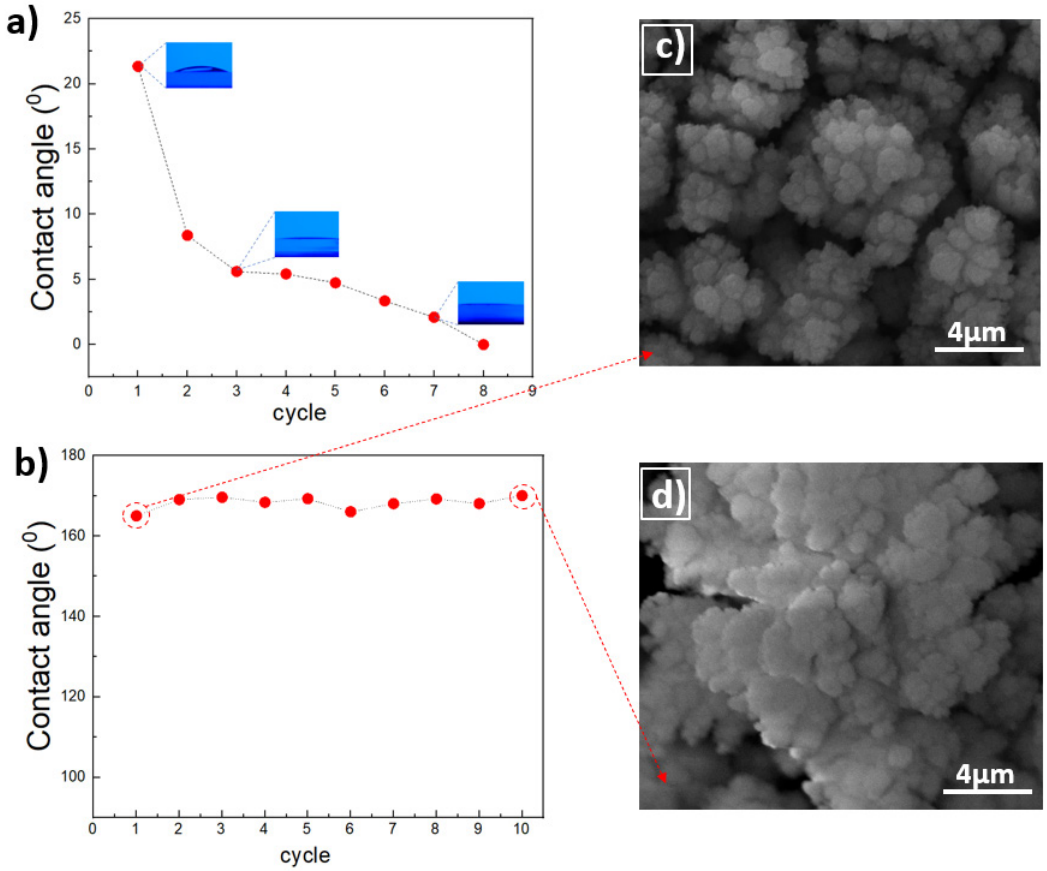

Figure 2 – Graphs of the dependence of the number of cycles for hydrophilic (a) and superhydrophobic (b) surfaces. SEM images of superhydrophobic coating after one (c) and ten (d) cycles.

In the study of the superhydrophobic properties of the coatings, the following parameters were used: a discharge power of 200 W, a pulse frequency of 1000 Hz, a primary argon flow rate of 40 cm³/s, a secondary gas flow rate (Ar + HMDSO) of 20 cm³/min, and exposure at room temperature. The effect of the number of deposition cycles on the contact angle was investigated. Varying the number of deposition cycles from 1 to 10 (Figure 2b) showed that the contact angle increased from 164.25° to 171.35° with an increasing number of cycles. Thus, a single deposition cycle is sufficient to form a superhydrophobic coating. To assess the characteristics of the coating formed as a result of the interaction of precursors on the surface of a glass sample with a plasma flow after one (Figure 2c) and ten (Figure 2d) cycles, the morphological properties were analyzed. The morphology of the synthesized coatings

was examined using a scanning electron microscope (SEM). The obtained data showed that the formed particles have various shapes, including spherical ones.

The effectiveness of modifying the surface properties of synthetic fabrics using atmospheric-pressure plasma treatment technology was further investigated. Synthetic fabrics were used as substrates, onto which a superhydrophobic coating was subsequently applied. As a result of the treatment, the water contact angle of the surface reached 157.16° (Figure 3a), indicating a significant reduction in wettability and a transition of the material from a hydrophilic to a superhydrophobic state.

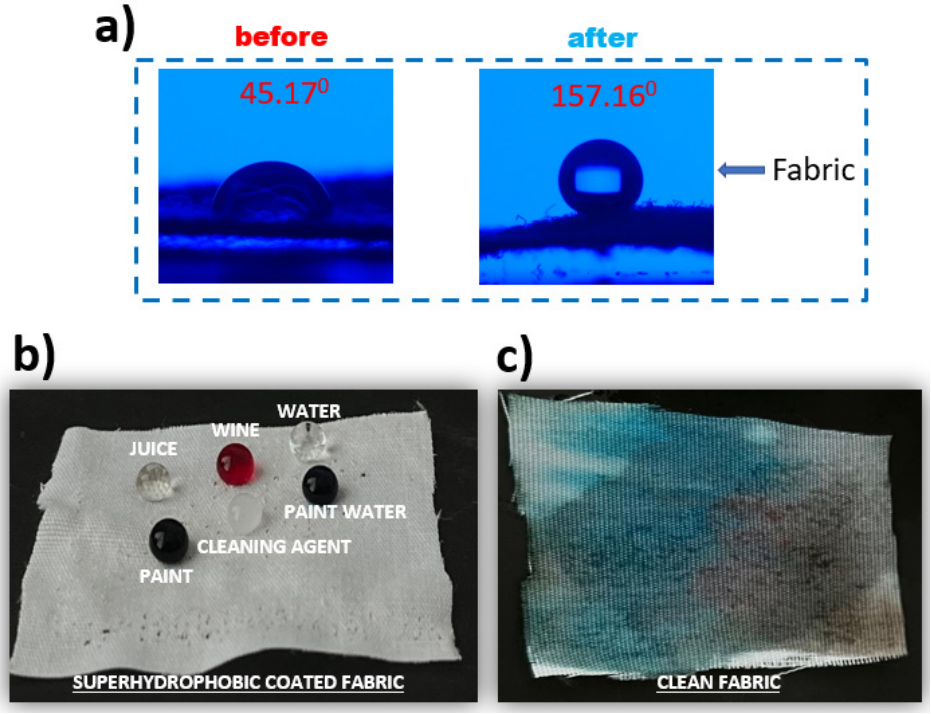

Figure 3 – Water contact angle on fabric coated with a superhydrophobic layer compared to plain clean fabric (a). Interaction of various types of liquids on fabric with a superhydrophobic coating (b) and clean fabric (c).

To evaluate the effectiveness of the obtained coating, experiments were conducted by applying various liquids to treated and untreated fabric samples. The tests demonstrated that the high contact angle promotes the formation of a superhydrophobic layer, preventing surface wetting (Figure 3b). In contrast, on untreated fabrics, liquid substances easily penetrated the material's structure, leaving stains that hindered reuse and led to significant cleaning costs (Figure 3c).

Thus, the obtained results demonstrate the high efficiency of atmospheric-pressure plasma treatment for creating superhydrophobic coatings on textile materials. This technology has potential applications in various fields, including the production of water-repellent clothing, protective coatings for textiles, and medical and industrial textiles requiring resistance to contamination and moisture.

4. Conclusion

This study investigates the formation of hydrophilic and superhydrophobic coatings using radio-frequency (RF) plasma discharge at atmospheric pressure. The wettability of modified surfaces was analyzed, and the durability of the obtained coatings under various conditions was evaluated. The results showed that increasing the number of plasma treatment cycles enhances hydrophilic properties by removing organic contaminants and activating the surface, thereby promoting the formation of polar functional groups. Conversely, the deposition of low-surface-energy compounds led to the formation of superhydrophobic coatings, with contact angles reaching 171.35° after multiple deposition cycles.

The study also examined the effectiveness of plasma treatment for modifying synthetic textile sur-

faces, achieving a significant reduction in wettability, with a water contact angle of 157.16°. The treated materials demonstrated strong resistance to liquid penetration, preventing staining and enabling self-cleaning. Comparative tests confirmed that untreated fabrics readily absorb liquids, whereas plasma-modified textiles effectively repel them.

These findings highlight the potential of atmospheric-pressure plasma treatment as an efficient and environmentally friendly method for controlling surface wettability without the use of hazardous chemicals. The ability to precisely tailor hydrophilic and hydrophobic properties through plasma treatment opens new opportunities for various industrial applications, including waterproof textiles, protective coatings for packaging materials, biomedical coatings, and filtration systems. Further research is needed to optimize treatment parameters to enhance coating durability and to evaluate large-scale implementation strategies for industrial applications.

Acknowledgements. All authors are grateful to the Committee of Science of the Ministry of Science and Higher Education of the Republic of Kazakhstan (No. BR21882187, No. BR27197639).

References

1. Sundriyal P., Sahu M., Prakash O., Bhattacharya S. Long-term surface modification of PEEK polymer using plasma and PEG silane treatment // Surfaces and Interfaces. – 2021. – Vol. 25. – Art. 101235. https://doi.org/10.1016/j.surfin.2021.101253

2. Hagger O. S. J., Parkes M. A., Estrin F. L., Agrotis S., Parkin I. P., Handoko A. D., Caruana D. J. Additive metal printing on multi materials using an atmospheric pressure plasma jet on a 5-Axis platform // Materials & Design. – 2025. – Art. 113681. https://doi.org/10.1016/j.matdes.2025.113681

3. Vesel A., Macovei A., Balestrazzi A., Tondepu S. A. G., Dueñas Jr C., Locato V., Tonto T. C., Zoani C., Lojen D., Primc G., Zaplotnik R., Ogrinc N., Lehocky M., Mozetič M. Hydrophilization of rice seeds by plasma treatments – Super-hydrophilic surface finish and hydrophobic recovery // Applied Surface Science. – 2025. – Vol. 691. – Art. 162674. https://doi.org/10.1016/j.apsusc.2025.162674

4. Chien S.-W., Chau S.-W., Živný O., Jeništa J., Chen S.-H. Modelling of thermal plasma-assisted carbon tetrafluoride abatement // Journal of Cleaner Production. – 2024. – Vol. 434. – Art. 139952. https://doi.org/10.1016/j.jclepro.2023.139952

5. Ismaylov B. K., Zikrillayev N. F., Ismailov K. A., Kenzhaev Z. T. Clusters of impurity nickel atoms and their migration in the crystal lattice of silicon // Physical Sciences and Technology. – 2023. – Vol. 10, No. 1–2. – Pp. 13–18. https://doi.org/10.26577/phst.2023.v10.i1.02

6. Mussabek G. K., Yermukhamed D., Dikhanbayev K. K., Mathur S., Sivakov V. A. Self-organization growth of Ge-nanocolumns // Materials Research Express. – 2017. – Vol. 4. – Art. 035003. https://doi.org/10.1088/2053-1591/aa5ed6

7. Akatan K., Battalova A., Sagiyeva N., Kabdrakhmanova S., Kaiyrbekov N., Tursyngazykyzy A., Shaymardan E., Beisebekov M., Kampitova G. Oxidized starch/CMC based biofilm: Synthesis and characterization // Physical Sciences and Technology. – 2024. – Vol. 11, No. 1–2. -Pp. 58-63. https://doi.org/10.26577/phst2024v11i1a7

8. Abdirakhmanov A., Dauylbayeva M., Kyrykbay B., Baikaliyev A., Orazbayev S., Utegenov A., Gabdullin M., Ramazanov T., Batryshev D. The formation of chondrule-like particles in RF discharge plasma // Physical Sciences and Technology. – 2023. – Vol. 10, No. 3–4. – Pp. 68–72. https://doi.org/10.26577/phst.2023.v10.i2.08

9. Yuan Y., Wang Y., Liu S., Zhang X., Liu X., Sun C., Yuan D., Zhang Y., Cao X. Direct chemical vapor deposition synthesis of graphene super-hydrophobic transparent glass // Vacuum. – 2022. – Art. 111136. https://doi.org/10.1016/j.vacuum.2022.111136

10. Chen C., Jia X., Li X., Shi M., Hu J., Song M., Wu S., Dai H., Wang X., Geng H. Scalable wet-spinning of wearable chitosan-silica textile for all-day radiative cooling // Chemical Engineering Journal. – 2023. – Vol. 457. – Art. 146307. https://doi.org/10.1016/j.cej.2023.146307

11. Orazbayev S., Zhumadilov R., Zhunisbekov A., Gabdullin M., Yerlanuly Y., Utegenov A., Ramazanov T. Superhydrophobic carbonous surfaces production by PECVD methods // Applied Surface Science. – 2020. – Vol. 515. – Art. 146050. https://doi.org/10.1016/j.apsusc.2020.146050

12. Solihat N. N., Purwanti T., Husna N., Oktaviani M., Zulfiana D., Fatriasari W., Nawawi D. S. Capability lignin from Acacia crassicarpa black liquor as an environmentally benign antibacterial agent to produce antibacterial and hydrophobic textiles // Bioresource Technology. – 2024. – Vol. 413. – Art. 131409. https://doi.org/10.1016/j.biortech.2024.131409

13. Mathew A., Poulose A., Peter A., Lal H. M., Uthaman A., Saheed M. S. M., Pasquini D., Grohens Y., Gopakumar D. A., George J. J. Bio-inspired hydrophobicity in cellulose nanopaper via thermal-induced phase separation of beeswax: A new strategy to develop sustainable food packaging materials and its service life prediction // Food Packaging and Shelf Life. – 2025. – Vol. 48. – Art. 101461. https://doi.org/10.1016/j.fpsl.2025.101461

14. Somvanshi S. B., Kharat P. B., Khedkar M. V., Jadhav K. M. Hydrophobic to hydrophilic surface transformation of nanoscale zinc ferrite via oleic acid coating: Magnetic hyperthermia study towards biomedical applications // Ceramics International. – 2020. – Vol. 46. – Pp. 7642–7653. https://doi.org/10.1016/j.ceramint.2019.11.265

15. Mussabek G., Diyuk V.E., Zaderko A.N., Afonin S., Baktygerey S., Taurbayev Ye., Yermukhamed D., Zhylkybayeva N., Yessengereyeva N., Lisnyak V.V. Thermal fluorination of nanoporous activated carbon mediated by freons // Diamond and Related Materials. -2025. -Vol. 155. P.112197. https://doi.org/10.1016/j.diamond.2025.112197

16. Rahman A. U., Kabeb S. M., Zulfkifli F. H. Functional hydrophobic coatings: Insight into mechanisms and industrial applications // Progress in Organic Coatings. – 2025. – Vol. 203. – Art. 109187. https://doi.org/10.1016/j.porgcoat.2025.109187

17. Wei N., Yang F., Zhao Y., Tian H., Jin Y., Kumar R. Environmentally friendly zein/ethylcellulose nanofiber air filtration materials with tunable hydrophobicity and high filtration efficiency // International Journal of Biological Macromolecules. – 2025. – Vol. 290. – Art. 139014. https://doi.org/10.1016/j.ijbiomac.2024.139014

18. Du J., Wu P., Kou H., Gao P., Cao Y., Jing L., Wang S., Rusinov P., Zhang C. Self-healing superhydrophobic coating with durability based on EP + PDMS/SiO_2 double-layer structure design // Progress in Organic Coatings. – 2024. – Vol. 190. – Art. 108359. https://doi.org/10.1016/j.porgcoat.2024.108359

19. Yang S.-H., Liu C.-H., Su C.-H., Chen H. Atmospheric-pressure plasma deposition of SiOx films for super-hydrophobic application // Thin Solid Films. – 2009. – Vol. 517, – No. 17. – Pp. 5284–5287. https://doi.org/10.1016/j.tsf.2009.03.083

20. Sun J., Wang J., Xu W., Zhang B. A mechanically robust superhydrophobic corrosion resistant coating with self-healing capability // Materials & Design. – 2024. – Vol. 240. –Art. 112881. https://doi.org/10.1016/j.matdes.2024.112881

21. Kyrykbay B. A., Abdirakhmanov A. R., Ussenkhan S. S., Utegenov A. U., Yerlanuly Y., Ramazanov T. S., Koshtybayev T. B., Orazbayev S. A. Obtaining hydrophobic coatings from Ar+HMDSO using radiofrequency discharge at atmospheric pressure // International Journal of Mathematics and Physics. – 2024. – Vol. 15, – No. 1. – Pp. 77–82. https://doi.org/10.26577/ijmph.2024v15i1a9

22. Przystupa K. Research on the durability and reliability of industrial layered coatings on metal substrate due to abrasive wear // Materials. – 2023. – Vol. 16. -No. 5. – Art. 1779. https://doi.org/10.3390/ma16051779

23. Kravchenko I. N., Zhachkin S. Y., Timashov E. P. et al. Effect of plasma deposition production parameters on protective and functional coating formation // Refractories and Industrial Ceramics. – 2023. – Vol. 64. – Pp. 388–392. https://doi.org/10.1007/s11148-024-00858-w

24. Rakhadilov B., Bayatanova L., Kengesbekov A., Magazov N., Toleukhanova Z., Yeskermessov D. Study of the influence of air plasma spraying parameters on the structure, corrosion resistance, and tribological characteristics of Fe–Al–Cr intermetallic coatings // Coatings. – 2025. – Vol. 15, No. 7. – P. 790. https://doi.org/10.3390/coatings15070790

25. Munteanu C., Melnic I., Istrate B., Hardiman M., Gaiginschi L., Lupu F. C., Arsenoaia V. N., Chicet D. L., Zirnescu C., Badiul V. A comprehensive review of improving the durability properties of agricultural harrow discs by atmospheric plasma spraying (APS) // Coatings. – 2025. – Vol. 15, No. 6. – Art. 632. https://doi.org/10.3390/coatings15060632

26. Nenastina T., Sakhnenko M., Oskak S., Yar-Mukhamedova G., Zellele D., Mussabek G., Imanbayeva A. Study of complexation patterns in the system Ni_2+, MoO_4^{2-}, $P_2O_7^{4-}$, Cit^{3-} for the development of poly-ligand electrolytes // Eurasian Chem.-Technol. J. -2024. -Vol. 26. -P. 155-160. https://doi.org/10.18321/ectj1638

27. Avcı A., Karabaş M., Eker A. A. et al. Optimization of laser process parameters and improved corrosion behaviour of LZ/YSZ thermal barrier coating // Journal of the Australian Ceramic Society. – 2025. – Vol. 61. – P. 1155–1171. https://doi.org/10.1007/s41779-025-01149-4

Information about authors:

Baglan A. Kyrykbay (corresponding author) – Master of Science, Researcher at the Kazakh-British Technical University (Almaty, Kazakhstan, e-mail: baglankyrykbaj44@gmail.com).

Sultan S. Ussenkhan – Master of Science, Researcher at the Institute of Applied Sciences and Information Technologies (Almaty, Kazakhstan, e-mail: sultan@physics.kz).

Zhanserik Ongaibergenov – Researcher at the Institute of Applied Sciences and Information Technologies (Almaty, Kazakhstan, e-mail: onajbergenovz@gmail.com).

Akhanova Nazim Yerlanovna – PhD, Acting Vice-Rector for Science and Innovation/Director of the Department of Science and Innovation at the Kazakh-British Technical University (Almaty, Kazakhstan, e-mail: n.akhanova@kbtu.kz).

Almasbek U. Utegenov – PhD, Associate Professor at the Department of Plasma Physics, Nanotechnology, and Computational Physics, Al-Farabi Kazakh National University (Almaty, Kazakhstan, e-mail: almasbek@physics.kz).

Sagi A. Orazbayev – PhD, Associate Professor at the Department of Plasma Physics, Nanotechnology, and Computational Physics, Al-Farabi Kazakh National University (Almaty, Kazakhstan, e-mail: sagi.orazbayev@gmail.com).

IRSTI 31.15.13 https://doi.org/10.26577/phst20251222

Highly efficient copper–palladium nanoalloy catalysts on modified carbon supports

M.K. Skakov[1], A. Amirov[2*], A.K. Kabdrakhmanova[2, 3, 4], N. Toshkuvatova[5], A.T. Khalmanov[6], A.Zh. Miniyazov[1], V.V. Baklanov[1], Y.T. Koyanbayev[1], N.M. Mukhamedova[1], G.K. Zhanbolatova[1], K. Pramod[7] and A. Shakeel[8, 9]

[1]Institute of Atomic Energy, Branch RSE NNC RK, Kurchatov, Kazakhstan
[2]Satbayev University, Almaty, Kazakhstan
[3]Scientific Research Institute "TrueScience", Almaty, Kazakhstan
[4]LLP "SciCom", Astana, Kazakhstan
[5]Samarkand State University named after Sh. Rashidov, Samarkand, Uzbekistan
[6]Samarkand State University of Architecture and Construction named after Mirzo Ulugbek, Samarkand, Uzbekistan
[7]School of Nanoscience and Nanotechnology, Mahatma Gandhi University, Kottayam, India
[8]Postgraduate Department of Chemistry, Government Postgraduate College Rajouri, Jammu and Kashmir, India
[9]Higher Education Department, Government of Jammu and Kashmir, Jammu, India
*e-mail: alseit.amirov@gmail.com

(Received September 22, 2025; received in revised form November 13, 2025; accepted November 19, 2025)

Catalytic systems were made using Cu, Pd, and Pd-Cu nanoparticles (NPs) supported on modified activated carbon (ACm) of BAU-A grade, which had been modified with hydrochloric acid, for dehydrochlorination of chlorobenzene and 1,2-dichlorobenzene. Based on previous studies, the optimal content of metal NPs in the heterogeneous catalysts for the transformation of mono- and dichlorobenzene organochlorine pollutants utilizing the method of catalytic dehydrochlorination were determined to be: 5% for Pd; 10% for Cu; and, 3% Pd and 7% Cu for the bimetallic variant. The metal NPs were determined to bond to the carboxyl and carbonyl functional groups of the ACm. The characteristics of the catalysts were studied using FTIR spectroscopy, differential thermogravimetric analysis, scanning electron microscopy and ad-sorption porosimetry. Finally, following dehydrochlorination, a chromatograph mass spectrometer was used to identify the products. These results on the pore structures of the catalysts demonstrate good development, allowing for an increased number of sites to adsorb persistent organic pollutants (POPs). Whereas all the catalysts showed effectiveness in dehydrochlorination of chlorobenzene and 1,2-dichlorobenzene, separately, into benzene, the bimetallic catalyst, 3Pd-7Cu/ACm, demonstrates the best results, with conversion rates of 93.94% and 89.79%, respectively.

Keywords: hydrodechlorination, copper nanoparticles, palladium nanoparticles (NPs), catalysis, bimetallic catalyst, organochlorine compounds, modified carbon, persistent organic pollutants (POPs).
PACS number(s): 82.65.+r, 68.43.–h, 81.05.U–, 82.20.–w, 81.07.–b.

1. Introduction

Halogen-containing organic compounds are extensively utilized in various industries and by consumers, serving as coolants, medicines and their delivery systems, solvents, and plasticizers, and many other applications. Due to their high toxicity and chemical stability, numerous halogenated organic compounds are identified as persistent organic pollutants (POPs). Consequently, many of these compounds are banned by the World Health Organization (WHO). On May 22, 2001, the Stockholm Convention on Persistent Organic Pollutants was signed. This agreement aims to reduce and eventually eliminate existing stocks of POPs, as well as to cease the production, use, and release of any new POPs [1]. The currently accumulated reserves of excessively produced halogen-containing by-products require environmentally safe handling. This necessitates the development of new methods for their conversion and disposal. Modern methods

of neutralizing waste containing POPs utilize reductive dechlorination. This process can be optimized to save more re-sources by using new types of nanocaalysts that regenerate the hydrocarbon component of halogenated molecules [2].

The development of reductive methods for the dechlorination of organohalogen compounds is facilitated by the search for active, selective, and efficient catalysts. Several studies have demonstrated that catalysts based on palladium (Pd) and platinum (Pt) exhibit the highest activity and selectivity in the reductive transformation of chlorine-containing compounds [3-7]. This is attributed to their capacity to facilitate the separation of H_2, thereby promoting the cleavage of the C–Cl bond [8]. Many studies have been devoted to the analysis of catalysts based on Pd and Pt for the electrocatalytic reduction of halogenated, specifically chlorine-containing, organic compounds. Typically, the content of Pd and Pt in such catalysts reaches 10% by weight [9-12]. However, the utilization of noble metals increases the cost of catalysts and thus, the entire process. In recent years, there has been a trend to alleviate the cost of catalysts by diluting or substituting these expensive noble metals with others that are more economical yet still exhibit acceptable characteristics.

Carbon carriers are highly promising for catalytic applications due to their purity, exceptional porous structure, and high specific surface area [13]. Activated carbon (AC), in particular, is extensively utilized as a carrier material in the synthesis of catalysts aimed at recycling persistent organic pollutants (POPs) [14-17]. Granular activated carbon (GAC) combined with bimetallic Pd and Fe nanoparticles (NPs) was used for the simultaneous adsorption and dehalogenation of polychlorinated biphenyl (PCB) [17]. For this purpose, the pore volume of granular activated carbon is impregnated with a solution of Fe (III) nitrate Fe(NO3)3, followed by heat treatment at a temperature of 3000C. Subsequent reduction with sodium borohydride (NaBH4) leads to the formation of zerovalent (ZVI) Fe0, with Fe NPs sizes in the range of 7-40 nm. Afterwards, the reduced Pd solution (Pd(CH3CO2)2 is added to the surface of Fe NPs. As a result, small stable Fe NPs of 6-12 nm in size are formed in the mesopores of the granular AC, on which a 2-3 nm Pd nanolayer has been uniformly dis-tributed. The GAC/ZVI/Pd system demonstrated 90% efficiency in the dechlorination of 2-chlorobiphenyl to form the reaction product biphenyl. In previous studies, the hydrodechlorination of organohalogen substances with Pd catalysts supported on coal-based material was 80-100% [18-22]. Some researchers developed na-nosized palladium catalysts for the reductive dechlorination of PCBs, achieving this at low temperatures and with a minimal amount of catalyst [23-26]. Fifteen PCB congeners, including monochlorinated (PCB 1, PCB 2), dichlorinated (PCB 4, PCB 5, PCB 7, PCB 9, PCB 10, PCB 11, PCB 12, PCB 14, PCB 15), trichlorinated (PCB 29), tetrachlorinated (PCB 77), pentachlorinated (PCB 126), and hexachlorinated (PCB 169), under-went complete decomposition. This process resulted in a 100% yield of biphenyl using 10% Pd/C–Et3N as a catalyst [27]. In this case, the reductive dechlorination of PCBs was carried out at room temperature in MeOH, with bottled hydrogen as a reducing agent, Pd (10%)/C, and Et3N. 2.5 mg of catalyst was consumed per 25 mg of PCB.

Despite the high catalytic activity of palladium, the high cost of noble metals limits the large-scale production of these catalysts. Recently, copper nanoparticles (Cu NPs) have garnered significant interest in the devel-opment of new catalytic systems due to their high activity and selectivity [28, 33-35]. A study on copper catalysts, with metal contents ranging from 0.5% to 5.0% (wt.), demonstrated the significant impact of the carrier material on alachlor conversion, achieving conversion rates ranging from 85.2% to 92.9% [34]. A catalytic system utilizing copper nanoparticles (Cu NPs) stabilized with polyvinylpyrrolidone (PVPD40) and deposited onto an activated carbon (AC) substrate achieved a chlorobenzene conversion rate of 94.46% [14].

Considering that Cu catalysts for hydrodechlorination have very often been used in conjunction with noble metals, the high conversion rate of alachlor hydrodechlorination is an interesting result from the point of view of scaling [29-32].

Compared to previously reported Pd–Cu catalytic systems, the novelty of this work lies in the use of a Cu-rich composition, which makes it possible to significantly reduce the amount of expensive noble metal without loss of catalytic efficiency. Additionally, the application of HCl-modified wood-based activated carbon as a support is an important distinguishing factor, since chemical modification increases the number of oxygen-containing functional groups and improves the interaction of the metal nanoparticles with the surface, which can promote the formation of more homogeneous and stable Pd–Cu nanoalloys. These two factors together – optimized Pd/Cu ratios and targeted chemical modification of the carbon carrier – create conditions for enhanced Pd–Cu synergy and demonstrate that high hydrodechlorination efficiency can be achieved not only by increasing

Pd loading, but also by engineering the support and nanoalloy composition.

This study focuses on the synthesis and investigation of the physical and chemical properties of Cu, Pd, and Pd-Cu catalysts to evaluate their effectiveness in the liquid-phase hydrodechlorination of mono- and dichlorobenzenes.

2. Materials and Methods

2.1. Materials

In this study, the following reagents were used: copper (II) nitrate $Cu(NO_3)_2 \cdot 3H_2O$ (99.9%), palladium(II) chloride $PdCl_2$ (99.9%), sodium tetrahydroborate $NaBH_4$ (99.9%), sodium hydroxide NaOH, chlorobenzene C_6H_5Cl (99.5%), and 1,2-dichlorobenzene $C_6H_4Cl_2$ (99%). All reagents were purchased from Sigma Aldrich and used without additional purification. As a catalyst support, commercial wood-based activated carbon BAU-A (GOST 6217-74, Russia) was employed, which possessed the following characteristics: iodine adsorption activity of not less than 60%, ash content not exceeding 6%, and moisture content not exceeding 6%. For the modification of activated carbon, hydrochloric acid (GOST 11125-84, LLCMK MAGNA, Russia) was used according to the procedure described by Shaimardan et al [13].

2.2. Methods

2.2.1 Preparing the catalysts

In this study, the catalysts were synthesized using the wet impregnation method described by Hyeok et al. (Fig. 1) [32–34]. For the preparation of the Cu catalyst, 6.5 g of copper(II) nitrate was dissolved in 5 mL of deionized water, after which 10 g of AC_m was introduced into the solution and stirred vigorously for 10 minutes. The mixture was then placed in a desiccator for 4 hours to facilitate the sorption of Cu ions, followed by drying at 150 °C for 2 hours to remove excess water. To stabilize the Cu ions, the Cu^{2+}/ACm sample was calcined at 330°C for 4 hours. Subsequently, the reduction of Cu^{2+} in ACm was carried out by dissolving 1.6 g of sodium borohydride ($NaBH_4$) in 20 mL of distilled water. Subsequently, the $NaBH_4$ solution was added to a 50 mL aqueous-alcohol solution with a volume ratio of 30:70, and the mixture was stirred. To adjust the pH to ≤ 7, a 5 N NaOH solution was introduced. The $NaBH_4$ solution was slowly added to the Cu^{2+}/ACm suspension and stirred for 3 hours until the complete release of hydrogen. The resulting catalyst contained 10 wt.% of active Cu phase (10Cu/ACm).

The preparation of the Pd catalyst followed a similar procedure, where 20 mg of palladium (II) chloride was dissolved in 20 mL of an aqueous-alcoholic solution with a volume ratio of 30:70 (90% ethanol to water), and then mixed with 1 g of ACm under vigorous stirring. The obtained catalyst contained 5 wt.% of active Pd phase (5Pd/ACm). The bimetallic Pd–Cu catalyst was synthesized using the same procedure, with the difference that Pd^{2+}/ACm and Cu^{2+}/ACm suspensions were combined in a 3:7 ratio before the addition of the $NaBH_4$ solution. The final bimetallic catalyst contained 3 wt.% of active Pd phase and 7 wt.% of active Cu phase (3Pd–7Cu/ACm).

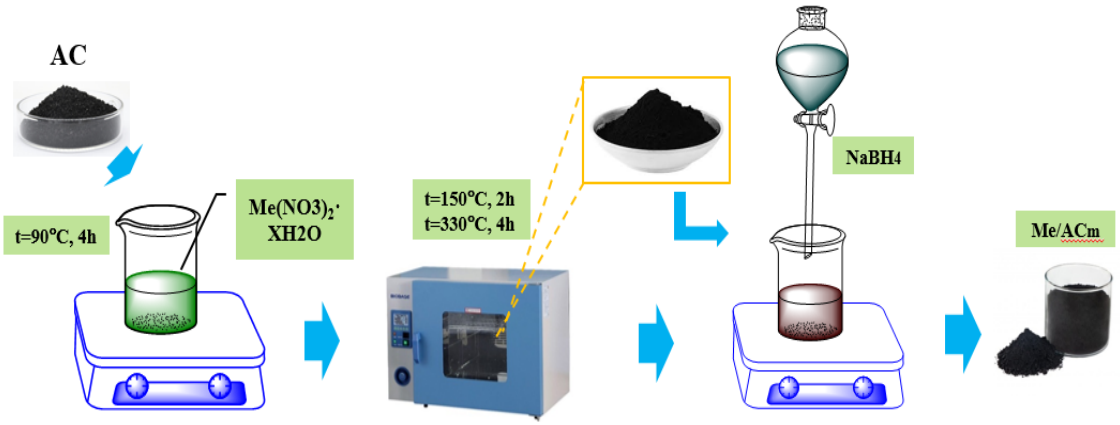

Figure 1 – Schematic for preparation of $10Cu/AC_m$, $5Pd/AC_m$ and3Pd-$7Cu/AC_m$ catalysts.---

2.2.2 FTIR analysis

Fourier-transform infrared (FTIR) spectroscopy was performed using an FTIR FT-801 spectrometer (Simex, Russia) with a resolution of 1 cm^{-1} in the range of 500–4000 cm^{-1}. Measurements were conducted at 25°C following the standard procedure, employing KBr pellets prepared at a 1:10 sample-to-KBr ratio. A total of 100 scans were collected for each spectrum. Prior to use, potassium bromide was finely ground and calcined at 200°C for 3 hours.

2.2.3 X-ray diffraction (XRD) analysis

The crystal structure of the samples was analyzed using an X'PertPRO diffractometer (Malvern Panalytical Empyrean, Netherlands) equipped with monochromatized CuKα radiation. Data were collected over the 2θ range of 10–45° with a step size of 0.02°. The operating conditions included an X-ray tube voltage of 45 kV, a current of 30 mA, and a counting time of 0.5 s per step.

2.2.4 Thermogravimetric analysis (TGA)

Thermal stability and decomposition behavior of the catalysts were investigated using an STA449C simultaneous thermal analyzer (NETZSCH, Germany) under an argon atmosphere. Measurements were conducted in the temperature range of 30–700°C with a heating rate of 10 ± 1°C/min. The initial sample mass was approximately 20 ± 2 mg.

2.2.5 Scanning and transmission electron microscopy (SEM and TEM)

The morphology and structure of the catalysts were characterized using a Crossbeam 540 high-vacuum scanning electron microscope (Zeiss, Germany). Elemental composition was determined by energy-dispersive X-ray spectroscopy (EDS, Thermo Fisher Scientific, USA). Transmission electron microscopy (TEM) images were obtained with a JEM-1400 microscope (JEOL, Japan), operating at an accelerating voltage of 120 kV, with a resolution of 0.38 nm, equipped with a Morada high-resolution CCD digital camera (Olympus, Japan). Prior to TEM, samples were ground in an agate mortar, dispersed in ethanol, and sonicated at 44 kHz using an UZDN-2T ultrasonic generator (Electron, Russia). A drop of the suspension was deposited on a perforated carbon-coated copper grid and dried before imaging. Particle size distributions and average particle diameters were determined statistically from TEM micrographs.

2.2.6 Adsorption porosimetry

Textural properties of the catalysts were determined by low-temperature nitrogen adsorption–desorption measurements using an Autosorb-1 analyzer (Quantachrome Instruments, USA). Before analysis, the samples were degassed under vacuum at 200–250°C for 3 hours. The Brunauer–Emmett–Teller (BET) method was applied to calculate specific surface area, with a measurement error of ±2.8%. Pore size distribution and total pore volume were derived from desorption isotherms using the Barrett–Joyner–Halenda (BJH) method.

2.2.7 Catalytic activity

Catalytic hydrodechlorination of chlorobenzene and 1,2-dichlorobenzene was carried out in an RVD-2-150 high-pressure reactor (Uoslab, Ukraine). The reaction mixture consisted of 1 mL of organochlorine compound, 0.1 g of catalyst, 3 mL of NaOH solution, and 1 mL of ethanol in a two-neck round-bottom flask [30]. Hydrogen gas was introduced at 50°C under 10 atm pressure, with magnetic stirring for 5 hours. After completion, the reaction mixture was washed with 10 mL of magnesium sulfate solution to precipitate sodium salts. A 1 mL aliquot of the treated solution was diluted with 19 mL of hexane for subsequent analysis.

2.2.8 Gas chromatography–mass spectrometry (GC–MS)

The hydrodechlorination products were analyzed using a 5975C GC/MS system (Agilent, USA) equipped with a GC–MSD quadrupole mass spectrometric detector (Agilent, USA). Operating conditions were as follows: electron ionization energy of 70 eV; HP-5MS quartz capillary column (30 m × 0.25 mm × 0.25 μm); helium as carrier gas; split ratio of 1:50; flow rate of 1.0 mL/min. The oven temperature program consisted of an initial temperature of 40°C (held for 3 min), followed by heating at 10°C/min to a maximum of 290°C, with a final holding time of 30 min.

3. Results and discussion

Physical and chemical characteristics of the 5Pd/ACm, 10Cu/ACm, and 3Pd–7Cu/ACm catalysts are presented below.

3.1. FTIR spectroscopy

In the FTIR spectra of 5Pd/AC_m, 10Cu/AC_m and 3Pd-7Cu/AC_m, in comparison to unmodified AC, the appearance of intense peaks in the region of 600-750 cm^{-1} and the absence of an absorption band in the region of 1713 cm^{-1}, related to C=O, are observed, which indicates a new bond in the catalysts, as seen in Figure 2.The data is in good agreement with previous studies. The most important difference in the FTIR spectra of the catalytic systems is the absence of the C=O vibration at 1713 cm^{-1}, which indicates the interaction of NPs and AC_m through the C–OH functional group.

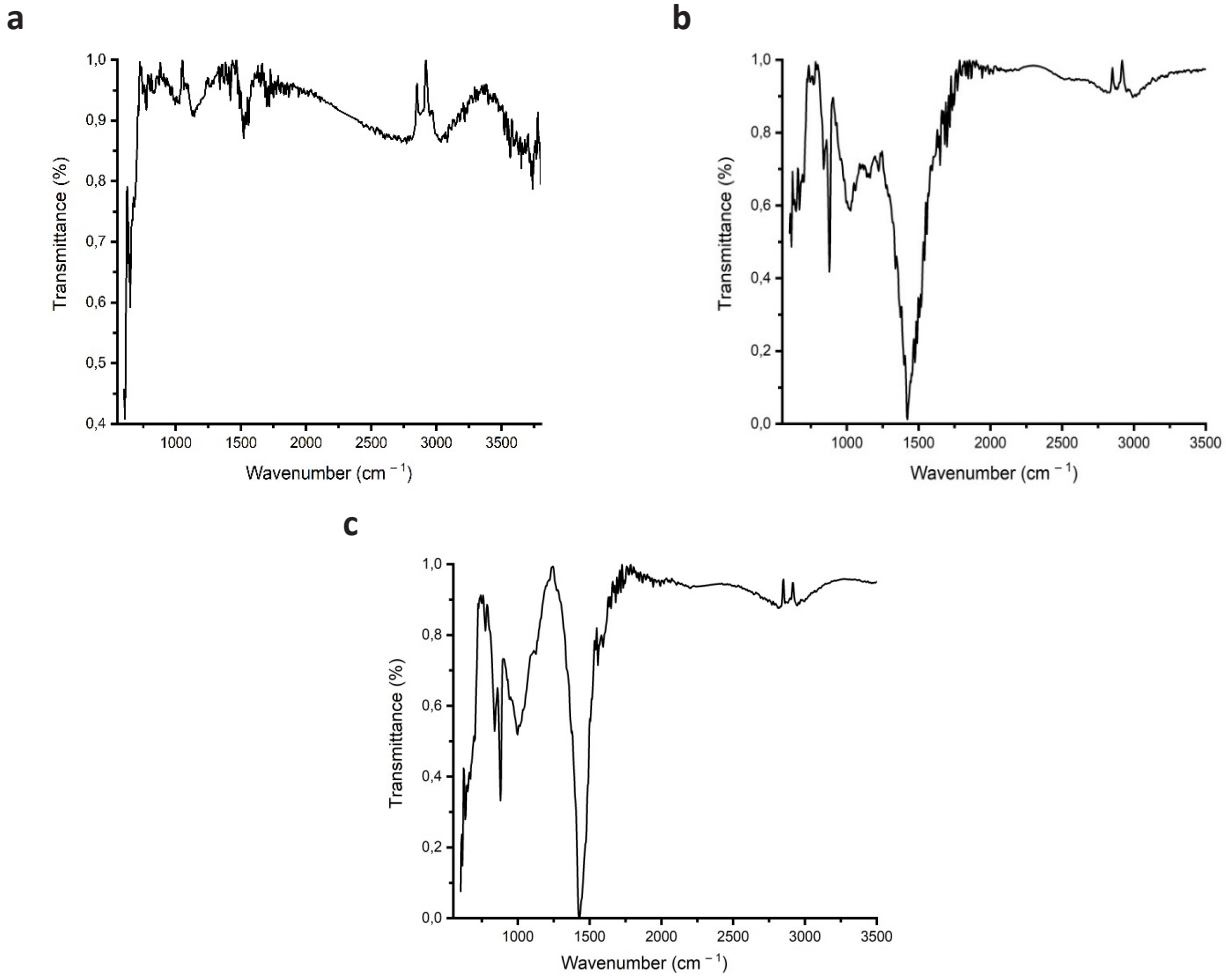

Figure 2 – The FTIR spectra of catalytic systems: a) 5Pd/AC_m; b) 10Cu/AC_m; and, c) 3Pd-7Cu/AC_m.

FTIR spectra demonstrate the disappearance of the C=O vibration at 1713 cm^{-1} together with the appearance of new bands in the 600–750 cm^{-1} region, which evidences chemical coordination of Pd and Cu nanoparticles specifically with carbonyl / carboxyl surface functionalities on ACm. XRD further confirms that the metals do not exist as independent separate phases: the presence of mixed reflections characteristic for Pd–Cu alloy formation shows that the two metals interact electronically at the atomic level, forming common crystallographic domains rather than isolated particles. Taken together, FTIR and XRD results indicate that the active phase is a true nanoalloy, strongly bonded to oxygen-containing anchoring sites of the HCl-modified carbon support, and this metal–metal–support coupling is the basis for the enhanced catalytic behavior observed.

3.2. XRD analysis

The X-ray diffraction (XRD) analysis of the 5Pd/AC_m catalyst reveals three distinct diffraction peaks at 2θ values of 23.6°, 43.5°, and 72.5°, which correspond to the Miller indices (003), (101), and (220), respectively. These peaks indicate that the catalyst exhibits a face-centered cubic lattice structure. This structural information is significant as it confirms the successful reduction of the $PdCl_2$ precursor to Pd NPs (Fig. 3, Table 1).

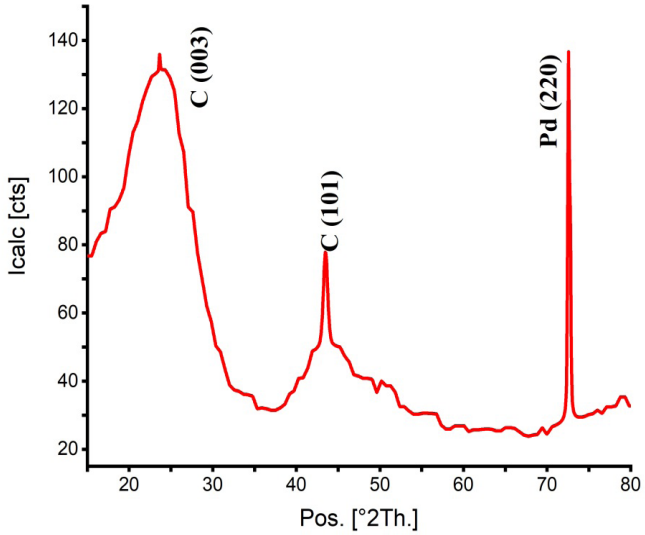

Figure 3 – X-ray diffraction pattern of 5Pd/AC_m catalyst.

Table 1 – Interplanar distance (d) of atoms in the 5Pd/AC_m catalyst.

Pos. [°2Th.]	Height [cts]	FWHM Left [°2Th.]	d-spacing [Å]	Rel. Int. [%]
23.6308	4.90	0.0900	3.76197	4.52
43.4566	19.83	0.5904	2.08245	18.31
72.5528	108.30	0.1968	1.30296	100.00

XRD analysis of 10Cu/AC_m revealed five diffraction peaks, with Miller indices at 2θ = 26.47 (020), 36.31 (111), 42.34 (121), 49.96 (020) and 72.58 (022) (Fig. 4, Table 2). The X-ray diffraction (XRD) pattern of the 10Cu/AC_m catalyst provides critical structural information. In the 2θ angle range of 50-80°, the pattern exhibits a series of reflections characteristic of a face-centered cubic (FCC) lattice, thereby confirming the presence of metallic copper (Cu). Additionally, in the 2θ angle range of 20-45°, the pattern reveals reflections indicative of cubic lattices, which demonstrate the presence of copper oxide (CuO).

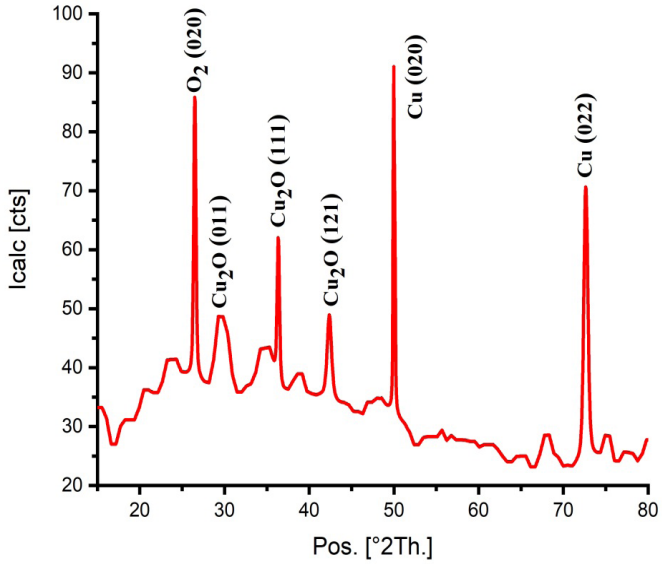

Figure 4 – X-ray diffraction pattern of 10Cu/AC_m catalyst.

Table 2 – Interplanar distance (d) of atoms in the 10Cu/AC_m catalyst.

Pos. [°2Th.]	Height [cts]	FWHM Left [°2Th.]	d-spacing [Å]	Rel. Int. [%]
26.4737	34.14	0.2952	3.36688	61.29
36.3197	17.76	0.2952	2.47358	31.89
42.3402	9.88	0.5904	2.13474	17.74
49.9641	55.70	0.1476	1.82542	100.00
72.5885	35.69	0.4920	1.30241	64.08

The crystal structure and phase characteristics of the 3Pd-7Cu/AC_m bimetallic catalyst are elucidated by five diffraction peaks, corresponding to the following Miller indices: 2θ = 26.49° (002), 36.88° (100), 43.14° (111), 62.51° (213), and 72.63° (022) (Fig.5, Table 3). The lattice parameter for palladium (Pd) is determined to be 3.36421 Å, which is closely aligned with the literature value of 3.890 Å. The copper (Cu) component exhibits a face-centered cubic (FCC) lattice, while the palladium (Pd) displays a hexagonal lattice structure. Moreover, the Pd-Cu alloy demonstrates a tetragonal lattice structure (Table 3).

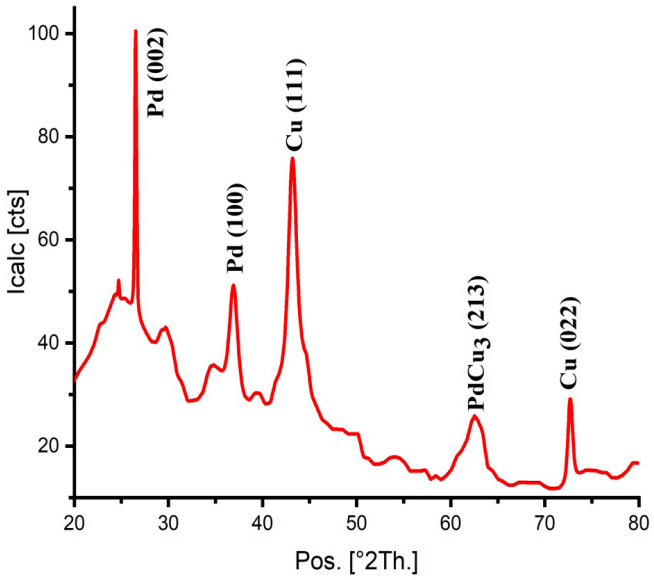

Figure 5 – X-ray diffractionof3Pd-7Cu/AC_m.

Table 3 – Interplanar distance (d) of atoms in the 3Pd-7Cu/AC_m catalyst.

Pos. [°2Th.]	Height [cts]	FWHM Left [°2Th.]	d-spacing [Å]	Rel. Int. [%]
26.4950	40.78	0.1968	3.36421	100.00
36.8896	14.00	0.9840	2.43666	34.32
43.1491	28.14	0.9840	2.09658	69.01
62.5193	0.79	0.0900	1.48444	1.94
72.6397	12.30	0.4920	1.30161	30.16

3.3. Thermogravimetric analysis

Thermogravimetric analysis established a sharp decrease in the mass of all samples of catalysts, which occurred in the temperature range of 30-130°C, due to the evaporation of surface adsorbed water (Fig. 6). Furthermore, gradual decrease in the mass of 5Pd/AC_m, 10Cu/AC_m and 3Pd-7Cu/AC_m was observed in the temperature range of 450-700°C, which was caused by the combustion of carbonaceous compounds (Figures 5a-d). The state of general equilibrium in the temperature range of 150-450^{0}C indicates the stability of the carboxyl, carbonyl and lactone groups, which is likely due to the interaction of metal ions with these specified functional groups.

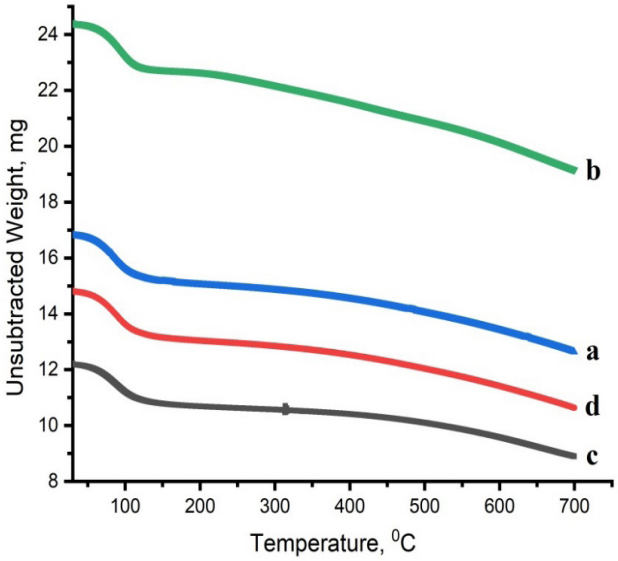

Figure 6 –TGA curves of AC_m alone and of the catalytic systems: a) AC_m; b) $5Pd/AC_m$; c) $10Cu/AC_m$; and, d) $3Pd\text{-}7Cu/AC_m$.

3.4. SEM and EDX analysis

Figures 6-8 present scanning electron micrographs of the $5Pd/AC_m$, $10Cu/AC_m$, and $3Pd\text{-}7Cu/AC_m$ catalysts. The $5Pd/AC_m$ catalyst exhibits a relatively smooth surface texture, spherical palladium nanoparticles (Pd NPs) with a uniform size distribution ranging from 18.04 to 19.50 nm (Fig. 7). Energy dispersive spectroscopy (EDX) analysis, integrated with SEM data, confirms that the palladium content in this catalyst is 3.9%.

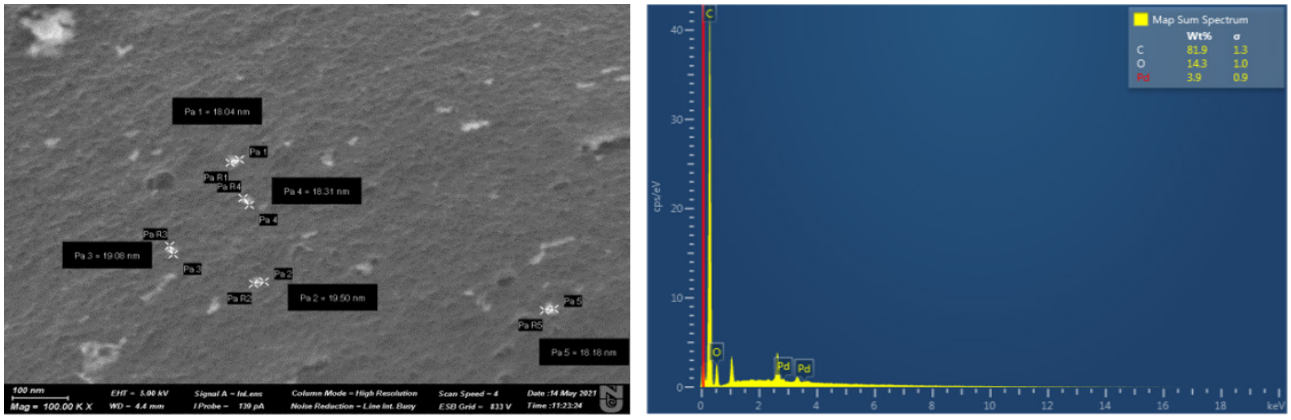

Figure 7 – SEM image and energy-dispersive X-ray (EDX) spectrum of the of $5Pd/AC_m$ catalyst.

In the 10Cu/AC$_m$ catalyst, SEM imaging reveals a rougher surface texture with copper nanoparticles (Cu NPs) ranging in size from 18.58 to 29.56 nm (Fig. 8). EDX data indicate a high carbon content of 79.9 wt.% and an oxygen content of 19.2 wt.%, while the copper content is measured at 10%

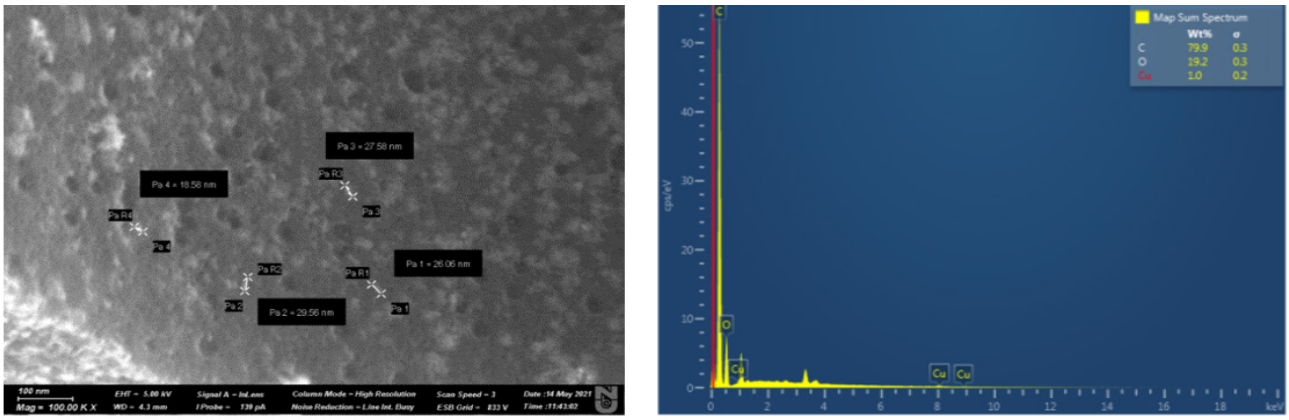

Figure 8 – SEM image and energy-dispersive X-ray (EDX) spectrum of the 10Cu/AC$_m$catalyst

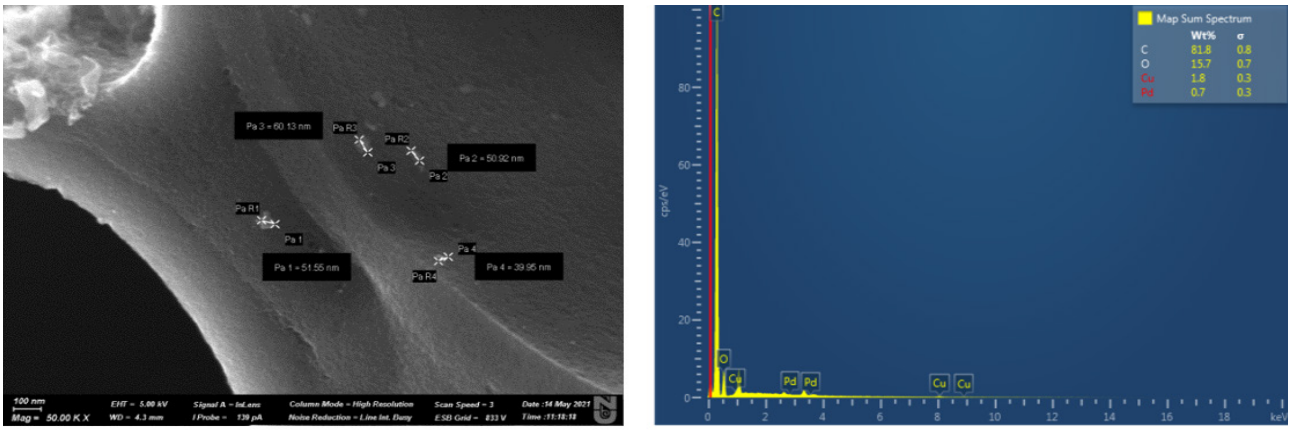

Figure 9 – SEM image and energy-dispersive X-ray (EDX) spectrum of the of 3Pd-7Cu/AC$_m$catalyst.

The 3Pd-7Cu/AC$_m$ bimetallic catalyst exhibits a more uniform texture compared to the monometallic catalysts, with particle sizes approximately twice as large, ranging from 39.95 to 60.13 nm (Fig. 9). EDX analysis confirms the presence of copper (Cu) and palladium (Pd) at concentrations of 1.8 wt.% and 0.7%, respectively. Figures 10-12 depict the TEM images of 5Pd/AC$_m$, 10Cu/AC$_m$, and 3Pd-7Cu/AC$_m$.

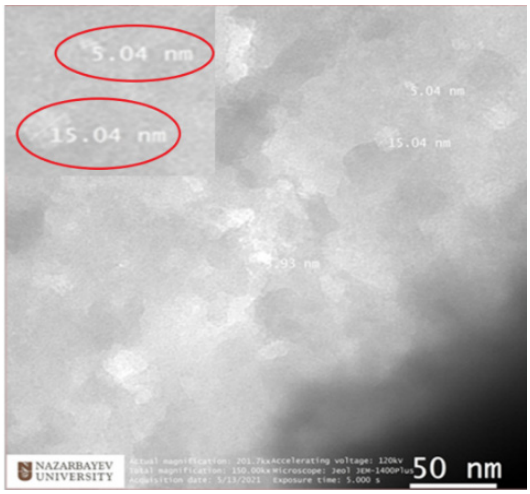

Figure 10 – TEM image of 5Pd/AC_m catalyst.

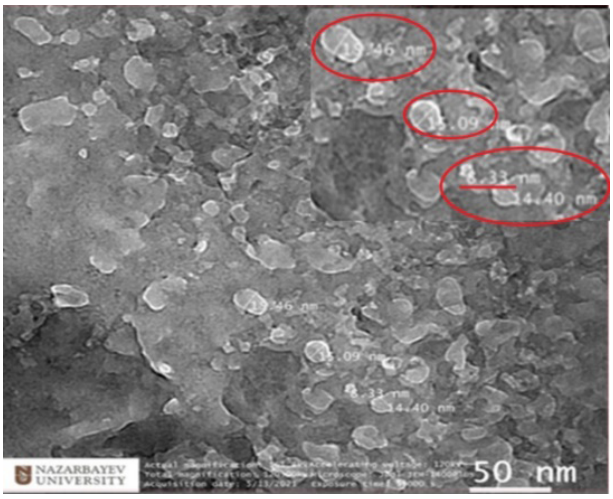

Figure 11 – TEM image of 10Cu/AC_mcatalyst.

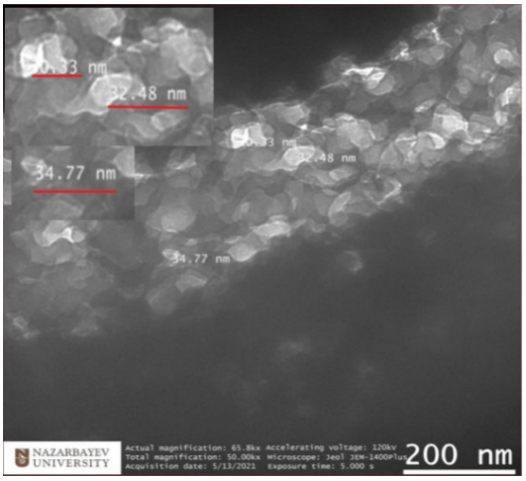

Figure 12 – TEM image of 3Pd-7Cu/AC_m catalyst.

3.5. TEM analysis

Transmission electron microscopy reveals that Pd nanoparticles form on the surface layer (Fig. 10) and exhibit diverse geometries and dimensions, ranging from 5 to 15 nm. The 10Cu/AC_m sample contains both small and large Cu nanoparticles, with sizes ranging from 8 to 19 nm, displaying various shapes and distributed uniformly across the entire surface of the catalyst (Fig. 11). The 3Pd-7Cu/AC_m bimetallic catalyst features larger nanoparticles in the range of 30 to 34 nm, which aggregate to form agglomerates (Fig. 12).

3.6. BET analysis

Table 4 shows the indicators of the specific surface area of AC_m alone and the three catalytic systems, calculated using the multipoint BET method, including the total pore volume and characteristics of the micropores. Further, the pore size distribution, surface area, and nitrogen adsorption-desorption isotherms of the catalytic systems are shown in Figures 13-14.

The catalysts synthesized exhibit a specific surface area ranging from 371.4 to 672.1 m²/g, which is 1.6 to 2.9 times higher than that of the AC_m support (Table 4). Additionally, there is a notable reduction in pore size accompanied by a substantial increase in total pore volume. Upon incorporation of Pd nanoparticles into the modified carrier, the specific surface area reaches 371.4 m²/g. In contrast, catalysts containing Cu nanoparticles show a specific surface area twice as large as that of Pd, at approximately 672.1 m²/g. The 3Pd-7Cu/AC_m catalytic system demonstrates a significant nearly two-fold increase in

specific pore surface area compared to the modified carrier (Table 4), consistent with findings from prior research [12]. All catalysts exhibit an increase in total pore volume, measured at 36.6, 73.9, and 65.6 ml/g for 5Pd/AC_m, 10Cu/AC_m, and 3Pd-7Cu/AC_m, respectively, indicating a well-developed porous structure. This expansion suggests an enhanced capability for adsorbing pollutants due to an increase in available adsorption sites. The pore sizes (Dv(r)) of the catalysts is seen to have decreased by 6.37-6.4 times, as compared to those of the AC_m carrier [12]. The order of reduction is: 10Cu/AC_m>3Pd-7Cu/AC_m>5Pd/AC_m (Table 4). The increase in the specific surface area and pore volume of all the catalysts is accompanied by a corresponding decrease in pore size, which is in the range of 19.084 nm, 19.168 nm and 19.070 nm for 5Pd/AC_m, 10Cu/AC_m and 3Pd-7Cu/AC_m, respectively, as compared to the carrier [12] (Table 4). This result may be due to the localization of Pd, Cu and Pd-Cu inside the pores of AC_m.

Table 4 – Specific surface area, size, total pore volume of AC_m; 5Pd/AC_m,; 10Cu/AC_m; 3Pd-7Cu/AC_m.

Sample	Surface area, m^2/g	Poresize, nm	Porevolume, ml/g
AC_m[12]	233.8	122.1	0.19
5Pd/AC_m	371.4	19.0	36.6
10Cu/AC_m	672.1	19.1	73.9
3Pd-7Cu/AC_m	600.4	19.07	65.6

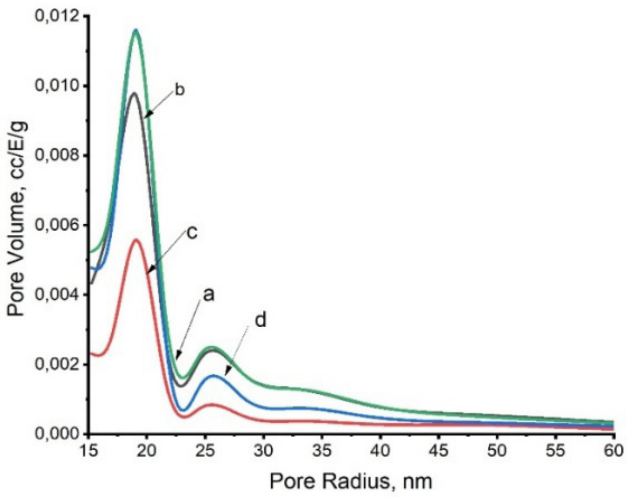

Figure 13 – Pore size distribution of different catalysts:
a) AC_m; b) 5Pd/AC_m; c) 10Cu/AC_m; and, d) 3Pd-7Cu/AC_m.

Further examination of the textural properties of the synthesized catalysts reveals distinct pore structures compared to the AC_m carrier (Fig. 13). The N_2 adsorption isotherm for all catalysts exhibits a type IV behavior, characterized by rapid and uniform nitrogen adsorption. The initial curves of these isotherms indicate the presence of micropores in all samples. At higher P/Po values, a slight capillary condensation appears on the isotherm, accompanied by a characteristic H4-type hysteresis loop. The pronounced wide hysteresis loop, classified as type IV according to IUPAC guidelines, reaffirms the uniform pore size and mesoporous nature of the materials.

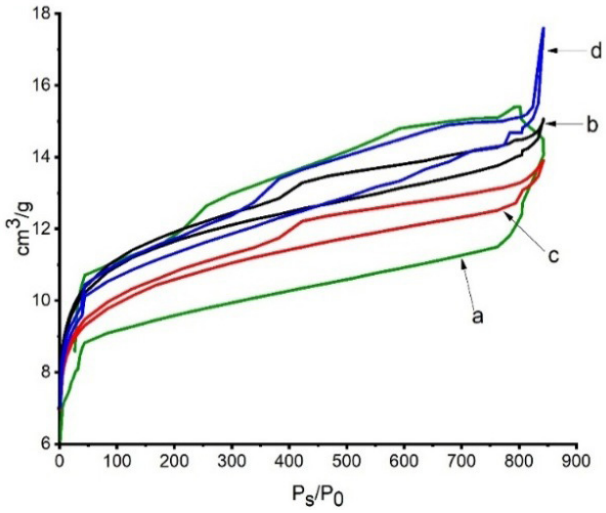

Figure 14 – N_2 adsorption-desorption isotherms of catalysts: a) AC_m; b) $5Pd/AC_m$; c) $10Cu/AC_m$; and d) $3Pd\text{-}7Cu/AC_m$.

3.7. Catalytic hydrodechlorination of chlorobenzene and 1,2-dichlorobenzene

The $5Pd/AC_m$, $10Cu/AC_m$ and $3Pd\text{-}7Cu/AC_m$ catalysts were tested using the model hydrodechlorination reactions of chlorobenzene and 1,2-dichlorobenzene, separately, in 10 ml ethanol, at a temperature of 50^0C and P_{H2} of 10 atm, over a period of 5 hrs. The data on the catalytic activity for the neutralization of the organohalogen substances are given in Table 5 and Figures 15-17.

Table 5 – Hydrodechlorination of chlorobenzene and 1,2-dichlorobenzene, using the $5Pd/AC_m$, $10Cu/AC_m$ and $3Pd\text{-}7Cu/AC_m$ catalysts.

Sample	Chlorobenzene		1,2-dichlorobenzene	
	Conversionproduct	Conversion, %	Conversionproduct	Conversion, %
$5Pd/AC_m$	Benzene	82,90	Benzene	86,74
$10Cu/AC_m$	Benzene	70,20	Benzene	80,30
$3Pd\text{-}7Cu/AC_m$	Benzene	93,94	Benzene	89,79

To further contextualize these results, Table 6 compares the catalytic performance of the 3Pd–7Cu/ACm catalyst with representative Pd-Cu based systems previously reported in the literature. This comparative overview clearly demonstrates that the Cu-rich 3Pd–7Cu/ACm composition provides competitive or even superior hydrodechlorination activity, while maintaining significantly lower Pd loading.

Table 6 – Comparison of hydrodechlorination performance of Pd–Cu catalysts with previously reported systems.

Catalyst System	Metal Loading (wt%)	Support Type	Chlorobenzene Conversion (%)	1,2-Dichlorobenzene Conversion (%)	Main Products	Findings
3Pd–7Cu/ ACm	3 Pd, 7 Cu	HCl-modified activated carbon	93.94	89.79	Benzene	Highest conversions with reduced Pd loading due to Cu-rich nanoalloy and modified support

Continuation of the table

Catalyst System	Metal Loading (wt%)	Support Type	Chlorobenzene Conversion (%)	1,2-Dichlorobenzene Conversion (%)	Main Products	Findings
5Pd/ACm	5 Pd	HCl-modified activated carbon	82.90	86.74	Benzene	Monometallic Pd catalyst, moderate conversions
10Cu/ACm	10 Cu	HCl-modified activated carbon	70.20	80.30	Benzene	Cu catalyst shows lower conversion compared to Pd or bimetallic
Pd–Cu/ Coal-Based AC	~10 Pd	Coal-based activated carbon	80–100	-	-	Previously reported high activity with higher Pd content
Pd–Fe/ GAC	Pd ~2-3 nm layer on Fe NPs	Granular activated carbon	~90 for PCB	-	Biphenyl	Bimetallic Pd-Fe catalysis, complex synthesis
Pd/C-Et3N	10 Pd	Modified carbon (triethylamine)	100 for PCB	-	Biphenyl	Complete decomposition of PCBs; high Pd loading
Cu/PVP–AC	~5 Cu	AC stabilized with PVP	94.46	-	Benzene	Copper-only catalyst with stabilizer shows high conversion
Pd/C (various)	10 Pd	Various activated carbons	80–100	-	Various	Widely studied Pd catalysts for hydrodechlorination with high activity

3.8. Gas chromatography-mass spectrometry analysis

The conversion of chlorobenzene through hydrodechlorination using 5Pd/AC_m, 10Cu/AC_m and 3Pd-7Cu/AC_m is 82.9%, 70.20 and 93.94%, respectively (Table 5, Figures 14a-16a). Hydrodechlorination of 1,2-dichlorobenzene using 5Pd/AC_m, 10Cu/AC_m and 3Pd-7Cu/AC_m is 86.74%, 80.30% and 89.79%, respectively (Table 5, Figures 14b-16b). In both cases, the conversion product was benzene. The bimetallic catalyst, 3Pd-7Cu/AC_m, showed the greatest activity in the hydrodechlorination of both organohalogens, with a conversion rate of 93.94% and 89.79%, respectively. The order of increasing catalytic activity in the hydrodechlorination of organohalogen substances is 10Cu/AC_m<3Pd/AC_m<3Pd-7Cu/AC_m.

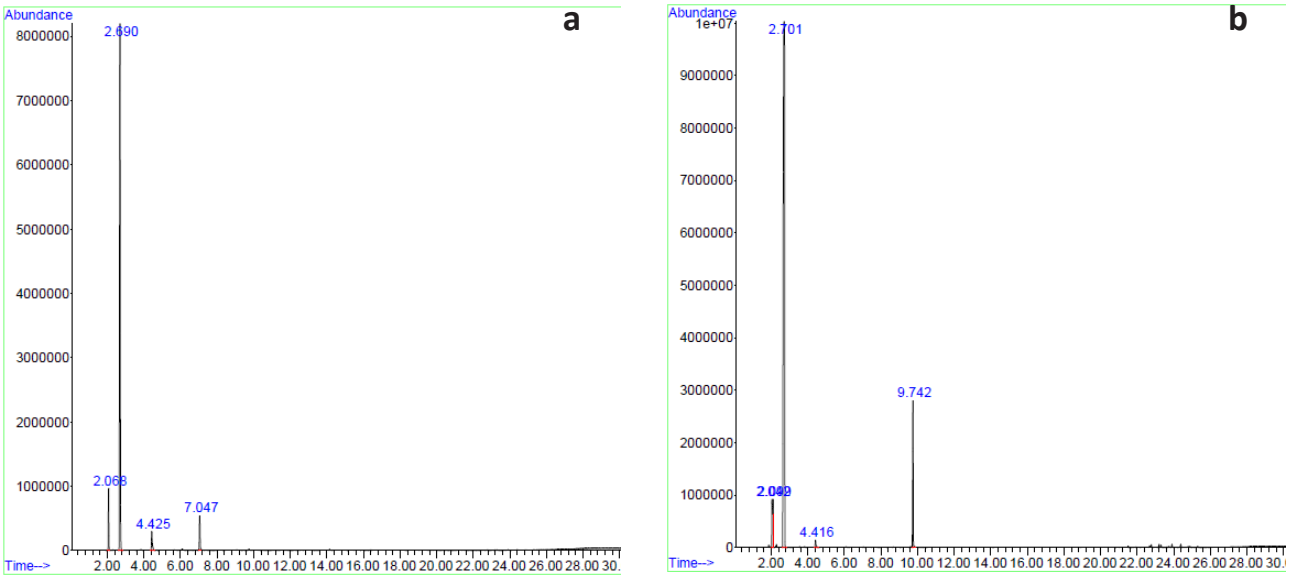

Figure 15 – Chromatogram of the hydrodechlorination products of:
a) chlorobenzene; b) 1,2-dichlorobenzene, using 5Pd/AC_m (10 mg) at a temperature of 50^{0}C.

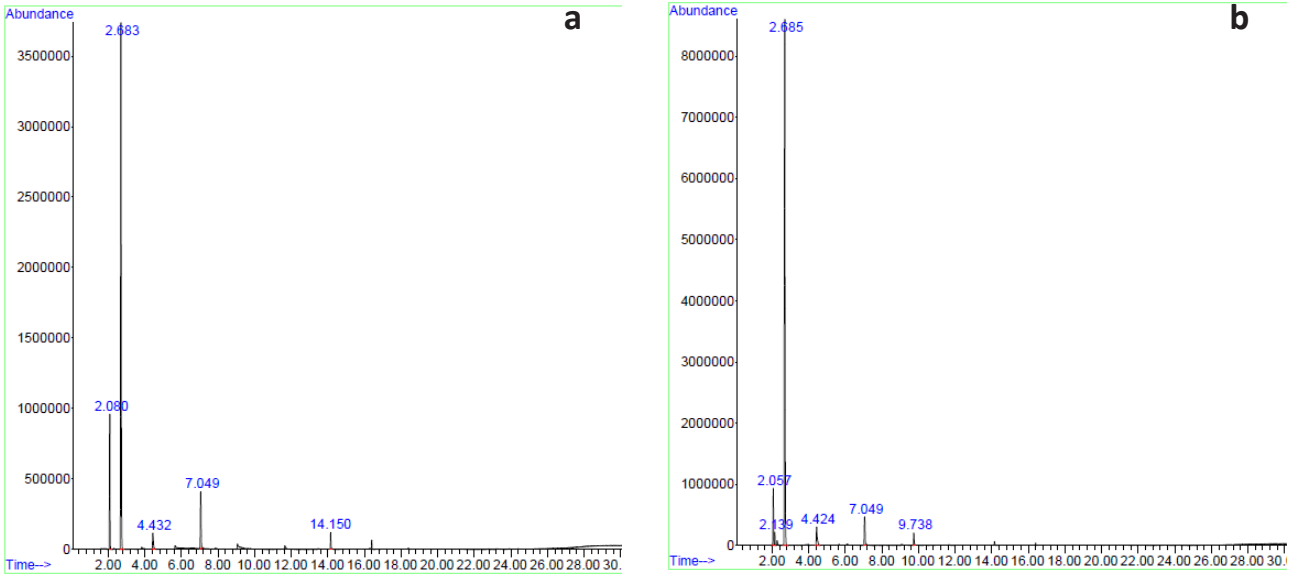

Figure 16 – Chromatogram of the hydrodechlorination products of:
a) chlorobenzene; b) 1,2-dichlorobenzene, using 10Cu/AC_m catalyst (10.0 mg) at a temperature of 50^0C.

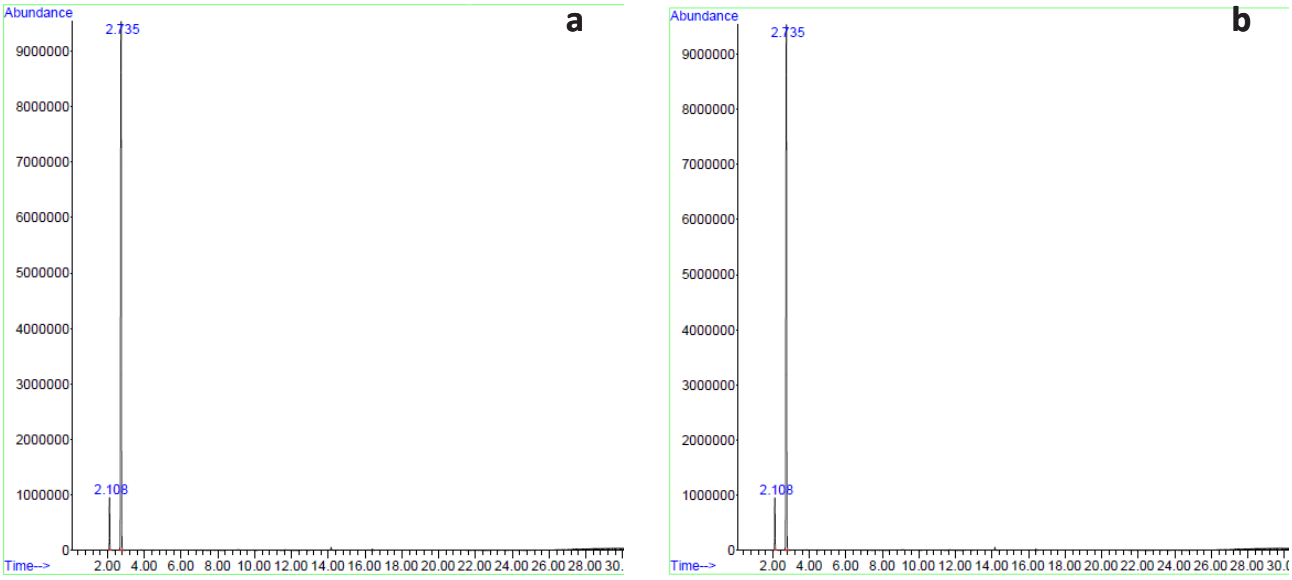

Figure 17 – Chromatogram of the hydrodechlorination products of:
a) chlorobenzene; b) 1,2-dichlorobenzene, using 3Pd-7Cu/AC_m catalyst (10 mg) at a temperature of 50^0C.

4. Conclusions

Three dehydrochlorination catalysts were synthesized on modified activated carbon (AC_m), using Pd and Cu nanoparticles (NPs), both alone and as a bimetal. Based on prior research, the following combinations were selected, using estimations of both cost and effectiveness: 5% Pd (5Pd/AC_m), 10% Cu (10Cu/AC_m), and 3% Pd with 7% Cu (3Pd-7Cu/AC_m). As per FTIR, TGA and EDX analyses, the NPs are able to connect with the AC_m carrier at the carboxyl and carbonyl functional groups. The pore sizes of the resulting catalysts have a range of 19.070 to 19,168 nm, which is 100 times smaller than that of the AC_m carrier alone. Further, the surface areas of the catalysts were found to be in the range of 371.748 to 672,132 m^2/g, which is 1.6-2.9 times higher than that of AC_m. These results on the pore structures of the catalysts demonstrate good development, allowing for an increased number of sites to adsorb persistent organic

pollutants (POPs). Whereas all the catalysts showed effectiveness in dehydrochlorinating chlorobenzene and 1,2-dichlorobenzene, separately, into benzene, the bimetallic catalyst, 3Pd-7Cu/AC_m, demonstrates the best results, with conversion rates of 93.94% and 89.79%, respectively.

The usage of inexpensive metallic NPs, like Cu, as catalysts on an AC_m carrier allows for a reduction in the amount of more expensive materials, such as Pd. The need for efficient and cost-effective catalysts to decrease the number of POPs is of great importance to all nations, especially in Kazakhstan, which faces serious problems created by both the industrial and agricultural sectors regarding POPs. This is in accordance with the WHO Convention on Persistent Organic Pollutants, which targets the reduction of both existing and future halogenated organic compounds. Furthermore, as Kazakhstan is already known for its petroleum production, the use of new types of nanocatalysts that regenerate the hydrocarbon component of halogenated molecules can create a synergistic relationship among the petroleum, agricultural, chemical and research sectors of the country. Finally, the current research team hopes to particularly find opportunities for this technology in the cleanup of hazardous areas that have been negatively affected by both past and recent application of halogenated organic compounds.

A deeper mechanistic explanation of the catalytic pathway can be formulated by considering the specific roles of Pd, Cu, and the HCl-modified carbon surface. According to our FTIR results, both Pd and Cu nanoparticles are bound to carboxyl and carbonyl functionalities of the modified activated carbon. This anchoring not only stabilizes the nanoparticles, but also electronically couples them to the support, creating an interface that facilitates H2 activation and stabilizes surface hydride species. XRD analysis confirms the formation of Pd–Cu alloy phases, which is a direct structural indicator of electronic interaction between the two metals at the atomic level. In Pd–Cu nanoalloys, the presence of Cu modifies the electronic density of Pd: electron donation from Cu to Pd shifts the d-band center of Pd to lower energy, which is known to weaken the Pd–Cl interaction. As a result, the C–Cl bond cleavage pathway becomes energetically more favorable, and surface poisoning by strongly adsorbed chlorides is reduced. Pd remains the primary site for H2 dissociation, while Cu facilitates electron transfer steps and stabilizes reactive intermediates, which together increases the overall turnover for hydrodechlorination. The modified carbon support additionally contributes by providing high surface area mesoporosity and a high density of oxygen-containing groups, which improves nanoparticle dispersion and suppresses sintering or growth during reaction.

Thus, the high activity of the 3Pd–7Cu/ACm catalyst can be explained mechanistically by the combination of (I) alloy-driven electronic tuning of Pd by Cu, (II) more efficient H_2 activation–transfer sequence at the bimetallic interface, and (III) stronger metal–support interactions induced by HCl modification of the carbon. These three effects act synergistically, and this explains why a Cu-rich formulation with reduced Pd loading can achieve higher conversion than monometallic Pd or Cu catalysts.

Acknowledgments. The authors would like to thank the management and staff of the Institute of Atomic Energy, Branch RSE NNC RK, Kurchatov, Kazakhstan, for providing the necessary infrastructure and resources for carrying out this research. The authors are also grateful to the Scientific Center of Composite Materials, Almaty, Kazakhstan, and Satbayev University, Almaty, Kazakhstan, for their technical support and contributions. Special thanks are extended to Mahatma Gandhi University, Kottayam, India, and Government Postgraduate College Rajouri, Jammu and Kashmir, India, for providing the facilities for material synthesis and analysis. The authors also appreciate the contribution of Mprex Healthcare Pvt., Ltd. Pune, India, for supplying the extract samples used in this study.

Funding. This research has been funded by the Science Committee of the Ministry of Science and Higher Education of the Republic of Kazakhstan (Grant No. BR21882200).

References

1. Stockholm Convention on Persistent Organic Pollutants (POPs) as amended in 2009. Text and An-nexes. – 2009. – P. 1–64. – Available at: https://www.pops.int/Portals/0/Convention%20text/UNEP-POPS-COP-CONVTEXT-2009.En.pdf (Available online on December 16, 2025).

2. Shaimardan E., Kabdrakhmanova S. K., Beisebekov M. M., Selenova B. S., Imangazinova Zh., Sydykbayeva S. Nickel nanocatalyst for hydrodechlorination of polychlorinated biphenyls // Bulletin of the National Nuclear Center of the Republic of Kazakhstan. – 2023. – Vol. 2. – Pp. 74–81. https://doi.org/10.52676/1729-7885-2023-2-74-81

3. Detlev F., Karsten K., Katrin M., Dieter K. F. Hydrodechlorination of chloroorganic compounds in ground water by palladium catalysts // Catalysis Today. – 2003. – Vol. 82. – Pp. 105–118. https://doi.org/10.1016/S0920-5861(03)00208-6

4. Castillo C., García-Muñoz P., Pérez-Ramírez J., Martín-Martínez F. Advances in hydrodechlorina-tion technologies for diclofenac removal: A comprehensive review // Molecules. – 2025. – Vol. 30, No. 16. – Art. 3332. https://doi.org/10.3390/molecules30163332

5. Urbano F. J., Marinas J. M. Hydrogenolysis of organohalogen compounds over palladium supported catalysts // Journal of Molecular Catalysis A: Chemical. – 2001. – Vol. 173, No. 1–2. – Pp. 329–345. https://doi.org/10.1016/S1381-1169(01)00157-1

6. de Pedro Z. M., Diaz E., Mohedano A. F., Casas J. A., Rodriguez J. J. Compared activity and stabil-ity of Pd/Al_2O_3 and Pd/AC catalysts in 4-chlorophenol hydrodechlorination in different pH media // Applied Catalysis B: Environmental. – 2011. – Vol. 103. – Pp. 128–135. https://doi.org/10.1016/j.apcatb.2011.01.018

7. Lan L., Liu Y., Liu S., Ma X., Li X., Dong Z., Xia C. Effect of the supports on catalytic activity of Pd catalysts for liquid-phase hydrodechlorination/hydrogenation reaction // Environmental Technology. – 2019. – Vol. 40, No. 12. – Pp. 1615–1623. https://doi.org/10.1080/09593330.2018.1426645

8. Keane A. M. Supported transition metal catalysts for hydrodechlorination reactions // ChemInform Abstract. – 2011. – Vol. 3. – Pp. 800–821. https://doi.org/10.1002/chin.201137243

9. Benítez L. J., Del A. G. Total hydrodechlorination of industrial transformer oil on metal-supported catalysts // Chemical Engineering Communications. – 2009. – Vol. 196, No. 10. – Pp. 1217–1226. https://doi.org/10.1080/00986440902831888

10. Janiak T., Janina O. Effectiveness and stability of commercial Pd/C catalysts in the hydrodechlo-rination of meta-substituted chlorobenzenes // Applied Catalysis B: Environmental. – 2009. – Vol. 92. – Pp. 384–392. https://doi.org/10.1016/j.apcatb.2009.08.018

11. Mitoma Y., Katayama Y., Simion C. Mechanistic considerations on the hydrodechlorination process of polychloroarenes // IntechOpen. – 2018. https://doi.org/10.5772/intechopen.79083

12. Baktygerey S. B., Mussabek G., Zhylkybayeva N., et al. Palladium catalysts supported on car-bonized porous silicon for H_2/O_2 recombination // Physical Sciences and Technology. – 2023. – Vol. 10, No. 3–4. – Pp. 40–47. https://doi.org/10.26577/phst.2023.v10.i2.05

13. Shaimardan E., Kabdrakhmanova S. K., Beisebekov M. M., et al. Influence of liquid-phase oxida-tion of activated carbon "BAU-A" grade with hydrogenic acid on its surface structure // Bulletin of the National Nuclear Center of the Republic of Kazakhstan. – 2023. – Vol. 3(95). – Pp. 96–101. https://doi.org/10.52676/1729-7885-2023-3-96-102

14. Kabdrakhmanova S., Shaimardan E., Akatan K., et al. Preparation and characterization of the catalyst based on the copper nanoparticles // International Journal of Nanoscience and Nanotechnology. – 2022. – Vol. 18, No. 1. – P. 1–10. https://www.ijnnonline.net/article_249799_fd00a59e31d5e0e9690dfff364998c2b.pdf

15. Mussabek G., Diyuk V.E., Zaderko A.N., Afonin S., Baktygerey S., Taurbayev Ye., Yermukhamed D., Zhylkybayeva N., Yessengereyeva N., Lisnyak V.V. Thermal fluorination of nanoporous activated carbon mediated by freons // Diamond and Related Materials. -2025. -Vol. 155. -Art. 112197. https://doi.org/10.1016/j.diamond.2025.112197

16. Zhumadilov R., Zhumadilov B., Nemkayeva R., et al. In-situ Raman analysis of carbon nanowalls during electrochemical measurement // Physical Sciences and Technology. – 2025. – Vol. 12, No. 1–2. – Pp. 57–67. https://doi.org/10.26577/phst20251216

17. Jujjuri E., Ding E., Shore S. G., Keane M. A. Synthesis and characterization of novel silica-supported Pd/Yb bimetallic catalysts: Application in gas-phase hydrodechlorination and hydrogenation // Journal of Catalysis. – 2006. – Vol. 239. – Pp. 486–500. https://doi.org/10.1016/j.jcat.2006.02.022

18. Mussabek G., Baktygerey S., Taurbayev Ye., Yermukhamed D., Zhylkybayeva N., Zaderko A.N., Diyuk V. E. Afonin S., Yar-Mukhamedova G., Mariychuk R.T., Grishchenko L. M., Kanuchova M., Lisnyak V.V. Surface chemistry and catalytic activity in H_2O_2 decomposition of pyrolytically fluoralkynated activated carbons // RSC Advances. – 2024. – Vol.14. -Art. 29052. https://doi.org/10.1039/d4ra04883k

19. Rodriguez J. G., Lafuente A., Cristóbal de los Ríos. Thermal analysis of 1,4-di[n'-(quinolyl)]buta-1,3-diynes, structure, and topo-oligomerization // Journal of Polymer Science Part A: Polymer Chemistry. – 2004. – Vol. 42, No. 23. – P. 6031–6040. https://doi.org/10.1002/pola.20441

20. Lorenc-Grabowska E., Yperman J., Gryglewicz G., Hoste S., Carleer R. Study on hydrodechlorina-tion of polychlorinated biphenyls during reductive pyrolysis in the presence of a catalyst // Fuel. – 2006. – Vol. 85, No. 3. – P. 374–381. https://doi.org/10.1016/j.fuel.2005.07.002

21. Kume A., Monguchi Y., Hattori K., Nagase H., Sajiki H. Pd/C-catalyzed practical degradation of PCBs at room temperature // Applied Catalysis B: Environmental. – 2008. – Vol. 81, No. 3–4. – P. 274–282. https://doi.org/10.1016/j.apcatb.2007.12.019

22. Nurbolat S. T., Gabdullin M., Kalkozova Z., Mirzaeian M., Abdullin K. Capacitive electrodes based on a combination of activated carbon and graphene // Physical Sciences and Technology. – 2022. – Vol. 9, No. 3–4. – P. 18–24. https://doi.org/10.26577/phst.2022.v9.i2.03

23. Xu Y., Zhang W.-X. Subcolloidal Fe/Ag particles for reductive dehalogenation of chlorinated ben-zenes // Industrial & Engineering Chemistry Research. – 2000. – Vol. 39, No. 7. – P. 2238–2244. https://doi.org/10.1021/ie9903588

24. Mekhaev A. V., Pervova M. G., Taran O. P., Simakova I. L., Parmon V. N. Pd/Sibunit as efficient hydrogen transfer catalyst in hydrodechlorination of polychlorobiphenyls // Russian Journal of Organic Chemistry. – 2014. – Vol. 50, No. 6. – P. 900–901. https://doi.org/10.1134/S1070428014060244

25. Mekhaev A. V., Pervova M. G., Taran O. P., et al. Liquid-phase dechlorination of toxic man-made products using nanodispersed palladium catalysts Sibunit // Chemistry for Sustainable Development. – 2011. – Vol. 19. – Pp. 173–180.

26. Beall G. W., Kuanyshbekov T. K., Tulegenova M. A. Graphene produced by carbon diffusion through nickel foil // Physical Sciences and Technology. – 2018. – Vol. 5, No. 3–4. – P. 37–42. https://doi.org/10.26577/phst-2018-2-156

27. Korte N. E., West O. R., Liang B. G., Zutman J. L., Fernando Q. The effect of solvent concentra-tion on the use of palladized-iron for the step-wise dechlorination of polychlorinated biphenyls in soil ex-tracts // Waste Management. – 2002. – Vol. 22, No. 3. – P. 343–349. https://doi.org/10.1016/S0956-053X(01)00050-2

28. Murena F., Schioppa E., Gioia F. Catalytic hydrodechlorination of a PCB dielectric oil // Environ-mental Science & Technology. – 2000. – Vol. 34. – P. 4382–4385. https://doi.org/10.1021/es000015x

29. Guo-Bin L., Tsukinoki T., Kanda T., Mitoma Y., Tashiro M. Organic reaction in water. Part 2. A new method for dechlorination of chlorobiphenyls using a Raney Ni–Al alloy in dilute aqueous alkaline solution // Tetrahedron Letters. – 1998. – Vol. 39. – P. 5991–5994. https://doi.org/10.1016/S0040-4039(98)01230-1

30. Xia C. H., Liu Y., Xu J., et al. Catalytic hydrodechlorination reactivity of monochlorophenols in aqueous solutions over palladium/carbon catalyst // Catalysis Communications. – 2009. – Vol. 10. – P. 456–458. https://doi.org/10.1016/j.catcom.2008.10.021

31. Calvo L., Gilarranz M. A., Casas J. A., Mohedano A. F., Rodriguez J. J. Hydrodechlorination of alachlor in water using Pd, Ni and Cu catalysts supported on activated carbon // Applied Catalysis B: Envi-ronmental. – 2008. – Vol. 78. – P. 259–266. https://doi.org/10.1016/j.apcatb.2007.09.028

32. Messerle V., Ustimenko A. Plasmatron with renewable carbon nanostructured covering of elec-trodes // Physical Sciences and Technology. – 2014. – Vol. 1, No. 1. – P. 43–47. https://doi.org/10.26577/phst-2014-1-13

33. Das D., Samal D. P., Meikap B. Preparation of activated carbon from green coconut shell and its characterization // Journal of Chemical Engineering & Process Technology. – 2015. – Vol. 6. – P. 248. https://doi.org/10.4172/2157-7048.1000248

34. Shimodaira N., Masui A. Raman spectroscopic investigations of activated carbon materials // Journal of Applied Physics. – 2002. – Vol. 92. – P. 902–909. https://doi.org/10.1063/1.1487434

Information about authors:

Mazhyn K. Skakov – Dr. Sci. (Phys. & Math.), Professor, Academician of KazNAEN, Chief Researcher at the Branch of the National Nuclear Center of the Republic of Kazakhstan, Professor of Physics and Technology at NAO VKU named after S. Amanzholov (Kurchatov, Kazakhstan, e-mail: skakov@nnc.kz, skakovmk@mail.ru).

Alseit Amirov – MSc, Researcher at the Satbayev University (Almaty, Kazakhstan, e-mail: alseit.amirov@gmail.com).

Ainur K. Kabdrakhmanova – PhD, Senior Researcher at the Satbayev University (Almaty & Astana, Kazakhstan, e-mail: ainurkabdrahmanova@mail.ru).

Nodira Toshkuvatova – MSc, Researcher at the Samarkand State University named after Sh. Rashidov (Samarkand, Uzbekistan, e-mail: nodira.toshkuvatova@gmail.com).

Aktam T. Khalmanov – PhD, Researcher at the Samarkand State University of Architecture and Construction named after Mirzo Ulugbek (Samarkand, Uzbekistan, e-mail: a-xalmanov@umail.uz).

Arman Zh. Miniyazov – PhD, Director of the Center for Technological Competence in the Field of Hydrogen Energy, Institute of Atomic Energy, NNC RK (Kurchatov, Kazakhstan, e-mail: miniyazov@nnc.kz).

Viktor V. Baklanov – PhD, Associate Professor, First Deputy Director of the Branch Institute of Atomic Energy, NNC RK (Kurchatov, Kazakhstan, e-mail: baklanov@nnc.kz).

Yerbolat T. Koyanbayev – PhD, Researcher at the Branch Institute of Atomic Energy, NNC RK (Kurchatov, Kazakhstan, e-mail: erbol@nnc.kz).

Nuriya M. Mukhamedova – PhD, Head of Laboratory of Advanced Materials, Branch Institute of Atomic Energy, NNC RK (Kurchatov, Kazakhstan, e-mail: bakayeva@nnc.kz).

Gainiya K. Zhanbolatova – PhD, Senior Researcher at the National Nuclear Center of the Republic of Kazakhstan (Kurchatov, Kazakhstan, e-mail: kaiyrdy@nnc.kz).

Kadu Pramod – M.Sc., M.Phil., PhD, Postdoctoral Researcher, School of Nanoscience and Nanotechnology, Mahatma Gandhi University (Kottayam, India, e-mail: pramd.k145@gmail.com, pramodk@mgu.ac.in).

Ahmed Shakeel – PhD, Assistant Professor at the Postgraduate Department of Chemistry, Government Postgraduate College Rajouri, Higher Education Department, Government of Jammu and Kashmir (Jammu & Kashmir, India, e-mail: editorshakeel@gmail.com).

IRSTI 29.19.22 https://doi.org/10.26577/phst20251223

Kubelka-Munk function, Urbach energy and Kramer–Kronig method in porous silicon

F. Alfeel

Department of Medical Physics, University of Al-Farahidi, Baghdad, Iraq
e-mail: faten.hussein@uoalfarahidi.edu.iq
(Received June 7, 2025; received in revised form November 30, 2025; accepted December 7, 2025)

Porous silicon (PS) samples were fabricated using electrochemical etching and characterized by atomic force microscopy, which showed that the surface roughness increases with porosity. The optical properties and the influence of porosity were investigated through specular and diffuse reflectance, transmission, and absorption measurements. Analysis of the diffuse reflectance spectra using the Kubelka–Munk function revealed that the optical band gap widens as porosity increases, indicating modifications in the electronic structure due to pore formation. The Urbach energy, determined from the absorption edge, also increases with porosity as a result of the higher density of unsaturated surface bonds. The dielectric constant, calculated via the Kramers–Kronig method, shows an increase in both its real and imaginary components with higher porosity, confirming the enhanced energy-storage capability of PS. Thermal energy-loss values likewise rise with pore content. Overall, the results demonstrate that increasing porosity significantly alters the optical and dielectric properties of porous silicon, supporting its potential applications in optoelectronic and energy-storage devices.

Keywords: Porous silicon, Kubelka–Munk function, Urbach energy, dielectric constant, Kramers–Kronig method, refractive index.
PACS number(s): 78.20.Ci, 78.40.-q -, 02.30.-f, 81.07.-b -, 78.30.-j.

1. Introduction

Porous silicon (PS) has attracted substantial interest in recent years owing to its remarkable physicochemical and optoelectronic characteristics, including visible luminescence, tunable refractive index, adjustable energy band gap, and low optical absorption in the visible range [1]. Its high internal surface area, variable surface chemistry, and morphology-dependent porosity, along with its strong light–matter interaction [2] and controllable thermal properties [3], further enhance its technological relevance. These attributes, combined with the relative ease of fabricating well-defined layered structures, have enabled the development of a wide range of PS-based optoelectronic devices, such as light-emitting components, wavelength-selective photodetectors, optical sensors, and Bragg reflectors [4]. Carbon-coated PS has also been incorporated into palladium-based catalysts for safe hydrogen storage, demonstrating improved efficiency and humidity tolerance compared to existing commercial alternatives [5]. Moreover, PS has been explored as a means of enhancing solar-cell efficiency [6,7].

Diffuse reflectance spectra have been widely used to estimate the optical band gap by fitting it to multiple absorption mechanisms for different materials, while Kramers–Kroning transformation has enabled the extraction of dielectric constants from the same measurements [8]. The Urbach tail, which characterizes the degree of disorder near the band edge, has been evaluated via the generalized Tauc–Lorentz method [9]. PS can exhibit extremely high optical absorption, with reported values approaching 99.75% absorption at selected frequencies; this absorption can be dynamically tuned by varying external parameters such as pump-beam fluence [10]. Integration of PS with materials like Vanadium dioxide (VO_2) further enhances its tunability, enabling phenomena such as electromagnetically induced transparency (EIT) and narrow-band absorption that are controllable through temperature or optical pumping [11]. Such hybrid

systems are compatible with modern semiconductor processing techniques, expanding their potential for advanced optoelectronic applications [12].

Although several studies have investigated the physical properties of PS and the influence of individual fabrication [13], the literature lacks a systematic, comparative analysis of how different manufacturing conditions simultaneously affect key optical descriptors–namely, the band gap derived from the Kubelka–Munk function, the degree of band-edge disorder assessed through the Urbach energy, and the dielectric response obtained from the Kramers–Kronig method. Similarly, a coherent examination of surface roughness, its dependence on porosity, and its relationship to fabrication parameters across two groups of samples within a single study has not yet been reported.

This work provides a comprehensive analysis that systematically correlates the optical properties of porous silicon with key fabrication parameters, including current density and HF concentration, as well as surface roughness and porosity. By preparing samples under controlled variations of these parameters, the study establishes quantitative relationships and offers deeper insight into how different manufacturing conditions influence the resulting optical behavior. The findings presented here serve as a valuable reference for future researchers and designers developing hybrid optoelectronic systems, providing an essential materials database for advanced device engineering.

2. Theoretical basis for optical and structural parameter calculations

2.1. Porosity and film thickness

The influence of the HF concentration and current density on the porosity was studied by performing anodic etching under various combinations of these parameters and characterizing the resulting PS samples. The porosity *P* of PS is defined as the fraction of void volume within the porous layer and can be easily determined via using standard gravimetric measurements [14]

$$P(\%) = \frac{m_1 - m_2}{m_1 - m_3} \quad (1)$$

where m_1 is mass of the pristine silicon wafer prior anodization, m_2 is the mass immediately after anodization, m_3 is the mass after complete dissolution of the porous layers in a molar NaOH aqueous solution. The selective removal of the PS layer is achieved by immersing the sample for several minutes in a 3% NaOH solution, which dissolves the porous silicon without affecting the underlying crystalline substrate.

The thickness *L* of the porous layer was also determined gravimetrically using:

$$L = \frac{m_1 - m_3}{\rho S} \quad (2)$$

where ρ is the density of bulk silicon and S is the etched surface area [14].

Additionally, the film thickness *L* was calculated from the reflectance spectrum using Eq. (3), based on the separation between two adjacent interference peaks with refractive indices of n_1 and n_2 and corresponding wavelengths of λ_1 and λ_2 [13]:

$$L = \frac{\lambda_1 \lambda_2}{2(\lambda_1 n_2 - \lambda_2 n_1)} \quad (3)$$

2.2. Diffuse reflectance spectroscopy (DR) and the Kubelka-Munk function

Diffuse refraction spectra (DRS) were converted into equivalent absorption spectra using the Kubelka–Munk formalism, which is widely employed for determining the optical band gap of porous and powdered materials [15-18].

$$F(R) = \frac{K}{S} = \frac{(1-R)^2}{2R} \quad (4)$$

where *F(R)* is the Kubelka–Munk function, *R* is the diffuse reflectance of the film as a function of the wavelength, S and K denote the scattering and absorption Kubelka–Munk coefficients, respectively.

The energy band gap was then extracted by plotting $(F(R) * hf)^n$ as a function of photon energy (hf), where the exponent n takes the value of 2 for direct allowed transitions and 1/2 for indirect allowed transitions [16]. The linear portion of the resulting Tauc plot was extrapolated to the energy axis to obtain the corresponding band gap.

2.3. Urbach energy tail E_u

The Urbach energy is an important parameter that characterizes the density of localized defect states within the band-gap region. These defect states–arising from structural disorder, lattice imperfections, and incomplete surface passivation–give rise to an exponential absorption tail in the sub-band-gap

region of the optical spectrum, known as the Urbach tail. This tail reflects absorption contributions from both the crystalline lattice and dopant-related states. The magnitude of this tail, quantified as the Urbach energy, provides insight into the degree of disorder present in the material. The Urbach energy can be extracted from absorption spectra using the empirical relation [9,17,19]:

$$\alpha = \alpha_o Exp(\frac{E}{E_u}) \quad (5)$$

where E_u is the Urbach energy, α is the absorption coefficient and α_o is a material-dependent constant. The incident photon energy is given by $E = hf$, where h is a Plank's constant and f is photon frequency.

The absorption coefficient can also be calculated from equation [17]:

$$\alpha = \frac{A}{L} \quad (6)$$

where L is the thickness of the film and A is the absorption.

According to the Beer–Lambert's law [20]:

$$A = -Ln(T) \quad (7)$$

Therefore, equation (6) can be written as [15]:

$$\alpha = -\frac{\ln(T)}{L} \quad (8)$$

The refractive index n and extinction coefficient k can be calculated as follows [19-21]:

$$n = \frac{1-R_{spec}}{1+R_{spec}-2\sqrt{R_{spec}}\,cos\theta} \quad (9)$$

$$k = \frac{2\sqrt{R_{spec}}\,sin\theta}{1+R_{spec}-2\sqrt{R_{spec}}\,cos\theta} \quad (10)$$

where R_{spec} represents the specular reflectance of the PS.

The dielectric constant describes the ability of a material to store electrical energy when subjected to an external electric field. It is expressed as a complex quantity comprising two components: a real part and an imaginary part. The real component represents the amount of energy stored elastically within the material; thus, higher values of the real dielectric constant indicate greater energy-storage capability. In contrast, the imaginary component corresponds to dielectric losses, reflecting the amount of energy dissipated as heat. Consequently, an increase in the imaginary dielectric constant signifies greater thermal energy loss under an applied electric field [21,22].

The complex dielectric function can be calculated using the following relations [20]:

$$\tilde{\varepsilon} = \varepsilon_r + i\varepsilon_i$$

$$\varepsilon_r = n^2 - k^2 \quad (11)$$

$$\varepsilon_i = 2nk \quad (12)$$

where $\tilde{\varepsilon}$ is a complex dielectric constant, ε_r and ε_i are its real and imaginary components, and n and k are the refractive index and extinction coefficient, respectively.

3. Materials and methods

Two groups of n-type crystalline silicon (c-Si) wafers with a (100) orientation were electrochemically etched in hydrofluoric acid (HF) solutions of varying concentrations. In the first group samples were etched in 20% HF (by volume) at different current densities of 30, 40, and 50 mA/cm² for 5 minutes. The second group was fabricated using HF solutions of 25%, 30%, and 35% (by volume) at a fixed current density of 20 mA/cm² for 10 minutes. After anodization, all the samples of PS were gently removed, rinsed in deionized water, and dried. The presence of PS was initially confirmed through its characteristic photoluminescence under UV illumination [1–3, 23]. The full set of fabrication parameters is summarized in Table 1.

Atomic force microscopy (AFM) was employed to accurately assess both porosity and surface roughness. Optical scattering measurements were conducted using an integrating sphere attached to a spectrophotometer operating over the 350–2500 nm wavelength range.

A central objective of this study is to examine how the porosity of silicon influences its optical properties–most notably the energy band gap and dielectric constant–and to establish quantitative relationships between structural parameters and optical responses.

Table 1 – Fabrication parameters of the PS samples.

PS n-type Samples	HF concentration (%)	Anodization time(min)	Current density (mA/cm^2)	Porosity%
S1	20	5	30	30.8 ± 0.05
S2	20	5	40	32.28 ± 0.05
S3	20	5	50	33 ± 0.05
S4	25	10	20	17 ± 0.05
S5	30	10	20	14 ± 0.05
S6	35	10	20	9 ± 0.05

4. Results and discussion

The porosity (p%) increases with increasing current density, as shown in Fig.1a. At low current densities, the number of charge carriers is limited, resulting in minimal silicon dissolution along the current path and, consequently, low porosity. At higher current densities, the increased availability of charge carriers enhances dissolution, leading to higher porosity [24].

Similarly, the porosity (p%) increases as the HF concentration decreases, as shown in Fig.1b. Lower HF concentrations promote greater silicon dissolution, effectively increasing the critical current density at the oxide–silicon interface. As the HF concentration increases, the pore structure becomes finer and the pore walls thicken, resulting in a reduction in overall porosity [25].

Atomic force microscopy (AFM) was employed to examine the surface morphology of the PS samples and to quantify their surface roughness. Fig. 2 presents 2D AFM images of the investigated samples. These measurements were used to establish the relationship between surface roughness and the fabrication conditions applied during sample preparation.

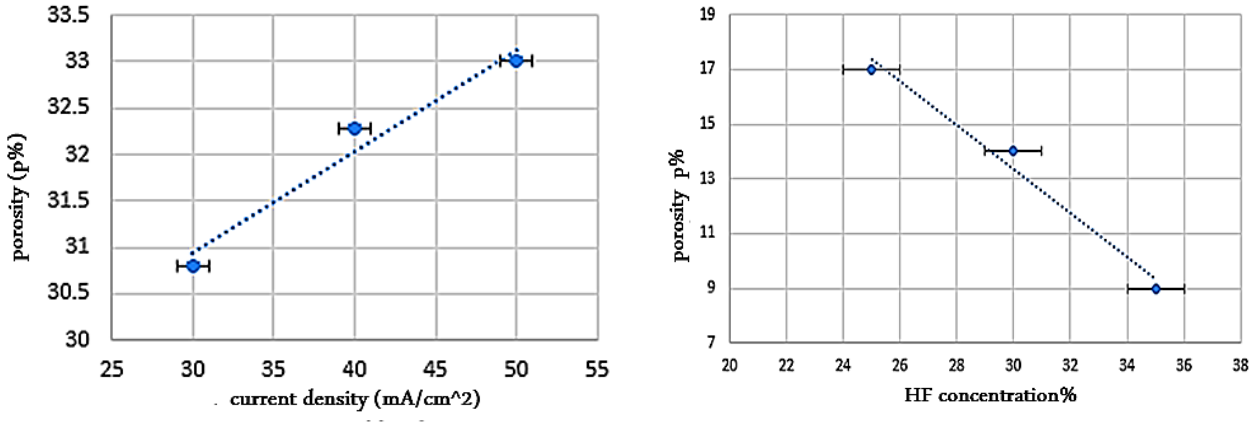

a) b)

Figure 1 – (a) Porosity (p%) of the PS layers as a function of current density for samples etched at 20% HF.
(b) Porosity (p%) of the PS layers as a function of HF concentration for samples etched at a fixed time and current density.

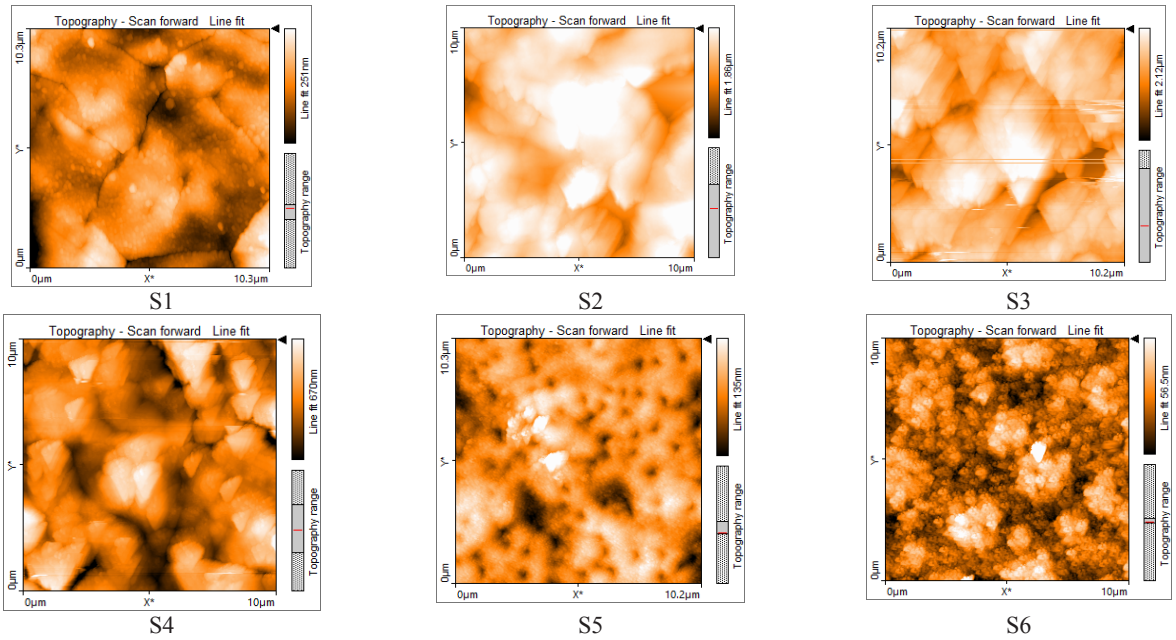

Figure 2 – 2D AFM images (10 × 10 μm^2) of PS.

The introduction of pores into crystalline silicon inherently increases surface roughness, as greater porosity corresponds to a larger number of pores that disrupt the initially smooth surface. As shown in Fig.3, the surface roughness increases systematically with increasing porosity, consistent with the accompanying increase in effective surface area.

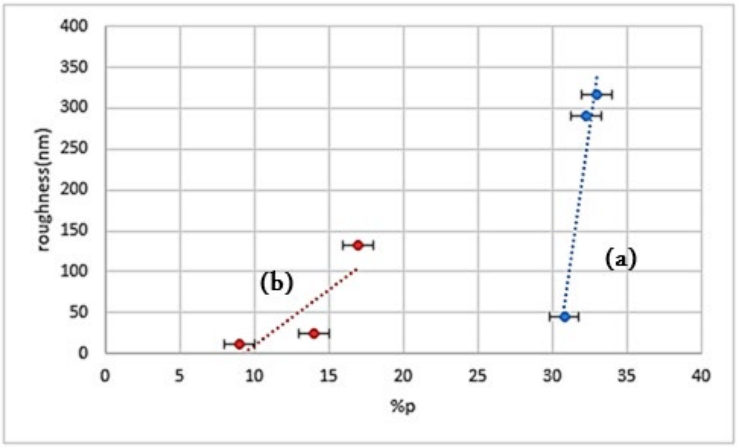

Figure 3 – Surface roughness vs porosity of PS samples:
(a) PS samples prepared at different current densities;
(b) PS samples prepared at different HF concentrations.

The optical properties of the PS samples were studied using a UV–Vis–NIR spectrophotometer to record diffuse reflectance (DR) spectra (Fig. 4). Due to the roughened surface of PS, incident light is primarily scattered rather than specularly reflected. The nanoscale features within the porous layer give rise to distinct light–matter interactions, including interference effects in both the ultraviolet and visible regions of the spectrum, whereas the infrared region remains relatively flat. When light interacts with pores whose dimensions are comparable to the incident wavelength, resonant scattering occurs, producing

constructive or destructive interference with the scattered waves. This process strongly influences the transmittance, absorption, and reflectance properties of the material. Small pores preferentially scatter shorter wavelengths, while larger pores are more effective at scattering longer wavelengths. Furthermore, the presence of pores facilitates partial confinement of light within the silicon matrix, thereby modifying the effective optical path and altering the measured reflectance and absorption values [26].

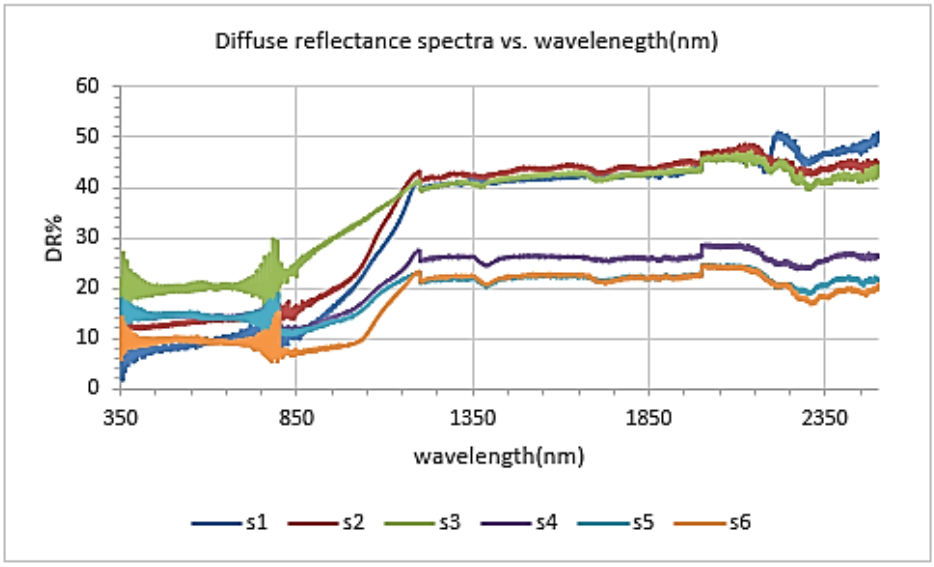

Figure 4 – DR spectra (expressed in %) of the PS samples recorded across the 350–2500 nm wavelength range.

Fig. 5 shows the spectra of the transmittance (T) as a function of the wavelength. The transmittance increases as the porosity increases because more pores make silicon more transparent.

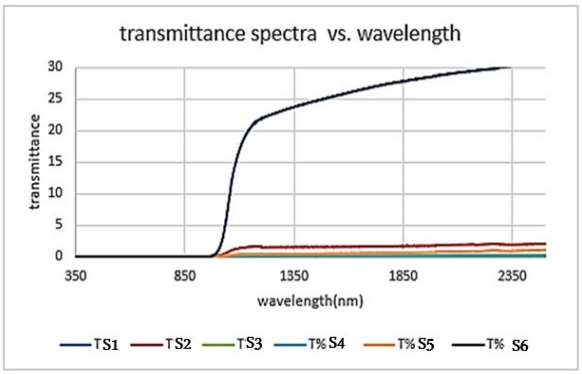

Figure 5 – Transmittance spectra of the PS samples measured over the wavelength range of 350–2500 nm.

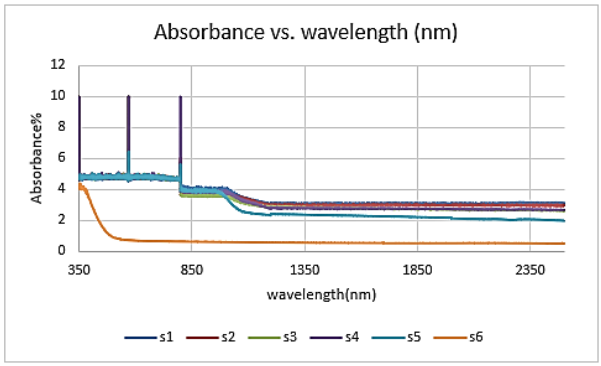

Figure 6 – Absorbance spectra of the PS samples recorded across the 350–2500 nm wavelength range.

The transmittance (T) spectra of the PS samples were used to calculate the absorption coefficient using Eq. (8). As shown in Fig. 6, the absorbance increases with increasing porosity. This behavior arises because pores partially trap incoming light: a portion of the light is transmitted through the porous

network, while the remainder is absorbed by the silicon walls surrounding the pores.

Using Eq. (9), the refractive index of the PS samples at a fixed wavelength of 808 nm was determined. As illustrated in Fig. 7, the refractive index increases with increasing porosity. This trend occurs because light propagates more rapidly through air-filled pores than through dense silicon; thus, a higher pore fraction results in an overall effective refractive index governed by an effective medium approximation. The refractive index of porous silicon therefore differs substantially from that of bulk crystalline silicon [1].

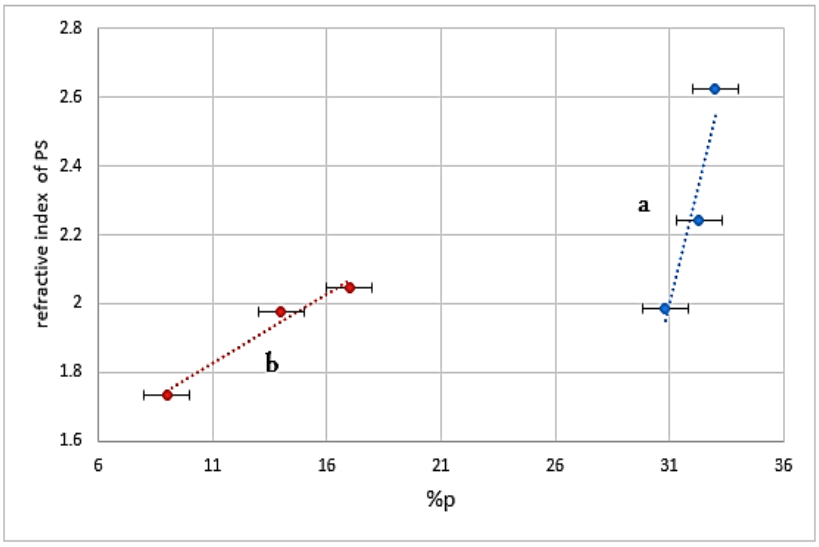

Figure 7 – Refractive index of PS samples at 808 nm as a function of porosity.
(a) PS samples prepared at different current densities;
(b) PS samples prepared at different HF concentration.

The energy band gap E_g was calculated using the Kubelka–Munk function, by plotting $(F(R) * hf)^n$ versus (hf) for n =2, corresponding to a direct allowed transition (Figure 8). The energy gap value was extracted from the intercept of the linear portion of the plot with the energy axis. The E_g values for PS samples are larger than that of bulk silicon, consistent with the presence of nanoscale silicon structures. As porosity increases, the remaining silicon frameworks become thinner and approach characteristic dimensions where quantum confinement becomes significant, leading to a widening of the energy band gap [26].

Fig. 9 shows the dependence of the optical band gap on porosity. For samples prepared at different current densities, the band gap increases from 1.87 eV to 3.26 eV as the porosity increases from 30.8% to 33%. Similarly, for samples fabricated at different HF concentrations, the band gap increases from 1.76 eV to 3.30 eV as porosity rises from 9% to 17%. When pores form within silicon at dimensions comparable to the de Broglie wavelength of charge carriers (electrons and holes), quantum confinement effects emerge. This confinement restricts carrier motion, discretizes the energy levels, and prevents the formation of a continuous energy band structure, thereby widening the band gap. The formation of localized energy states near the porous silicon surface also modifies the electronic properties and influences the carrier concentration [24].

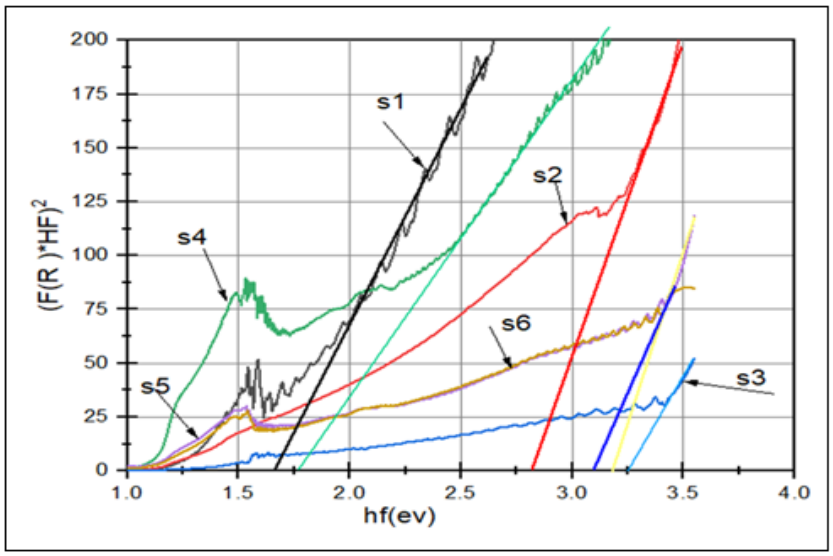

Figure 8 – Plots of $(F(R) * hf)^n$ versus (hf), used to determine the optical band gap of PS samples based on the Kubelka–Munk function.

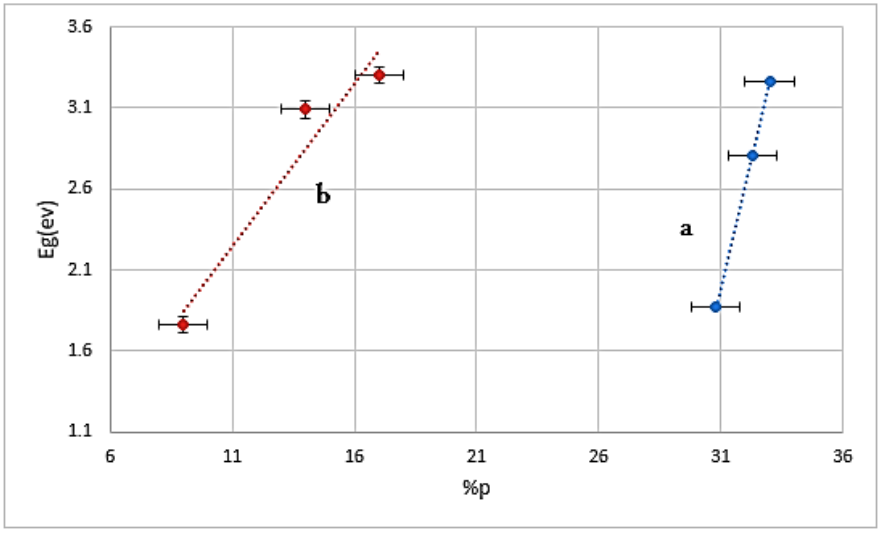

Figure 9 – Optical band gap as a function of porosity (p%) for the PS samples.
(a) Samples prepared at different current densities. (b) Samples prepared at different HF concentrations.

The absorption coefficient was calculated from the transmittance spectrum using Eq. (8), and the Urbach energy (Eu) was then determined using Eq. (5) by plotting $\ln(\alpha)$ versus hf. The inverse of the slope of linear region of this plot (illustrated for sample S1 in Fig. 10) yields the Urbach energy for each sample.

As shown in Fig. 11, the Urbach energy increases from 0.311 eV to 0.93 eV as porosity rises from 30.8% to 33% for samples prepared at different current densities. For samples prepared at varying HF concentrations, Eu increases from 0.1136 eV to 0.6696 eV as porosity increases from 9% to 17%. All values were obtained using identical procedures.

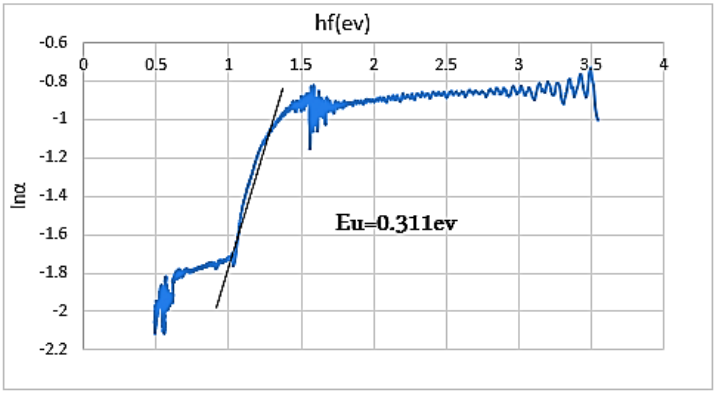

Figure 10 – Plot of ln(α) versus hf for determining the Urbach energy of sample S1.

The Urbach energy, often referred to as correlation energy, represents the energy required to break chemical bonds at the material surface and is closely associated with structural disorder and the presence of dangling or incomplete bonds [27]. As porosity increases, the number of such defect states grows, resulting in a corresponding increase in the Urbach energy.

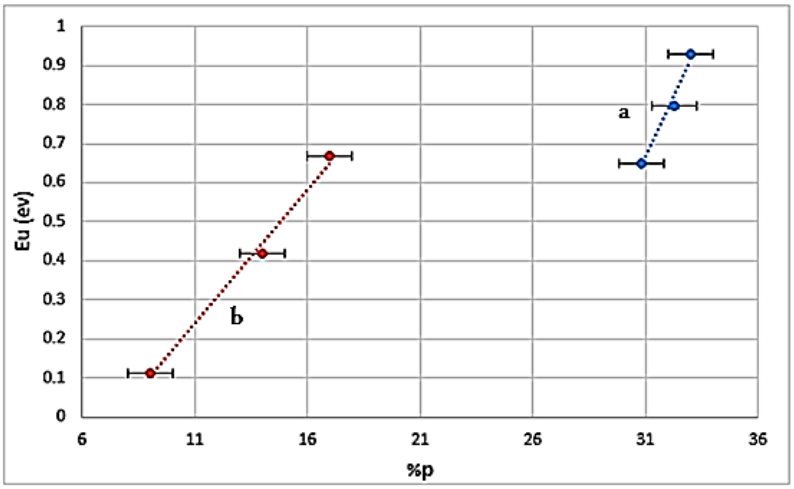

Figure 11 – Urbach energy as a function of porosity (P%P%) for the PS samples.
(a) Samples prepared at different current densities.
(b) Samples prepared at different HF concentrations.

The real part of the dielectric constant was calculated using Eq. (11), while the imaginary part was obtained using Eq. (12). At a wavelength of 808 nm, both components of the dielectric constant for the PS samples are shown in Figures 12 and 13. The results demonstrate that both the real and imaginary parts of the dielectric constant increase with increasing porosity. The incorporation of pores enhances the overall polarity of the material, thereby increasing the real dielectric constant. At the same time, the presence of pores promotes stronger scattering and confinement of electromagnetic waves, which leads to higher dielectric losses and thus a larger imaginary component. As shown previously in Fig. 11, higher porosity also corresponds to increased Urbach energy, indicating a greater density of defect states. These surface states may serve as active sites for interactions with

particles such as protons or secondary ions, making porous silicon a promising candidate for catalytic and biosensing applications [28].

The increase in the real part of the dielectric constant with porosity is particularly relevant for applications requiring materials with tunable dielectric behavior. High-dielectric porous layers can function as active components in ferroelectric capacitors, ferroelectric field-effect transistors (FeFETs), and ferroelectric tunneling junctions (FTJs), or as low-index interlayers in optical and electronic device architectures [29]. Conversely, a higher imaginary dielectric constant reflects increased energy dissipation, which is undesirable in photonic circuits where losses must be minimized, but advantageous in photothermal processing, where efficient heat generation is required.

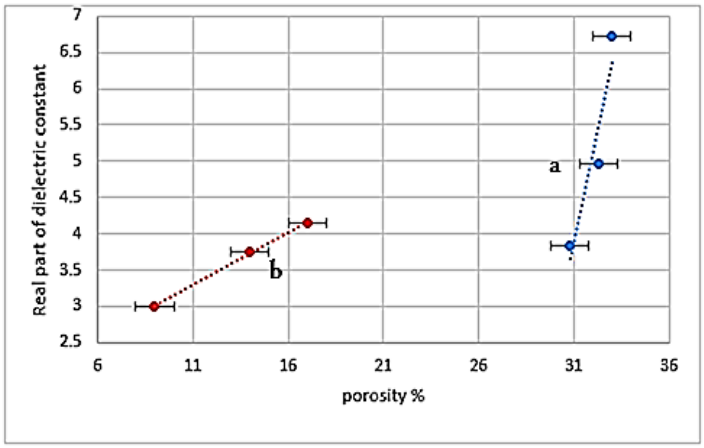

Figure 12 – Real part of the dielectric constant (ε_r) of the PS samples at 808 nm as a function of porosity. (a) Samples prepared at different current densities. (b) Samples prepared at different HF concentrations.

Porosity also directly influences the specific surface area of PS; as the surface area increases, the material exhibits enhanced responsiveness under an applied electric field [26]. Furthermore, the emergence of additional defect levels modifies the polarization behavior of the material [30]. Previous results have shown that changes in the energy band gap due to porosity alter the electronic structure and optical transitions within the material [31], which in turn impacts the dielectric response. As silicon transitions from a bulk semiconductor to a porous structure with a wider band gap, its absorption and transmission characteristics change accordingly, leading to corresponding variations in the dielectric constant [32].

Table 2 summarizes the results obtained in this study. Samples S1, S2, and S3 were fabricated by varying the current density while keeping the HF concentration and etching time constant. Their porosity increased from 30.8% to 33% with increasing current density. Correspondingly, the optical band gap expanded from 1.87 eV to 3.26 eV, while the Urbach energy increased from 0.649 eV to 0.930 eV. Surface roughness showed a pronounced rise, from 44.3 nm to 316.0 nm. The real part of the dielectric constant increased from 3.838 to 6.733, and the imaginary part increased from 0.745 to 2.47.

Samples S4, S5, and S6–prepared by varying the HF concentration while maintaining constant current density and etching time–showed the expected trend that higher HF concentrations yield lower porosity. When the samples are ranked by increasing porosity, they similarly show an increase in band gap from 1.76 eV to 3.30 eV and a rise in Urbach energy from 0.114 eV to 0.669 eV. Surface roughness increased from 11.1 nm to 131.6 nm. The real part of the dielectric constant increased from 2.99 to 4.148, while the imaginary part increased from 0.427 to 0.836.

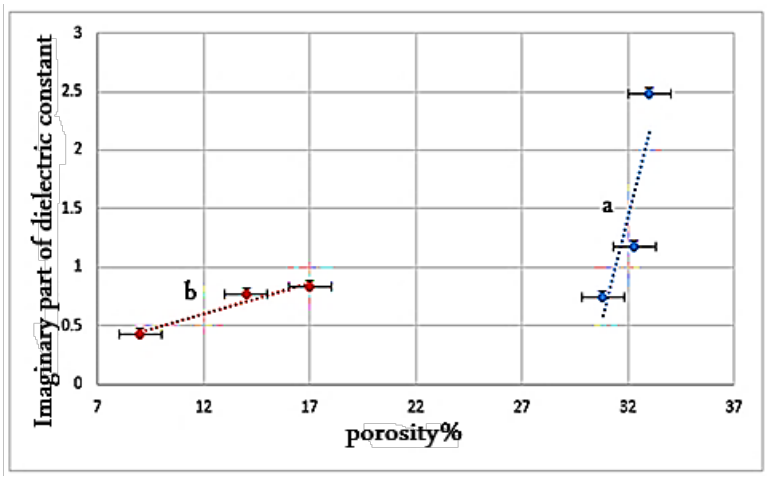

Figure 13 – Imaginary part of the dielectric constant (ε_i) of the PS samples at 808 nm as a function of porosity. (a) Samples prepared at different current densities. (b) Samples prepared at different HF concentrations.

Table 2 – Summary of optical and structural properties of PS samples.

Sample	S1	S2	S3	S4	S5	S6
Porosity% ∓0.05	30.8	32.28	33	17	14	9
Refractive index nps ∓0.001	1.97	2.24	2.63	2.05	1.98	1.74
E_g (ev) ∓0.0002	1.87	2.81	3.26	3.3	3.09	1.76
Roughness (nm) (∓0.005)	44.30	290.06	316.03	131.57	24.51	11.14
E_u (ev) (0.001)	0.649	0.795	0.930	0.669	0.417	0.114
$\varepsilon_i \mp 0.001$	0.745	1.178	2.477	0.836	0.765	0.427
$\varepsilon_r \mp 0.001$	3.838	4.959	6.733	4.148	3.757	2.991
Film thickness(nm)∓5nm	13620	14274	14592	948.63	781.22	502.22

5. Conclusion

This study demonstrates clear correlations between fabrication parameters and the fundamental optical and dielectric properties of porous silicon. By varying current density and HF concentration across two groups of samples, we observed systematic increases in porosity, which in turn led to higher optical band gaps, larger Urbach energies, increased surface roughness, and enhanced real and imaginary components of the dielectric constant. These trends reflect the growing density of defect states and the stronger light–matter interactions introduced by the porous structure.

The results highlight the strong dependence of PS properties on its fabrication conditions and underscore the importance of porosity as a key tuning parameter. These findings provide useful guidelines for the design of porous silicon components in optoelectronic devices, sensors, and hybrid materials. Moreover, the work opens pathways for further functionalization, including filling pores with tailored materials to achieve application-specific performance. Overall, this study links fundamental materials characterization with practical engineering considerations for future PS-based technologies.

Acknowledgments: I'm very grateful to Head of the Physics Department at the Faculty of Science at Damascus University, prof. Iyad Madwar, for helping me preparing samples, conduct measurements, and allow me to use the university's scientific research laboratories.

References

1. Alfeel F., Awad F., Qamar F. Tunable optical properties of porous silicon of p-type porous silicon // Damascus University Journal for the Basic Sciences. – 2014. – Vol. 30, No. 2. – Pp. 41–51.

2. Alfeel F., Awad F., Qamar F. Change of diffused and scattered light with surface roughness of p-type porous silicon // International Journal of Nano Dimensions. – 2014. – Vol. 5, No. 4. – Pp. 415–419. https://doi.org/10.7508/ijnd.2014.04.014

3. Alfeel F., Awad F., Qamar F. Changes of thermal conductivity, optical conductivity and electric conductivity of porous silicon with porosity // Journal of New Technology in Materials. – 2013. – Vol. 3, No. 1. – Pp. 56–60. https://doi.org/10.12816/0010281

4. Torres-Costa V., Martín-Palma R.J. Application of nanostructured porous silicon in the field of optics: A review // Journal of Materials Science. – 2010. – Vol. 45, No. 11. – Pp. 2823–2838. https://doi.org/10.1007/s10853-010-4251-8

5. Baktygerey S.Z. et al. Palladium catalysts supported on carbonized porous silicon for H_2/O_2 recombination // Physical Sciences and Technology. – 2023. – Vol. 10, No. 2. – Pp.40-47. https://doi.org/10.26577/phst.2023.v10.i2.05

6. Salman K.A., Hassan Z., Omar K. Effect of silicon porosity on solar cell efficiency // International Journal of Electrochemical Science. – 2012. – Vol. 7, No. 1. – Pp. 376–386.

7. Mussabek G., Mirgorodskij I., Kharin A., Taurbayev T., Timoshenko V. Formation and optical properties of nanocomposite based on silicon nanocrystals in polymer matrix for solar cell coating // J. Nanoelectron Optoelectron. -2015, -Vol. 9, --No. 6, -Pp. 738-740. https://doi.org/10.1166/jno.2014.1670

8. Nowak M., Kauch B., Szperlich P. Determination of energy band gap of nanocrystalline SbSI using diffuse reflectance spectroscopy // Review of Scientific Instruments. – 2009. – Vol. 80, No. 4. – Art. 046107. https://doi.org/10.1063/1.3103603

9. Riungu G.G., Mugo S.W., Ngaruiya J.M., John G.M., Mugambi N. Optical band energy, Urbach energy and associated band tails of nanocrystalline TiO_2 films at different annealing rates // American Journal of Nanosciences. – 2021. – Vol. 7, No. 1. – Art. 28. https://doi.org/10.11648/j.ajn.20210701.15

10. Wang Y., Yue L., Cui Z., Zhang X., Zhu Y., Zhang K. Optically tunable single narrow band all-dielectric terahertz metamaterials absorber // AIP Advances. – 2020. – Vol. 10, No. 4. – Art. 045039. https://doi.org/10.1063/5.0003817

11. Zhang X., Wang G., Liu J., Zuo S., Li M., Yang S., Jia Y., Gao Y. Switchable and tunable terahertz metamaterial based on vanadium dioxide and photosensitive silicon // Nanomaterials. – 2023. – Vol. 13. – Art. 2144. https://doi.org/10.20944/preprints202306.1936.v1

12. Hao D., Zhang Y., et al. Silicon bowtie structure based adjustable nonrigid all-nonmetal metamaterial terahertz filter // Optics Letters. – 2022. – Vol. 47, No. 23. – Pp. 6101–6104. https://doi.org/10.1364/ol.471704

13. Manakov S.M., Sagidolda Ye. Investigation of the physical properties of nanoscale porous silicon films // Physical Sciences and Technology. – 2015. – Vol. 2, No. 1. – Pp. 4–8. https://doi.org/10.26577/2409-6121-2015-2-1-4-8

14. Alfeel F.M. Optical properties of ZnO film on porous silicon p-type substrate // Damascus University Journal for the Basic Sciences. – 2025. – Vol. 41, No. 1. – Pp. 101–115.

15. Chryssou K., Stassinopoulou M., Lampi E. A study of the optical bandgap energy and Urbach energy tail of two white A4 copy paper samples // Annals of Chemical Science Research. – 2021. – Vol. 3, No. 1. Art. 000551. https://doi.org/10.31031/ACSR.2021.03.000551

16. Venkatesan R., Mayandi J., Pearce J.M., Venkatachalapathy V. Influence of metal assisted chemical etching time period on mesoporous structure in upgraded metallurgical grade silicon for solar cell application // Journal of Materials Science: Materials in Electronics. – 2019. – Vol. 30, No. 9. – Pp. 8676–8685. https://doi.org/10.1007/s10854-019-01191-6

17. Mussabek G.K., Yermukhamed D., Suleimenova Z. A., Assilbayeva R. B., Sivakov, V. A., Zavestovskaya. I. N., V.Yu. Timoshenko. Reflectance modification in nanostructured silicon layers with gradient porosity // Bulletin of the Lebedev Physics Institute. – 2019, -Vol. 46, – No.10, -Pp. 314-318. https://doi.org/10.3103/S106833561910004X

18. Dejam, Sabbaghzadeh J., Ghaderi A., Solaymani S., Matos R.S., Ţălu Ş., Henrique D., Sari A.H., Kiani M., Amir A., Doudaran M.A. Advanced nano-texture, optical bandgap, and Urbach energy analysis of NiO/Si heterojunctions // Scientific Reports. – 2023. – Vol. 13, No. 1. – Art. 3766. https://doi.org/10.1038/s41598-023-33713-y

19. Norouzzadeh P., Mabhouti Kh., Golzan M.M., Naderali R. Investigation of structural, morphological and optical characteristics of Mn-substituted Al-doped ZnO nanoparticles: A Urbach energy and Kramers–Kronig study // Optik. – 2020. – Vol. 204. – Art. 164227. https://doi.org/10.1016/j.ijleo.2020.164227

20. BYJU'S. Derivation of Beer–Lambert law [Electronic resource]. – 2018. – Available at: https://byjus.com/physics/derivation-of-beer-lambert-law (available on December 15, 2025).

21. Nazari N., Golzan M.M., Mabhouti Kh. Study of Urbach energy and Kramers–Kronig on Mn- and Zn-doped $NiFe_2O_4$ ferrite nanopowder for the determination of structural and optical characteristics // Scientific Reports. – 2024. – Vol. 14, No. 1. – Art. 6407. https://doi.org/10.1038/s41598-024-57045-7

22. Singh K.P., Bhattacharjee S. Optical parameters of atomically heterogeneous systems created by plasma-based low energy ion beams // Frontiers in Physics. – 2021. – Vol. 9. Art. 671137. https://doi.org/10.3389/fphy.2021.671137

23. Zhanabaev Z., Ibraimov M., Sagidolda Y. Nonlinear electrical properties of nanostructured porous silicon films // Physical Sciences and Technology. – 2014. – Vol. 1, No. 1. – Pp. 69–73. https://doi.org/10.26577/phst-2014-1-17

24. Solanki C.S., Bilyalov R., Poortmans J., et al. Self-standing porous silicon films by one-step anodizing // Journal of the Electrochemical Society. – 2004. – Vol. 151, No. 5. – Pp. C307–C313. https://doi.org/10.1149/1.1688797

25. Burham N., Hamzah A.A., Majlis B.Y. Effect of hydrofluoric acid concentration on pore size diameter of silicon membrane // Bio-Medical Materials and Engineering. – 2014. – Vol. 24, No. 6. – Pp. 2203–2209. https://doi.org/10.3233/BME-141032

26. Sze S.M., Ng K.K. Physics of semiconductor devices. – Hoboken: Wiley, 2006, 815 p. https://doi.org/10.1002/0470068329

27. Sivaprakash P., Venkatesan R., Muthu S.E., Hatshan M.R., Vetcher A.A., Kim S.-C., Kim I. Effect of different etching times on the structural, morphological, electrical, and antimicrobial properties of mesoporous silicon // Heliyon. – 2023. – Vol. 9, No. 12. – Art. e23105. https://doi.org/10.1016/j.heliyon.2023.e23105

28. Muhammad W., Song J., Kim S., Ahmed F., Cho E., Lee H., et al. Silicon-based biosensors: A critical review of silicon's role in enhancing biosensing performance // Biosensors. – 2025. – Vol. 15. – Art. 119. https://doi.org/10.3390/bios15020119

29. Yang J.J., Grollier J., Williams R.S., Huang R. Neuromorphic engineering: From materials to device application // Advanced Materials. – 2023. – Vol. 35, No. 37. -Art. 2305078. ahttps://doi.org/10.1002/adma.202305078

30. Yakovtseva V., Volchek S., Bondarenko V., Sayyed M.I., Hanafy T.A., Trukhanov S., Bondaruk A., et al. Effects during the cathode polarization of porous silicon // Heliyon. – 2024. – Vol. 10, No. 15. – Art. e34675. https://doi.org/10.1016/j.heliyon.2024.e34675

31. Anwar S., Muhammad, Ha S.J.-H., Lee J., Song I.-H., Kim Y.-W. Controlling the electrical resistivity of porous silicon carbide ceramics and their applications: A review // International Journal of Applied Ceramic Technology. – 2022. – Vol. 19, No. 4. – Pp. 1814–1840. https://doi.org/10.1111/ijac.14034

32. Friedrich S., Stojecevic S., Rapp P., Helmer S., Bock M., Durdel A., Gasteiger H.A., Jossen A. Effect of mechanical pressure on lifetime, expansion, and porosity of silicon-dominant anodes in laboratory lithium-ion cells // Journal of the Electrochemical Society. – 2024. – Vol. 171, No. 5. – Art. 050540. https://doi.org/10.1149/1945-7111/ad36e6

Information about author:

Faten Alfeel – Assistant Professor at the Medical Physics Department, College of Science, Al-Farahidi University (Baghdad, Iraq, e-mail: faten.hussein@uoalfarahidi.edu.iq).

IRSTI 53.37.23 https://doi.org/10.26577/phst20251224

Synthesis and properties of polyfunctional coatings on aluminum and titanium alloys

G.Sh. Yar-Mukhamedova[1*], N. Sakhnenko[2], A. Korogodskaya[2], I. Stepanova[2], A. Karakurkchi[3], W.Y. Wang[4], D. Zellele[1] and A. Imanbayeva[1]

[1]Al-Farabi Kazakh National University, Almaty, Kazakhstan
[2]National Technical University "Kharkiv Polytechnic Institute", Kharkiv, Ukraine
[3]National Defense University of Ukraine named after I. Chernyakhovsky, Kyiv, Ukraine
[4]Northwestern Polytechnical University, Xi'an, Shaan Xi, China
*e-mail: gulmira-alma-ata@mail.ru

(Received October 22, 2025; received in revised form November 30, 2025; accepted December 9, 2025)

This work presents the synthesis of highly active electrode materials for the electrolytic production of hydrogen from aqueous solutions, which can also serve as photocatalysts. Composite coatings produced by plasma–electrolytic oxidation on aluminum and titanium alloy substrates, doped with vanadium and tungsten compounds, were investigated. The electrolysis processes of aqueous solutions using these composites as electrode materials were analyzed. Linear voltammetry was applied to determine the Tafel equation constants for the systems $WO_3 – V_2O_5 – Al_2O_3$ / Al and $WO_3 – V_2O_5 – TiO_2$ / Ti, which are proposed as electrode materials for hydrogen evolution reactions. The study found that the dopant content, the metallic substrate characteristics, and surface morphology strongly influence the coatings' functional properties. The Tafel coefficients *a* and *b* indicate a high level of electrocatalytic activity for the synthesized coatings, confirming their suitability as electrode materials for electrolytic hydrogen production. A comparison of photocatalytic activity in the methyl orange degradation reaction revealed higher activity of the aluminum-based coating than the titanium-based coating, highlighting the relevance of these materials for ecological technologies. The presence of nonstoichiometric oxides, compositional variability, morphological differences, and the developed surface area accounts for their exceptionally high electrocatalytic activity and, therefore, their strong potential for functional applications.

Keywords: plasma electrolytic oxidation, composite coatings, metallic substrates, vanadium and tungsten oxides, photocatalysis, electrocatalysis, hydrogen evolution reaction, degradation.
PACS number(s): 68.37.-d, 81.65.-b, 81.05.Bx.

1. Introduction

Plasma electrolytic oxidation (PEO) is a well-established surface treatment technique for the formation of oxide coatings on valve metals such as Al, Ti, Zr, Ta, and Nb. This method enables the synthesis of multicomponent surface layers incorporating transition metal oxides, thereby offering broad possibilities for tailoring functional properties [1]. A key characteristic of the PEO process is the continuous and dynamic restructuring of the coating across the entire metal surface. Under PEO anodizing conditions, dielectric breakdown events give rise to numerous transient microdischarges that are repeatedly generated over the surface of the substrate. These localized discharge channels are associated with extreme temperature gradients, reaching approximately 2000–10 000 K, which facilitate the transformation of initially amorphous oxide phases into crystalline structures. As a result, PEO-derived coatings exhibit highly tunable morphologies, strong interfacial adhesion, elevated microhardness, and excellent resistance to wear and corrosion. In recent years, significant research attention has focused on the photocatalytic performance of modified coatings based on titanium (IV) and aluminum oxides. Although alternative semiconductor materials, including α-Fe_2O_3, CdS, SnO_2, and $SrTiO_3$, have been explored for photocatalytic ap-

plications, their widespread implementation is often constrained by toxicity and environmental concerns. In contrast, titanium (IV) and aluminum oxides are non-toxic, chemically stable, cost-effective, and readily produced on an industrial scale, making them particularly attractive for sustainable and large-scale technological applications.

Photocatalytic performance of semiconductor materials can be enhanced through several approaches: doping with transition metals (Pt, Pd, Au, Ni, Cr, Mo, Nb, W, Mn, Fe, Ce, Co, etc.), modifying surfaces with polymers or dyes, or employing mixed binary and ternary metal oxide systems [2]. A critical factor in improving coating performance is the incorporation of *d*- and *p*-elements into the oxide matrix [3]. In this regard, particular attention is directed to electrode materials based on vanadium and tungsten oxides [4–7]. These systems hold great promise for diverse applications, including heterogeneous catalysis, photocatalysis, semiconductor devices, and as electrode materials for electrolytic hydrogen and oxygen evolution reactions [8–10]. This context has defined the focus of the present study. The purpose of this study is to investigate the properties of heterooxide coatings formed on titanium and aluminum substrates, with the aim of expanding their use as photocatalytic and electrode materials. This requires examining the positive effects of incorporating complex vanadium and tungsten oxides into titanium and aluminum oxide films.

It is well established that the crystal lattices of tungsten and vanadium oxides often deviate from ideal stoichiometry, resulting in oxygen deficiencies that significantly enhance their electrochemical activity [11]. The high concentration of oxygen vacancies, together with the existence of multiple structural polymorphs–including cubic, hexagonal, orthorhombic, and monoclinic phases–suggests that coatings based on these oxides can exhibit pronounced catalytic and photocatalytic behavior. The efficiency of photocatalytic processes is strongly influenced by several factors, such as the specific surface area of the catalyst, the nature and density of surface-active sites, and the spatial localization and lifetime of photogenerated charge carriers. These properties are, in turn, governed by the crystalline structure of the material, the synthesis route employed, and any subsequent post-treatment of the active layer [12,13].

2. Experimental

PEO coatings were prepared on titanium alloy VT1-0 and aluminum A0 (Al – 99 wt.%). Sample preparation for anodizing included degreasing in a sodium carbonate solution at 40–60 °C, followed by etching: titanium samples in a nitric acid–hydrofluoric acid mixture (1:3) and aluminum samples in nitric acid at room temperature. Samples were then rinsed in running and distilled water.

Previous studies [14] indicated that coatings formed in potassium pyrophosphate solutions with concentrations ≥0.5 mol/dm³ exhibit optimal functional properties. Therefore, further experiments were carried out using electrolytes with constant pyrophosphate content and varying Na_2WO_4 (0.05–0.15 M) and NH_4VO_3 (0.1–0.15 M) concentrations. Electrolytes were prepared by dissolving tungsten and vanadium salts in distilled water, mixing them, and gradually adding the mixture to the base pyrophosphate solution under stirring. The pH was monitored with a pH-meter pH-150M and glass electrode ESL-6307. Due to vanadate's low solubility, dissolution was performed at 40–50 °C. At pH 8–10, sodium tungstate and ammonium metavanadate are fully hydrolyzed, with the $[HVO_4]^{2-}$ anion in equilibrium with the pervanadate ion $[V_2O_7]^{4-}$. Under PEO conditions, high temperatures induce transformations of these anions into V_2O_5 and WO_3, which are incorporated into the coating surface layers [15].

Oxidation was performed in a single stage at current densities of 10–40 A/dm² and a maximum voltage U_{phase} = 80–140 V for 10–20 min, with continuous stirring and electrolyte cooling. A B5-50 DC power supply was used for polarization. After anodizing, samples were rinsed with distilled water and dried at room temperature.

The chemical composition of the coatings was determined by X-ray fluorescence using a portable "SPRUT" spectrometer, with a relative standard deviation of 10^{-3}–10^{-2}. Measurements were taken at a minimum of three points per sample and averaged, with an error of ±1 wt.%. For verification, energy-dispersive X-ray spectroscopy was performed using an Oxford INCA Energy 350 electron probe microanalyzer (15 keV electron beam). Surface morphology was examined using a ZEISS EVO 40XVP scanning electron microscope (G.V. Karpenko Institute of Physics, NASU). Secondary electron imaging allowed high-resolution and high-contrast visualization at 100–5000× magnification. Images were processed with SmartSEM software [16].

Photocatalytic activity was tested via the model oxidation of methyl orange (MO) in a 50 mL thermostatic glass photoreactor with magnetic stirring (100 rpm) at room temperature under air. Initial MO concentrations ranged from (0.02–2.0) ×

10^{-4} mol/dm³. Samples coated with hetero-oxide films were irradiated with a UV lamp DRT-125-1 (230–400 nm, 125 W) placed 5 cm above the solution. Solutions were pre-equilibrated in the dark for 60 min to establish adsorption equilibrium, then irradiated for 80 min. MO concentration was measured every 10 min using a KFK-2 spectrophotometer at λ = 490 nm. The degree of MO decomposition was calculated as $(C_o–C_t)/C_o$, where C_t is the current concentration and C_o is the initial concentration.

Electrocatalytic properties were studied by linear voltammetry in a neutral model medium (1 M Na_2SO_4, pH 7) using a MTech PGP-550S potentiostat–galvanostat in a thermostated three-electrode cell. A platinum mesh was used as the auxiliary electrode, and a saturated Ag/AgCl electrode (EVL-1M1) as the reference. All potentials were converted to the standard hydrogen electrode (SHE) scale. Electrocatalytic activity in hydrogen evolution was characterized by the exchange current density $j_o(H_2)$, determined from linearized Tafel plots.

3. Results and discussion

Previous studies have demonstrated that the incorporation of d-block elements into metal oxide matrices significantly enhances the catalytic performance of hetero-oxide coatings [17–19]. In the present work, the observed synergistic interaction between tungsten and vanadium oxides in improving the photo- and electrocatalytic activity of oxide films motivated a detailed investigation into the influence of electrolysis conditions, electrolyte composition, and substrate material on these properties.

The formation mechanisms of the composite oxides can be rationalized by considering the atomic radii of the constituent elements: titanium (0.068 nm), aluminum (0.143 nm), vanadium (0.052 nm), and tungsten (0.135 nm). Owing to its relatively small atomic radius, vanadium can readily incorporate into the TiO_2 lattice, partially substituting titanium ions within the oxide structure [20–23]. In contrast, the larger atomic radius of tungsten restricts its incorporation into the bulk oxide lattice, leading to its preferential localization in the near-surface region of the coating.

The presence of tungsten oxides in the surface layer, which are intrinsically less catalytically active, facilitates the formation of vanadium-rich oligomeric domains and intermediate oligomeric structures. These species enhance catalytic performance primarily through structural rather than electronic effects. As a result, tungsten oxides are stabilized in the surface layer in the form of W_xO_y, enabling the formation of multicomponent heterostructured systems such as WO_3–V_2O_5–TiO_2/Ti and WO_3–V_2O_5–Al_2O_3/Al. Previous investigations [24–27] have shown that the emergence of highly reactive surface sites arises from the combined effect of tungsten and vanadium oxides, leading to the generation of surface centers with enhanced catalytic activity.

During PEO of aluminum, high-temperature regions form at breakdown sites, where γ-Al_2O_3 transforms into α-Al_2O_3 (corundum) with a stable cubic lattice, increasing the spark-discharge voltage. Electrolyte penetration into the aluminum matrix at these sites is slower than in titanium, yet the resulting coatings still contain vanadium and tungsten oxides [28, 29].

The formation of complex oxides differs between the two metals, likely due to the differing electrical resistivities of the oxide layers: Al_2O_3 films have resistivity in the range 10^{12}–10^{18} Ω·cm, while titanium films are 10^{10}–10^{12} Ω·cm. At temperatures above 400 °C, Al_2O_3 resistivity decreases by several orders of magnitude [30-38]. PEO monitoring shows that discharge intensity is lower on aluminum samples than on titanium. For titanium, sparking begins at U_{spark} = 60–70 V within 30 s, and the transition to the microarc regime occurs faster at lower voltages (105–120 V) than for aluminum, where U_{spark} = 80–100 V after 60–90 s.

The presence of α-Al_2O_3 complicates the incorporation of electrolyte components into the oxide film, resulting in a lower amount of incorporated elements (Table 1) and influencing the surface morphology of the coatings (Figures 1 and 2).

Table 1 – Composition of hetero-oxide coatings on aluminum and titanium substrates.

Composition of the oxide coating	Elemental mass fraction, %						
	V	W	Al	Ti	O	P	K
$WO_3 – V_2O_5 / Al_2O_3$	0,29	0,12,	46,35	-	52,65	0,59	-
$WO_3 – V_2O_5 / TiO_2$	1,51	2,83	-	27,59	60,99	6,76	0,32

Figure 1 shows that the surface of the WO_3 – V_2O_5 – Al_2O_3 / Al composite is uneven, with crater-like inclusions. In contrast, increasing the tungsten content in the WO_3 – V_2O_5 – TiO_2 / Ti coating produces a uniform, fine-grained structure without large agglomerates (Figure 2).

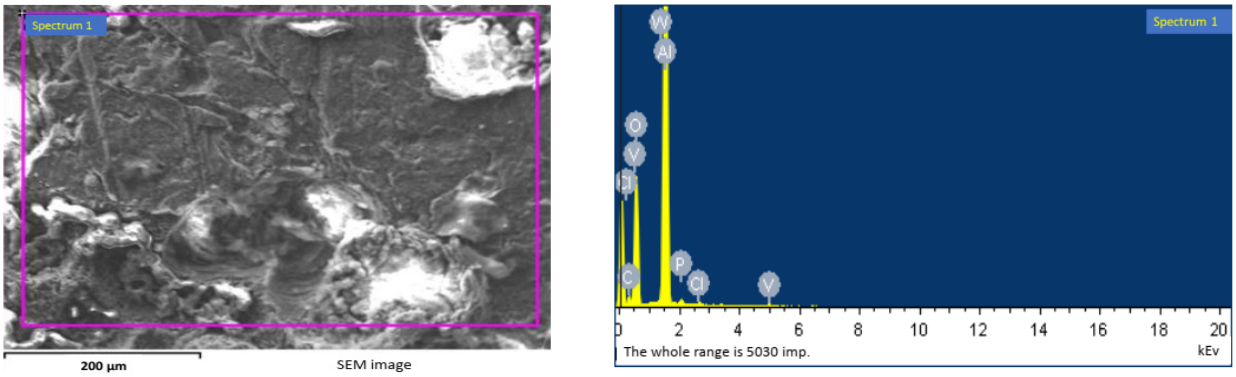

a) b)

Figure 1 – Morphology (a) and X-ray spectrum (b) of the composite surface on an aluminum substrate.

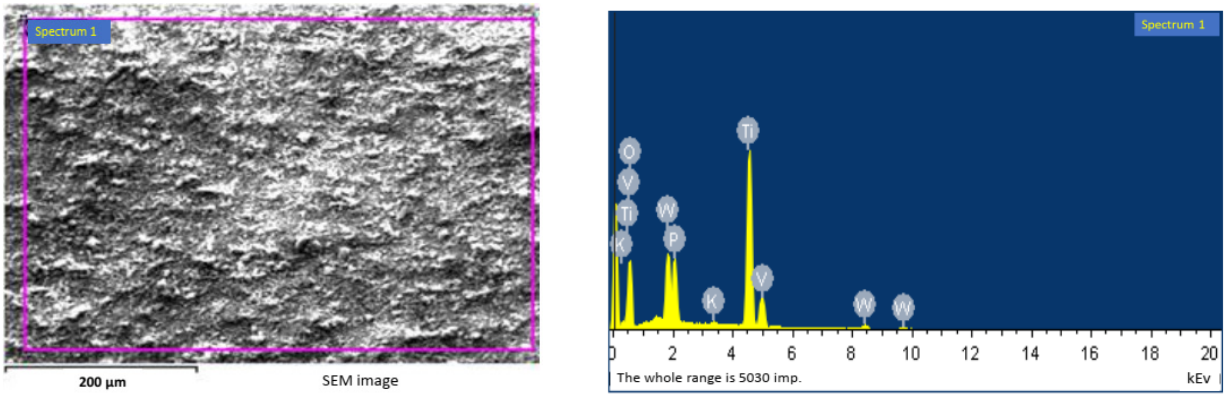

a) b)

Figure 2 – Morphology (*a*) and X-ray spectrum (*b*) of the composite surface on a titanium substrate.

The photocatalytic performance of the hetero-oxide coatings was assessed by tracking the temporal degradation of methyl orange (MO) in aqueous solutions. The results of these photocatalytic activity tests are presented as histograms in Figure 3.

The results indicate that the ratio of dopant metals has a significant impact on the photocatalytic activity of hetero-oxide coatings on aluminum substrates. Increasing the vanadium content in the electrolyte, however, reduces the photocatalytic activity of the hetero-oxide coatings on both aluminum and titanium. This effect can be explained by the sequence of oxide layer formation on the metal surfaces. V_2O_5 forms much more rapidly than WO_3 during oxidation reactions [22]. At high VO_3^- concentrations in the electrolyte, the accelerated formation of V_2O_5 hinders the uniform deposition of WO_3 on the coating surface, while WO_3 predominantly forms inside pores, reducing the exposed catalytically active surface area. Therefore, the optimal dopant ratio is 1:1.

The time-dependent degradation profiles of MO for mono-oxide coatings and hetero-oxide coatings prepared from electrolytes with a V:W ratio of 1:1 are shown in Figure 4.

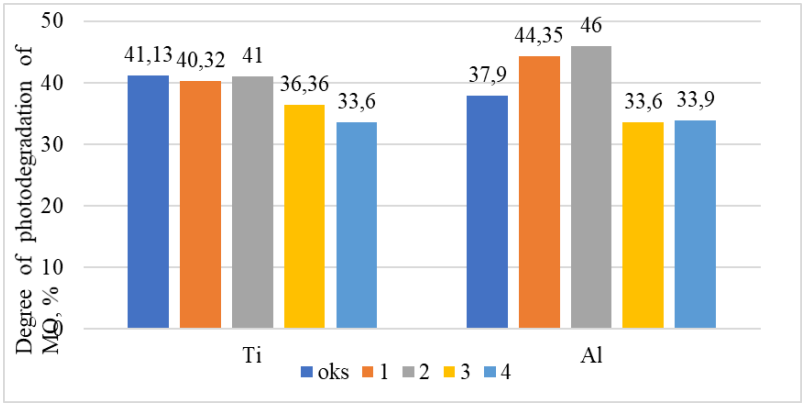

Figure 3 – Photocatalytic properties of coatings on aluminum and titanium substrates: mono-oxide coatings (ox) and hetero-oxide coatings obtained by PEO in electrolytes with V/W ratios of 1:3 (1), 1:1 (2), 2:1 (3), and 3:1 (4).

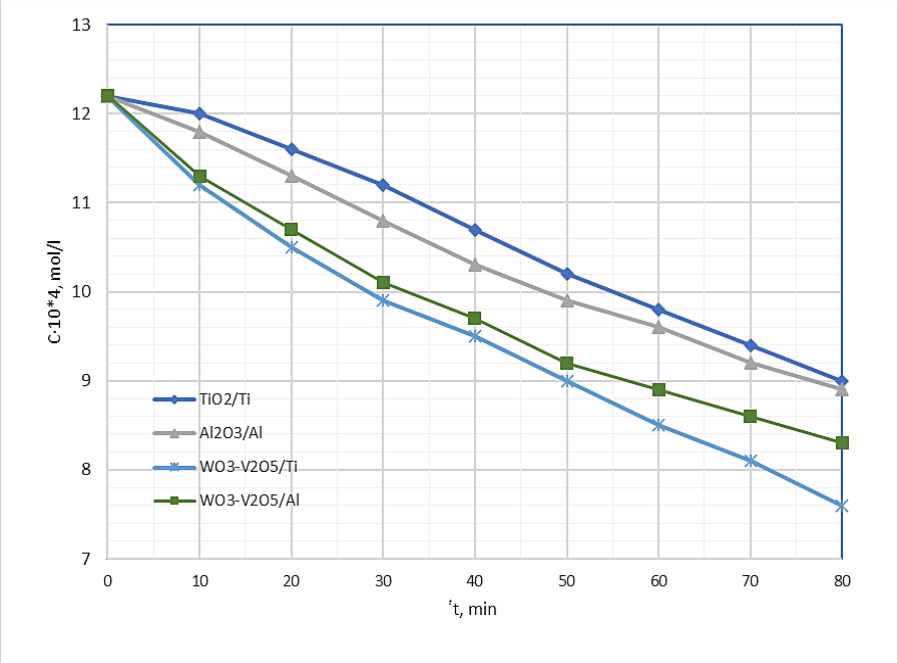

Figure 4 – Time-dependent profiles of photocatalytic degradation of MO in contact with mono- and hetero-oxide coatings (V:W ratio = 1:1).

Comparison of the coatings in the MO degradation reaction shows that doped hetero-oxide coatings exhibit significantly higher photocatalytic activity than mono-oxide coatings, demonstrating their potential for eco-technological applications.

The electrocatalytic activity of the hetero-oxide coatings was assessed using kinetic parameters from a model hydrogen evolution reaction. The hydrogen reduction potential and polarization behavior were found to depend on the coating composition, the nature of the substrate metal, and the pH of the medium. The presence of non-stoichiometric oxides, compositional variability, surface morphology, and the degree of surface development result in electrocatalytic properties of the hetero-oxide coatings that differ markedly from those of the pure metals (Figure 5).In a neutral medium, hydrogen evolution begins at –1.15 V on aluminum coatings and at –0.95 V on titanium coatings, indicating a reduction in hydrogen overpotential. The electrocatalytic activity of the coatings is characterized by the Tafel slope (b), determined from the linear portion of the Tafel plot (Figure 5, Table 2).

Lower b values indicate faster reaction kinetics. In this study, the observed b values differ from classical trends relating hydrogen evolution overpotential to current density and electrode material, reflecting the unique electrocatalytic behavior of the hetero-oxide coatings.

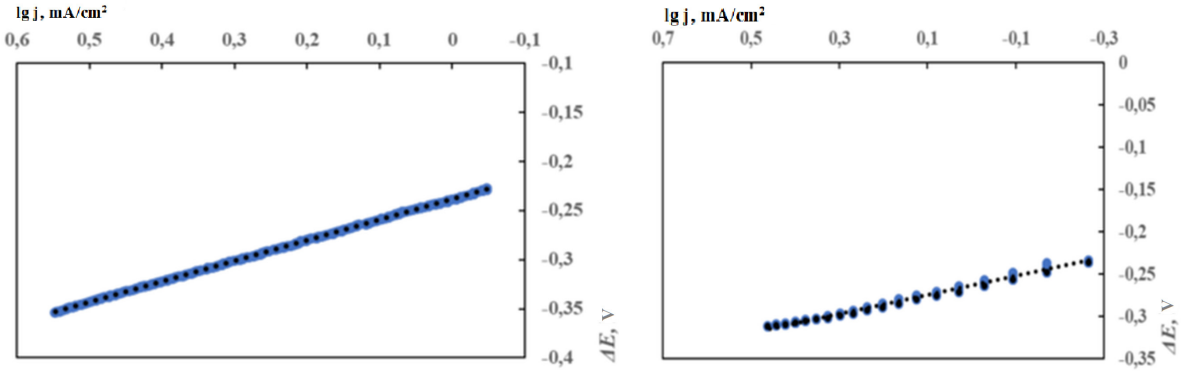

a) b)

Figure 5 – Linear regions of the polarization curves for the hydrogen evolution reaction in Tafel coordinates on $WO_3 – V_2O_5 – TiO_2$ / Ti (a) and $WO_3 – V_2O_5 – Al_2O_3$ / Al (b) coatings in a neutral 1 M Na_2SO_4 solution. Scan rate: 2 mV/s.

Table 2 – Electrocatalytic parameters of the coatings for hydrogen evolution.

Electrode material	–*a*, B	–*b*, B
Pt	0,31	0,10
Ti	0,82	0,14
Al	0,64	0,14
$WO_3 – V_2O_5 – Al_2O_3$ / Al	0,26	0,11
$WO_3 – V_2O_5 – TiO_2$ / Ti	0,23	0,20

In multicomponent oxide systems, unlike pure metals, the Tafel slope (b) can exceed 0.12 V. In this study, b for the $WO_3 – V_2O_5 – TiO_2$ / Ti composites was –0.20 V. For many metals, b is higher in alkaline solutions than in acidic media during hydrogen evolution; to avoid this effect, a neutral electrolyte was used.

The variation in b is influenced by several factors: the compositional diversity of non-stoichiometric oxides, differences in hydrogen adsorption on the oxide matrix (which can slow electrochemical desorption), and the formation of active centers from dopants (vanadium and tungsten). These factors complicate the hydrogen evolution mechanism on hetero-oxide surfaces and merit further investigation.

The Tafel constant a for $WO_3 – V_2O_5 – Al_2O_3$ / Al was –0.26 V (Table 2), close to that of $WO_3 – V_2O_5 – TiO_2$ / Ti (–0.23 V), and both values fall within the range typical for catalytically active materials. The slight difference in a arises from variations in the hetero-oxide matrix and the tungsten and vanadium oxide content. A higher proportion of non-stoichiometric tungsten and vanadium oxides in titanium-based coatings further lowers a. Overall, these results indicate the exceptionally high electrocatalytic activity of the hetero-oxide composites in hydrogen evolution, confirming their strong potential for practical applications.

4. Conclusion

Highly active hetero-oxide photocatalytic coatings were successfully synthesized on aluminum- and titanium-based substrates via plasma electrolytic oxidation incorporating vanadium and tungsten spe-

cies. The resulting materials demonstrated excellent functional performance across multiple application domains.

Evaluation of photocatalytic activity using methyl orange degradation revealed significantly enhanced reaction rates, confirming the strong potential of these coatings for environmentally oriented and eco-technological applications.

Electrochemical studies of hydrogen evolution reactions showed that the synthesized hetero-oxide composites exhibit exceptionally high electrocatalytic activity, underscoring their promise as efficient electrode materials for electrolytic hydrogen production.

The functional properties of the coatings exhibited a strong dependence on the dopant content, the characteristics of the metallic matrix, and the surface morphology.

(iv) Analysis of the Tafel parameters further confirmed the superior electrocatalytic characteristics of the coatings, supporting their applicability in practical hydrogen generation systems.

References

1. Friedemann A.E.R., Gesing Th.M., Plagemann P. Electrochemical rutile and anatase formation on PEO surfaces // Surface and Coatings Technology. – 2017. – Vol. 315. – P. 139-149. https://doi.org/10.1016/j.surfcoat.2017.01.042

2. Chakravorty A., Roy S. A review of photocatalysis, basic principles, processes, and materials // Sustainable Chemistry for the Environment. – 2024. – Vol. 8. – Art. 100155. https://doi.org/10.1016/j.scenv.2024.100155

3. Wu K.-R., Hung Ch.-H.J., Yeh Ch.-W., Wu J.-K. Microporous TiO_2-WO_3/TiO_2 films with visible-light photocatalytic activity synthesized by micro arc oxidation and DC magnetron sputtering // Applied Surface Science. – 2012. – Vol. 263. – Pp. 688-695. https://doi.org/10.1016/j.apsusc.2012.09.142

4. Lukiyanchuk I.V., Vasilyeva M.S., Yarovaya T.P., Nedozorov P.M., Tkachev V.V., Ustinov A.Yu., Budnikova Yu.B., Parotkina Yu.A. Photoactive TiO_2-V_2O_5-WO_3 film composites immobilized in titanium phosphate matrix by plasma electrolytic oxidation // Journal of Photochemistry and Photobiology A: Chemistry. – 2023, – Vol. 445. – Art. 11504. https://doi.org/10.1016/j.jphotochem.2023.115047

5. Lukiyanchuk I.V., Vasilyeva M.S., Ustinov A.Yu., Bryzhin A.A., Tarkhanova I.G. Ti/TiO_2/$NiWO_4$ + WO_3 composites for oxidative desulfurization and denitrogenation // Surface and Coatings Technology. – 2022. – Vol. 434. – Art. 128200. https://doi.org/10.1016/j.surfcoat.2022.128200

6. Hatel R., Baitoul M. Nanostructured Tungsten Trioxide (WO_3): synthesis, structural and morphological investigations // IOP Conf. Series: Journal of Physics: Conf. Series. – 2019. – Vol. 1292. – Art. 012014. https://doi.org/10.1088/1742-6596/1292/1/012014

7. He J., Luo Q., Cai Q.Z., Li X.W., Zhang D.Q. Microstructure and photocatalytic properties of WO_3/TiO_2 composite films by plasma electrolytic oxidation // Materials Chemistry and Physics. – 2011. – Vol. 129. – Pp. 242-248. https://doi.org/10.1016/j.matchemphys.2011.04.011

8. Javidi M., Fadaee H. Plasma electrolytic oxidation of 2024-T3 aluminum alloy and investigation on microstructure and wear behavior // Applied Surface Science. – 2013. – Vol. 286. – Pp. 212-219. https://doi.org/10.1016/j.apsusc.2013.09.049

9. Bairachnyi V., Rudenko N., Zhelavska Yu., Pilipenko A. Using aluminum alloys in the electrochemical hydrogen production // Materials Today: Proceedings. – 2019. – Vol. 6. – Pp. 299-304. https://doi.org/10.1016/j.matpr.2018.10.108

10. Ved M.V., Sakhnenko N.D., Karakurkchi A.V., Myrna T.Yu. Functional mixed cobalt and aluminum oxide coatings for environmental safety // Functional materials. – 2017. – Vol. 24. – Pp. 303–310. https://doi.org/10.15407/fm24.02.303

11. Curran J.A., Clyne T.W. Porosity in plasma electrolytic oxide coatings // Acta Materialia, – 2006. – Vol. 54. – Pp. 1985-1993. https://doi.org/10.1016/j.actamat.2005.12.029

12. Paiu M., Lutic D., Favier L., Gavrilescu M. Heterogeneous photocatalysis for advanced water treatment: Materials, mechanisms, reactor configurations, and emerging applications // Applied Science. – 2025. – Vol. 15. – P. 5681. https://doi.org/10.3390/app15105681

13. Bozheyev F., Nemkayeva R., Yerlanuly Y., Gabdullin M., Markhabayeva A. Performance of transition metal oxides for solar hydrogen conversion // ACS Catalysis. -2025. -Vol.15, -No.18. -Pp. 16449-16162. https://doi.org/10.1021/acscatal.5c03869

14. Karakurkchi A., Sakhnenko M., Korogodskaya A., Zyubanova S. Development of an approach to improvement the protection of the population in protective buildings of civil protection in the conditions of air pollution by toxic chemical agents // Technology Audit and Production Reserves. – 2022. – Vol. 1. – Pp. 6–11. http://doi.org/10.15587/2706-5448.2022.253650

15. Tseng Ch.-Ch., Lee J.-L., Kuo Tz.-Hs., Kuo Sh.-N., Tseng K.-H. The influence of sodium tungstate concentration and anodizing conditions on microarc oxidation (MAO) coatings for aluminum alloy // Surface and Coatings Technology. – 2012. – Vol. 206. – Pp. 3437-3443. https://doi.org/10.1016/j.surfcoat.2012.02.002

16. Sakhnenko N.D., Ved M.V. & Karakurkchi A.V. Nanoscale oxide PEO coatings forming from diphosphate electrolytes // In: Springer proceedings in physics. – 2017. – Pp. 507–531. https://doi.org/10.1007/978-3-319-56422-7_38

17. Sakhnenko M., Stepanova I., Korogodskaya A., Karakurkchi A., Skrypnyk O., Dzheniuk A. & Halak O. Patterns in the electrochemical synthesis of thin-film photocatalytic materials based on titanium heterooxide compounds // Eastern-European Journal of Enterprise Technologies. – 2022. – Vol. 6. – Pp. 30-39. https://doi.org/10.15587/1729-4061.2022.269942

18. Pizzini S. Physical chemistry of semiconductor materials and processes. Wiley. – 2015. 416 p.

19. Jaegers N.R., Lai J.-K., He Y., Walter E., Dixon D.A., Vasiliu M., Chen Y., Wang C., Hu M.Y., Mueller K.T., Wachs I.E., Wang Y., Hu J.Z. Mechanism by which tungsten oxide promotes the activity of supported V_2O_5/TiO_2 catalysts for NO_X abatement: Structural effects revealed by ^{51}V MAS NMR spectroscopy // Angewandte Chemie. – 2019. – Vol. 58. – Art. 12609. https://doi.org/10.1002/anie.201904503

20. Bayati M.R., Zargar H.R., Molaei R., Golestani-Fard F., Zanganeh N., Kajbafvala A. MAO-synthesized Al_2O_3-supported V_2O_5 nano-porous catalysts: Growth, characterization, and photoactivity // Applied Surface Science. – 2010. – Vol. 256 – Pp. 3806-3811. https://doi.org/10.1016/j.apsusc.2010.01.030

21. Abyzov A.M. Aluminum Oxide and Alumina Ceramics (review). Part 1. Properties of Al_2O_3 and commercial production of dispersed Al_2O_3 // Refractories and Industrial Ceramics. – 2019. – Vol. 60. – Pp. 24–32. https://doi.org/10.1007/s11148-019-00304-2

22. Karbasi M., Nikoomanzari E., Hosseini R., Bahramian H., Chaharmahali R., Giannakis S., Kaseem M., Fattah-Alhosseini A. A review on plasma electrolytic oxidation coatings for organic pollutant degradation: How to prepare them and what to expect of them? // Journal of Environmental Chemical Engineering. – 2023. – Vol. 11. – P. 110027. https://doi.org/10.1016/j.jece.2023.110027

23. Narivs'kyi O., Atchibayev R., Kemelzhanova A., Yar-Mukhamedova G., Snizhnoi G., Subbotin S., & Beisebayeva A. Mathematical modeling of the corrosion behavior of austenitic steels in chloride-containing media during the operation of plate-like heat exchangers // Eurasian Chemico-Technological Journal. – 2002. – Vol. 24(4). – P. 295-302. https://doi.org/10.18321/ectj1473

24. Sagyndykov A.B., Kalkozova Z.K., Yar-Mukhamedova G.S., Abdullin K.A. Fabrication of nanostructured silicon surface using selective chemical etching // Technical Physics. – 2017. – Vol. 62(11). – Pp. 1675-8. https://doi.org/10.1134/S106378421711024X

25. Mussabek G., Lysenko V., Yermukhamed D., Sivakov V., Timoshenko V. Yu. Thermally induced evolution of the structure and optical properties of silicon nanowires // Results in Physics. -2020. –Vol.18, -Art. 103258. https://doi.org/10.1016/j.rinp.2020.103258

26. Aldabergenova T.M., Kislitsin S.B., Larionov A.S., Yar-Mukhamedova G.S. Effect of low-energy alpha-particles irradiation on surface structure and physical-mechanical properties of high-purity tungsten // In AIP Conference Proceedings. – 2016. – Vol. 1783. – Art. 020003. https://doi.org/10.1063/1.4966296

27. Kemelzhanova A, Atchibayev R, Mukasev K, Myrzakul T, Yar-Mukhamedov Y. Nano-coatings protective properties in aminum environments // International Multidisciplinary Scientific GeoConference: SGEM. – 2019. – Vol. 19. – Pp. 297-303. https://doi.org/10.5593/sgem2019/6.1/S24.039

28. Yar-Mukhamedova G.S, Zellele D.M, Rutkowska-Gorczyca M., Makhambet I., Mussabek G., Atchibayev R., Kemelzhanova A. Advancements in coating methods and properties of titanium-based composite coatings: A review // ES Materials and Manufacturing. – 2025. – Vol. 1128. – P. 1569. https://doi.org/10.30919/mm1569

29. Dzhus A., Subbotin S., Pulina T., Snizhnoi G. Modeling the resistance of plate-like heat exchangers made of 06khn28mdt alloy (analogous to aisi904l steel) to crevice corrosion in recycled water enterprises // Physical Sciences and Technology. – 2024. – Vol. 11(3-4). – Pp. 58–66. https://doi.org/10.26577/phst2024v11i2b07

30. Greshta V., Narivskyi O., Dzhus A., Vynar V., Yar-Mukhamedova G., Mukashev K., Beissen N., Mussabek G., Imanbayeva A., Zelele, D., Atchibayev R., & Kemelzhanova A. Corrosion behavior of magnesium alloys NZ30K and NZ30K alloyed with silver in the model solution of the osteosynthesis process // Eurasian Physical Technical Journal. – 2024. – Vol. 21(3(49). – P. 29–36. https://doi.org/10.31489/2024No3/29-36

31. Kemelzhanova A., Zhamanbayeva G., Zakhidov A., Kurmangaliyeva V., Temirgaliyeva E. Nanostructural perostrovskite for photovoltaics // International Multidisciplinary Scientific GeoConference: SGEM. – 2020. – Vol. 20. – Pp. 113-9. https://doi.org/10.5593/sgem2020/4.1/s17.015

32. Mussabek G.K., Yermukhamed D., Dikhanbayev K.K., Mathur S., Sivakov V.A. Self-organization growth of Ge-nanocolums // Materials Research Express, – 2017, – Vol. 4, – Art. 035003. https://doi.org/10.1088/2053-1591/aa5ed6

33. Greshta V. Effect of copper in silver coatings on the corrosion behavior of NZ30K–0.1 wt.% Ag alloy in Ringer–Locke solution // Physical Sciences and Technology. – 2025. – Vol. 12(1-2). – Pp. 95–102. https://doi.org/10.26577/phst20251219

34. Sakhnenko N., Ved M., Koziar M. Ternary cobalt-molybdenum-zirconium coatings: electrolytic deposition and functional properties // Physical Sciences and Technology. – 2018. – Vol. 3(2). – Pp. 65–75. https://doi.org/10.26577/phst-2016-2-108

35. Zellele, D. M., Yar-Mukhamedova, G. S., Rutkowska-Gorczyca, M. A Review on properties of electrodeposited nickel composite coatings: Ni-Al_2O_3, Ni-SiC, Ni-ZrO_2, Ni-TiO_2 and Ni-WC // Materials. – 2024. – Vol. 17(23). – Art. 5715. https://doi.org/10.3390/ma17235715

36. Nenastina T., Sakhnenko M., Oksak S., Yar-Mukhamedova G., Zellele D., Mussabek G., Imanbayeva A. study of complexation patterns in the system Ni^{2+}, MoO_4^{2-}, $P_2O_7^{4-}$, Cit^{3-} for the development of poly-ligand electrolytes (Study of complexation patterns) // Eurasian Chemico-Technological Journal. – 2024. – Vol. 26(3). – Pp. 155-160. https://doi.org/10.18321/ectj1638

37. Dzhus A., Snizhnoi G. Prediction the durability of heat exchangers made of 06KhN28MDT alloy (analogous to AISI904L steel) to crevice corrosion during their operation in recycled water // Physical Sciences and Technology. – 2023. – Vol. 10(3-4). – Pp. 57–67. https://doi.org/10.26577/phst.2023.v10.i2.07

38. Zhilkashinova A., Skakov M., Zhilkashinova A., Abilev, M., Prokhorenkova N. Features of structural-phase states of Co-Cr-Al-Y composite coatings after heat treatment // Physical Sciences and Technology. – 2022. – Vol. 9 (1-2). – Pp. 45–54. https://doi.org/10.26577/phst.2022.v9.i1.06

Information about authors:

Gulmira Yar-Mukhamedova – Dr. Sci. (Physics and Mathematics), Professor at the Al-Farabi Kazakh National University (Almaty, Kazakhstan, e-mail: gulmira-alma-ata@mail.ru).

Nikolay Sakhnenko – Dr. Sci. (Physics and Mathematics), Professor at National Technical University "Kharkiv Polytechnic Institute" (Kharkiv, Ukraine, e-mail: nicksakhnenko@gmail.com).

Alla Korogodskaya – Candidate of Sciences (Physics and Mathematics), Associate Professor at the National Technical University "Kharkiv Polytechnic Institute" (Kharkiv, Ukraine, e-mail: korogodskaya@kpi.kharkov.ua).

Irina Stepanova – Candidate of Science (Physics and Mathematics), Associate Professor at National Technical University "Kharkiv Polytechnic Institute" (Kharkiv, Ukraine, e-mail: stepanova_i@kpi.kharkov.ua).

Anna Karakurkchi – Dr. Sci. (Physics and Mathematical), Professor at National Defense University of Ukraine (Kyiv, Ukraine, e-mail: anyutikukr@gmail.com).

William Yi Wang – PhD, Professor at the Northwestern Polytechnical University (Xi'an, Shaan Xi, China, e-mail: wywang@nwpu.edu.cn).

Daniel Zellele – PhD student (Materials Science and Technology of New Materials) at the Al-Farabi Kazakh National University (Almaty, Kazakhstan, e-mail: danielmekonnenz@gmail.com).

Akmaral Imanbayeva – Candidate of Physics and Mathematical Sciences, Senior Lecturer at the Department of Electronics and Astrophysics, Al-Farabi Kazakh National University (Almaty, Kazakhstan, e-mail: akmaral@physics.kz).

IRSTI 29.19.31 https://doi.org/10.26577/phst20251225

$ZnCo_2O_4$ nanostructure-based electrochemical sensor for highly sensitive glucose detection

L.V. Gritsenko[1, 2]*, Zh.K. Kalkozova[1, 3], Y.Y. Kedruk[4], Zh.U. Paltusheva[2], M.N. Mussakhanov[4] and Kh.A. Abdullin[1, 3]

[1]Institute of Applied Sciences and Information Technologies, Almaty, Kazakhstan
[2]Satbayev University, Almaty, Kazakhstan
[3]National Nanotechnology Laboratory of Open Type, Al-Farabi Kazakh National University, Almaty, Kazakhstan
[4]Kazakh-British Technical University, Almaty, Kazakhstan
*e-mail: l.gritsenko@satbayev.university

(Received August 22, 2025; received in revised form November 16, 2025; accepted November 30, 2025)

Enzyme-free electrochemical glucose sensors attract the attention of researchers due to their high reproducibility and stability compared to enzymatic sensors, which is of practical importance for both clinical diagnostics and the food industry. The development of an economical, controlled method for the synthesis of a multicomponent composite used to determine glucose is an urgent task for the prevention and treatment of diabetes. In this work, zinc cobaltite $ZnCo_2O_4$ nanostructures on nickel foam were synthesized using a simple hydrothermal method. The possibility of using the grown structures as a basis for enzyme-free electrochemical sensors for determining glucose is shown. It was revealed that the concentration of the growth solution affects the morphology of the synthesized structures and their electrochemical properties. The highest sensitivity to glucose 18.65 $mA \cdot mM^{-1} \cdot cm^{-2}$ in an alkaline solution of 0.1 M KOH was demonstrated by $ZnCo_2O_4$ samples grown in an aqueous solution containing 40 mM zinc nitrate and 400 mM cobalt nitrate. The results of the study show that the molar predominance of cobalt nitrate in the growth solution contributes to an increase in the electrochemical sensitivity of Ni-$ZnCo_2O_4$ electrodes. The obtained samples can be used as highly sensitive electrodes used both in medical applications and for the needs of the food industry.

Keywords: nanostructured composites, electrochemical biosensor, hydrothermal method, glucose, cyclic voltammetry, oxide semiconductors.
PACS number(s): 61.46.+w, 61.46.−w, 61.82.Fk, 68.37.Lp, 81.07.Bc, 81.10.Dn, 82.47.Rs.

1. Introduction

Diabetes, a serious chronic disease, is a public health problem. The number of recorded cases of this disease is steadily increasing. In this regard, the development of efficient, cost-effective, and highly glucose-sensitive biosensors is an urgent task [1-5]. Due to instability, high cost and complexity of immobilization in the development of enzyme sensors, the development of enzyme- free glucose sensors attract special interest of researchers [6-9]. Nanostructured noble metals such as Pt, Au, etc. are actively used for non-enzymatic glucose sensing [10-13]. The disadvantage of these sensors is that some noble metals are easily poisoned by intermediates formed during glucose oxidation, as well as chlorine ions in the test solution. An alternative to noble metals for glucose electrooxidation is transition metal nanostructures and their oxides, which are promising due to their large surface area, low cost, and unique electrocatalytic properties [14-16]. In particular, bimetallic oxide $NiCo_2O_4$ has been actively used because of its high electrical conductivity as well as high electrocatalytic activity compared to single metal oxides such as NiO, Co_3O_4 and CuO [17-20]. However, disadvantages such as brittle structure, easy self-agglomeration and dissolution on the electrode surface make it very difficult to use $NiCo_2O_4$ for glucose determination [17, 21 – 23].

Zinc cobaltite $ZnCo_2O_4$ is a well-known ternary spinel oxide possessing a high degree of cation disorder in two types of lattice sites tetrahedrally or octahedrally coordinated by oxygen [23]. It is a promising p-type functional material attracting considerable interest in potential applications such as lithium ion batteries, electrocatalysts, supercapacitors, etc. due to its electrochemical and catalytic properties [24-27]. In the $ZnCo_2O_4$ crystal Zn cations occupy tetrahedral positions, Co cations are uniformly distributed throughout the octahedral positions, and anions O_2 tend to coordinate both Zn^{2+} and Co^{3+} cations tetrahedrally and octahedrally, respectively, forming a closely packed structure [28, 29].

The fabrication of nanoparticle arrays is relevant in applications where important electrochemical processes take place. The morphology of the electrodes having a strong influence on their properties [30 – 34]. Nanostructured samples have enhanced reactivity and stability, providing pathways for electrolyte ions and electrons, thereby realizing maximum utilization of the electrochemical properties of the material [32 – 39]. The hydrothermal method is an inexpensive low-temperature synthesis method of nanostructured materials based on oxide semiconductors, which are promising for use in biosensors for solving healthcare problems, for chemical and biological analysis, monitoring of the ecological state of the environment, and in the food industry [9, 40]. To create a highly sensitive enzyme-free electrochemical sensor for the detection of glucose in alkaline solution, the use of nanostructured materials is promising [7, 14, 21, 22].

This paper presents the results of a study of the electrochemical properties of nanostructured composite materials based on $ZnCo_2O_4$ spinel synthesized by a low-cost hydrothermal method on nickel foam substrates. The study is aimed at assessing their potential as sensitive electrodes at electrochemical glucose (gl) detection.

2. Materials and methods

Zinc cobaltite samples were obtained by hydrothermal method on nickel foam. The growth solution contained cobalt nitrate $Co(NO_3)_2 \cdot 6H_2O$ (Sigma Aldrich, 99% purity), zinc nitrate $Zn(NO_3)_2 \cdot 6H_2O$ (Sigma Aldrich, 99% purity), and urea CH_4N_2O (Sigma Aldrich, 99% purity). Urea acts as a precipitating agent during hydrothermal synthesis. Six types of samples with different molar concentration ratios of zinc nitrate (NZn) / cobalt nitrate (NCo) are considered in this work: ZC1 (NZn40mM/NCo40mM), ZC2 (NZn60mM/NCo60mM), ZC3 (NZn40mM/NCo400mM), ZC4 (NZn60mM/NCo600mM), ZC5 (NZn400mM/NCo40mM), ZC6 (NZn600mM/NCo60mM) (see Table 1). The hydrothermal synthesis of nanostructures was carried out in a hermetically sealed autoclave at 140 °C for 4 hours. During the synthesis, the nickel foam substrate was placed vertically in the autoclave. At the end of the synthesis, all samples were washed with distilled water and air-dried at 80 °C.

The surface morphology of prepared samples was studied with transmission electron microscope (TEM, JEOL, JEM-1400 plus, Japan) (Fig. 1). The morphology of the sample ZC2 (NZn60mM/NCo60mM) presented in Figure 1a is characterised by nanoparticles in the form of plates or nanorods. The average particle size is of the order of 10-20 nm, which is characteristic of the formation of nanocrystalline spinel structure $ZnCo_2O_4$ during hydrothermal growth. A relatively homogeneous dispersion of crystallites is observed, indicating a close to stoichiometric ratio, as well as balanced conditions of nucleation and growth in solution at a molar ratio of Zn:Co = 1:1. This morphology is favourable for the formation of a developed specific surface area, which is critical for applications in sensing devices and electrochemical systems. Figure 1b shows a snapshot of sample ZC6 (NZn600mM/NCo60mM) synthesised at a precursor ratio of Zn:Co = 10:1. In contrast to sample ZC2, this material shows more pronounced aggregation and formation of larger crystallites (— 30-40 nm), indicating enhanced crystallite growth under zinc excess conditions. Apparently, high Zn^{2+} content leads to a change in the kinetics of hydrolysis and precipitation, while maintaining the nanocrystalline structure characteristic of spinels, but with a lower specific surface area compared to the ZC2 sample.

3. Results and discussion

Thus, by varying the molar ratios of Zn^{2+}/Co^{2+} in the growth solution, the morphology of $ZnCo_2O_4$ nanostructures can be controlled. At a stoichiometric ratio (1:1), the formation of uniform nanoparticles with high dispersion is observed, whereas at a significant excess of zinc (10:1), aggregation and crystallite growth are enhanced, leading to enlarged nanostructures.

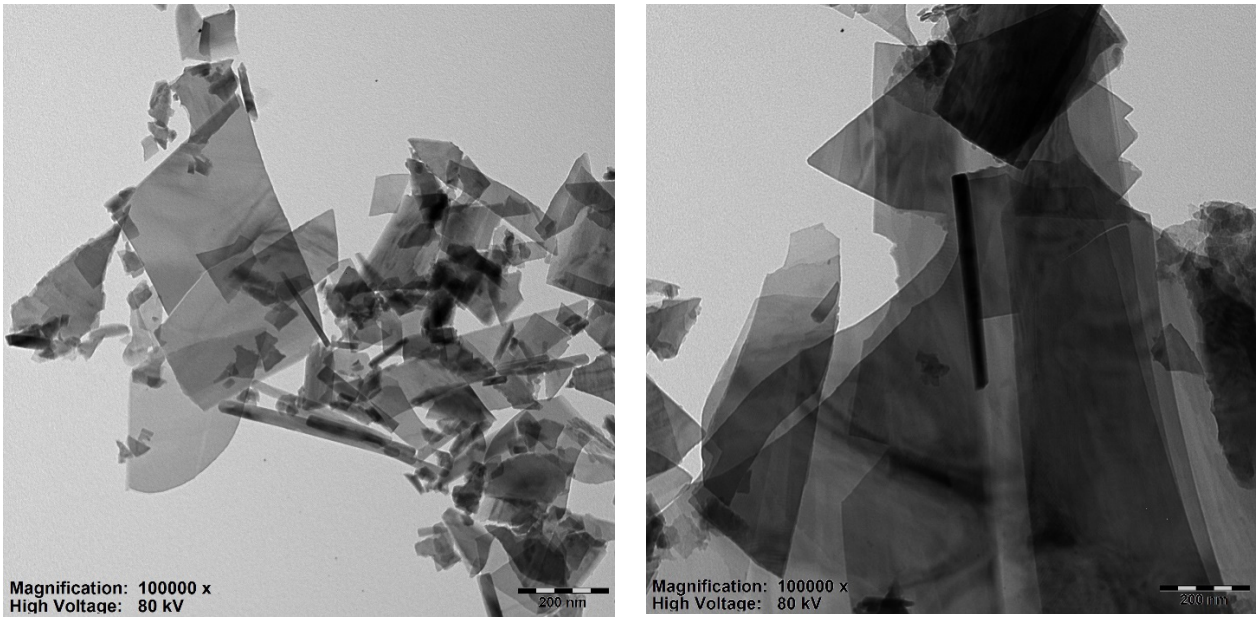

(a) (b)

Figure 1 – TEM of $ZnCo_2O_4$ samples: (a) ZC2, (b) ZC6.

The electrochemical properties of the obtained samples were investigated on a Corrtest CS310 single-channel potentiostat using a three-electrode electrochemical glass cell in 0.1M KOH alkaline solution at a scan rate of 25 mV/s. Cyclic voltammetry (CV) was measured at room temperature at potential changes from -0.1 to 0.65 V. An Ag/AgCl reference electrode was used for electrochemical measurements in a three-electrode setup.

The concentration of glucose in the alkaline solution varied from 0.2 mM to 2 mM. Figure 2 shows the CVs of the synthesized samples. It is observed that maximum oxidation currents are observed at ~0.6 V and maximum reduction currents are observed at ~0.3 V. The peaks of oxidation and reduction currents gradually increase with increasing concentration of glucose in solution.

The corresponding redox potentials indicate that the synthesised material is $ZnCo_2O_4$ [41]. It is observed that the anodic and cathodic peak potentials shift to the positive and negative side, respectively, with increasing glucose concentration in solution, indicating increasing concentration polarization.

The most pronounced anodic currents are observed for samples ZC3 and ZC4 synthesised at excess of cobalt ions (Zn:Co = 1:10). In particular, sample ZC3 (Zn:Co = 40:400 mM) exhibits the highest anodic current upon addition of glucose, indicating high catalytic activity. In contrast, the samples with excess zinc (ZC5 and ZC6) show significantly weaker current responses, indicating that the catalytic efficiency decreases as the proportion of Zn^{2+} in the growth solution increases. To compare the sensitivity of the samples, calibration plots were constructed for the oxidation current peaks as a function of glucose concentration in solution (Figure 3). On the graph R^2=0.99, linear range 0–2 mM. All dependences have a linear character in the investigated range, which confirms the suitability of these materials for quantitative determination of glucose.

On the basis of these dependences the sensitivity of each sample was calculated (Table 1). It was observed that the highest sensitivity (18.65 $mA \cdot mM^{-1} \cdot cm^{-2}$) is demonstrated by sample ZC3, obtained at low concentration of zinc nitrate and high concentration of cobalt nitrate. Sample ZC4, similar to ZC3 in terms of Zn:Co ratio but with higher concentrations of all reagents, also shows high sensitivity: 15.40 $mA \cdot mM^{-1} \cdot cm^{-2}$. This indicates that the high cobalt content of $ZnCo_2O_4$ promotes the formation of active centres that efficiently catalyse glucose oxidation.

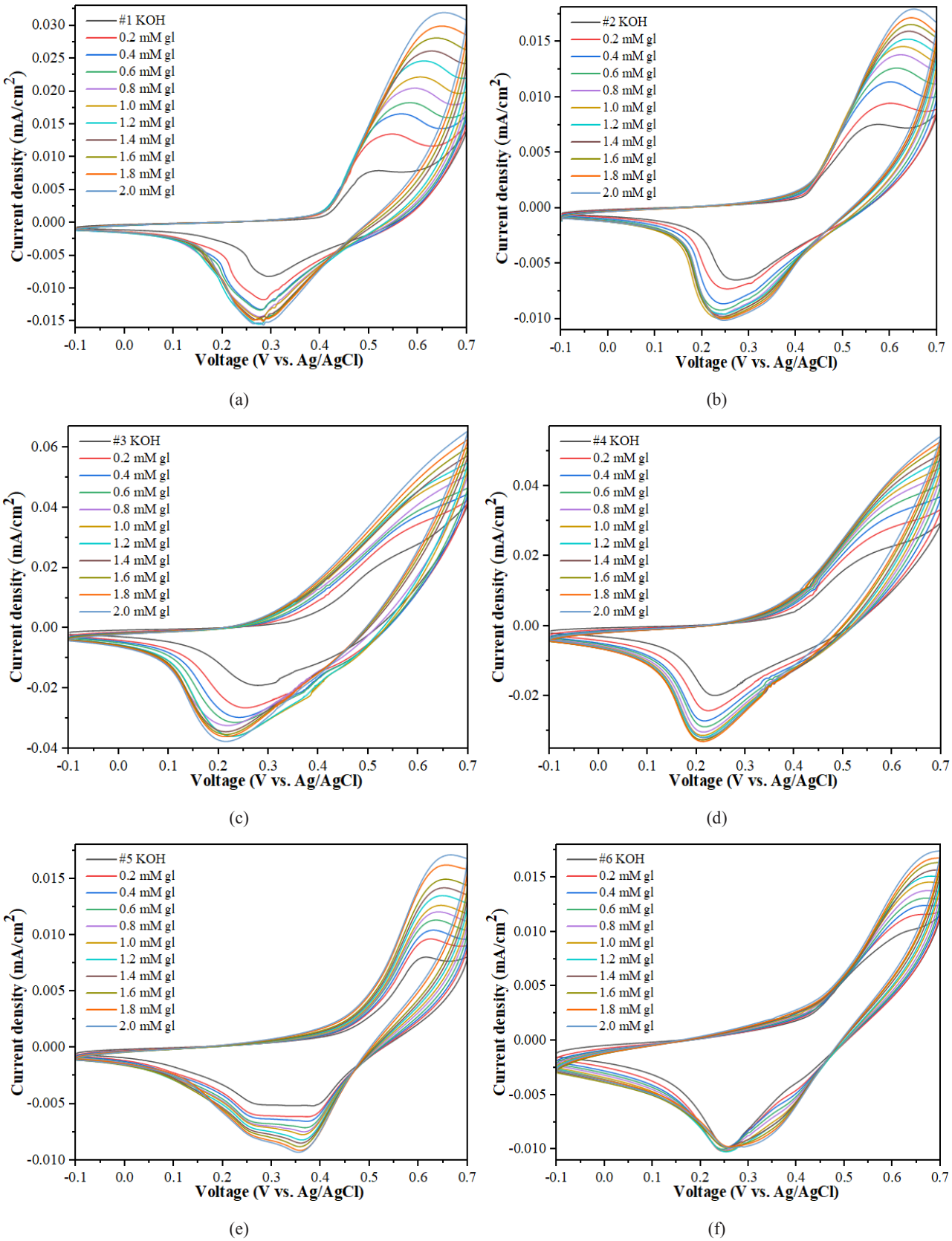

Figure 2 – Cyclic voltammetry patterns of $ZnCo_2O_4$ samples:
(a) ZC1, (b) ZC2, (c) ZC3, (d) ZC4, (e) ZC5, (f) ZC6

In contrast, the samples with excess zinc (ZC5 and ZC6) have the lowest sensitivity: 4.55 and 3.75 $mA \cdot mM^{-1}cm^{-2}$, respectively. This may be due to both less favourable morphology (larger aggregates, lower specific surface area) and lower catalytic activity of Zn-containing phases compared to Co-containing phases. Samples with equimolar ratio of Zn:Co (ZC1 and ZC2) occupy an intermediate position, but at the same ratio the sensitivity decreases with increasing total precursor concentration, possibly due to the densification of the structure and decreased availability of active centres.

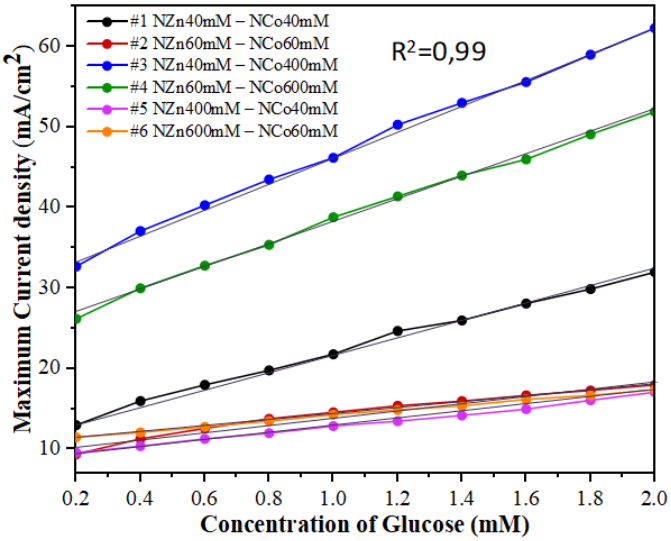

Figure 3 – Plots of variation of peak current density CV at different glucose concentration in alkaline solution of 0.1 M KOH at scanning speed of 25mV/s.

Table 1 – Sensitivity of $ZnCo_2O_4$ samples for glucose detection.

Sample name	Composition of the growth solution	Sensitivity, $mA \cdot mM^{-1} \cdot cm^{-2}$
ZC1	NZn40mM / NCo40mM, urea 100mM	12.05
ZC2	NZn60mM / NCo60mM, urea 150mM	5.25
ZC3	NZn40mM / NCo400mM, urea 100mM	18.65
ZC4	NZn60mM / NCo600mM, urea 150mM	15.40
ZC5	NZn400mM / NCo40mM, urea 100mM	4.55
ZC6	NZn600mM / NCo60mM, urea 150mM	3.75

To obtain more information about the charge transfer efficiency and charge separation at the $ZnCo_2O_4$/Ni interface, electrochemical impedance (EIS) measurement was performed in the range of $0.1 \div 10^5$ Hz at a bias voltage of +0.1 V. Figure 4 shows Nyquist plots between imaginary and real impedance for all $ZnCo_2O_4$ samples of the considered series in 0.1M KOH. The inset of Fig. 4a shows the equivalent Randle circuit, where R1 represents the equivalent series resistance of the electrolyte solution, R2 is the charge transfer resistance and Ws is the Warburg impedance.

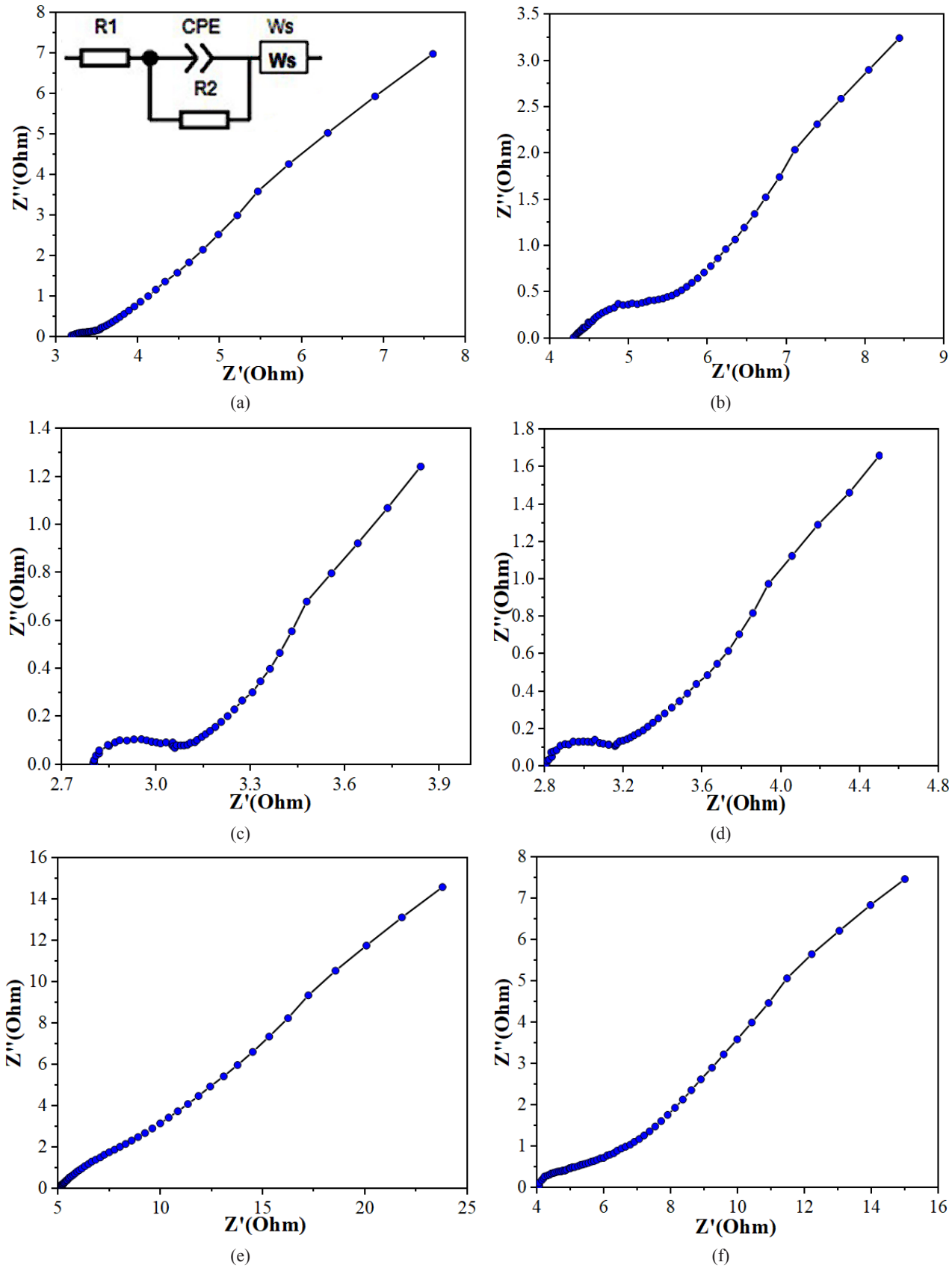

Figure 4 – Nyquist diagrams of $ZnCo_2O_4$ samples:
(a) ZC1, (b) ZC2, (c) ZC3, (d) ZC4, (e) ZC5, (f) ZC6.

CPE (constant phase element) is the circuit element used to describe the capacitance exhibited in real electrochemical systems due to surface roughness or reaction rate distribution. The R2 value for samples ZC2 and ZC4 were compared and found to be 1.21 Ohm and 0.18 Ohm respectively. From Table 1 it can be seen that sample ZC4 with a lower R2 value has a sensitivity 2.5 times higher than sample ZC2. This shows the importance of achieving low R2 values to achieve high sensitivity.

Analysis of Nyquist diagrams shows that all dependences are characterised by the presence of a semicircle in the high-frequency region and a linear section in the low-frequency region. The radius of the semicircle directly correlates with the value of R2: the smaller the radius, the lower the resistance to charge transfer and the higher the kinetics of the electrochemical reaction. The most pronounced small semicircle is observed in the ZC3 sample, indicating the lowest charge transfer resistance among all samples. This is in agreement with the previously obtained cyclic voltammetry data, where sample ZC3 showed the highest sensitivity to glucose. The low R2 indicates high interface conductivity and efficient separation of electron-hole pairs, which is probably due to the high concentration of Co^{3+}/Co^{4+} centres acting as active catalytic sites, as well as favourable morphology promoting rapid charge transfer. The ZC4 sample recorded a close half-circle radius, which also corresponds to a low charge transfer resistance. On the contrary, samples with excess zinc: ZC5 and ZC6 have the largest half-circle radii, indicating high charge transfer resistance and less efficient conduction at the interface, which is consistent with their low sensitivity (Table 1). Apparently, excess Zn^{2+} leads to the formation of less conductive phases or impairs electronic cohesion in the coating, and may also promote particle aggregation, reducing the availability of active centres. Meanwhile, samples with equimolar Zn:Co ratios (ZC1 and ZC2) occupy an intermediate position in terms of half-circle radius value and charge transfer resistance, respectively. The low-frequency linear sections of the diagrams corresponding to the diffusion region also differ in slope. Samples ZC3 and ZC4 show steeper slopes, indicating more efficient mass transfer associated with the diffusion of glucose and OH- ions to the electrode surface, which also confirms their high electrochemical activity.

Thus, the excess of cobalt in the composition promotes the formation of conductive and catalytically active Co^{3+}/Co^{4+} centres, improving the kinetics of the oxidation reaction. The EIS results confirm that controlling the composition of the growth solution allows not only controlling the morphology but also directly influencing the electronic and kinetic characteristics of $ZnCo_2O_4$. The ZC3 sample is of most interest for applications in electrochemical sensors and energy storage devices due to its low charge transfer resistance and high reactivity.

4. Conclusion

The hydrothermal method allowed the preparation of $ZnCo_2O_4$ nanostructures on nickel foam with controlled morphology. Transmission electron microscopy showed that at a molar ratio of Zn:Co = 1:1, uniform nanoparticles with a developed surface are formed. When the zinc content increases, crystallite enlargement and particle aggregation occur, leading to a decrease in the specific surface area of the material. It is shown that the optimal morphological characteristics of $ZnCo_2O_4$ are achieved when the ratio of zinc and cobalt is close to stoichiometric. The electrochemical activity of $ZnCo_2O_4$ nanostructures in the reaction of glucose oxidation in alkaline medium depends significantly on the molar ratio of Zn:Co in the initial growth solution. The samples with excess cobalt (Zn:Co = 1:10) show the highest sensitivity to glucose, which is due to the high catalytic activity of Co^{3+}/Co^{4+} redox couples and, probably, to a more developed surface morphology. Samples with excess zinc show low sensitivity, which is due to the less favourable structure and lower activity of the zinc-containing phases. At higher salt concentrations in the growth solution, a decrease in sensitivity was observed, possibly due to greater particle aggregation. The ZC3 sample (Zn:Co = 40:400 mM) is the most promising for application in non-enzymatic glucose sensors due to its high sensitivity (18.65 $mA \cdot mM^{-1}cm^{-2}$). The electrochemical impedance spectroscopy method showed that the charge transfer resistance R2 depends significantly on the molar ratio of Zn:Co in the growth solution. The lowest R2 was recorded for the ZC3 sample, which correlates with its highest sensitivity to glucose and indicates efficient charge transfer and high catalytic activity.

The results obtained confirm the possibility of controlling the electrochemical properties of $ZnCo_2O_4$ by controlling the composition of the growth solution, which opens prospects for the development of highly sensitive and stable non-enzymatic biosensors based on transition oxides.

Acknowledgements. The study was carried out with the financial support of the Ministry of Science and Higher Education of the Republic of Kazakhstan (grant No AP26103537).

References

1. Liang J., Huang Q., Wu L., Wang L., Sun L., Zhou Zh., Li G. Silicon-based field-effect glucose biosensor based on reduced graphene oxide-carboxymethyl chitosan-platinum nanocomposite material modified LAPS // Sensors and Actuators A: Physical. – 2024. – Vol. 366. – Art. 114937. https://doi.org/10.1016/j.sna.2023.114937

2. Bakranova D., Seitov B., Bakranov N. Photocatalytic and glucose sensing properties of ZnO-based nanocoating// ChemEngineering. – 2023. – Vol. 7. – Art. 22. https://doi.org/10.3390/chemengineering7020022

3. Kumar A., Kumar A., Sagar P., Srivastava M., Pandey A., Prakash R., Srivastava S.K. A sensitive SPR biosensor for glucose detection using MoS_2 quantum dots // Microchemical Journal. – 2025. – Vol. 214. – Art. 113889. https://doi.org/10.1016/j.microc.2025.113889

4. Yojo L.S., Rangel R.C., Duarte P.H., Sasaki K.R.A., Martino J.A. An enzymatic glucose biosensor using the BESOI MOSFET // Solid-State Electronics. – 2024. – Vol. 211. – Art. 108830. https://doi.org/10.1016/j.sse.2023.108830

5. Hamidi H., Murray R., Vezzoni V., Bozorgzadeh S., O'Riordan A., Pontiroli D., Riccò M., Quinn A.J., Iacopino D. A high performance laser induced graphene (LIG) dual biosensor for simultaneous monitoring of glucose and lactate // Biosensors and Bioelectronics: X. – 2025. – Vol. 24. – Art. 100600, https://doi.org/10.1016/j.biosx.2025.100600

6. Ghanbari A.H., Fathi S., Sheikhi M.H., Kordrostami Z. Fabrication of non-enzymatic glucose biosensor based on CuS/Ni_3S_4 reinforced microflowers // Chemosphere. – 2025. – Vol. 382. – Art. 144450. https://doi.org/10.1016/j.chemosphere.2025.144450

7. Jazi H.K., Sarafbidabad M., Henda M.B., Ahmadipour M. The effect of laser surface texturing on ZnO/MWCNT nanocomposite modified screen-printed carbon electrode for non-enzymatic glucose biosensor // Diamond and Related Materials. – 2025. – Vol. 151. – Art. 111845. https://doi.org/10.1016/j.diamond.2024.111845

8. Zhang C., Xu X., Li B., Li H., Tan X., Jesuraj P.J., Xie W. Ultra-sensitive and low detection limitation non-enzymatic glucose biosensor based on heterojunction $NiO@In_2O_3$ hollow nanofibers // Microchemical Journal. – 2025. –Vol. 208. – Art. 112401. https://doi.org/10.1016/j.microc.2024.112401

9. Kalkozova Z.K., Gritsenko L.V., Balgimbayeva U.A., Gabdullin M.T., Wen D., Abdullin Kh.A. New cobalt hydroxycarbonate-based material for highly sensitive enzyme-free glucose sensors // Scientific Reports. – 2025. – Vol. 15. – Art.17154. https://doi.org/10.1038/s41598-025-01164-2

10. Emin A., Ding A., Ali S., Chhattal M., Ali S., Parkash A., Li Q. Electrochemical non-enzymatic glucose biosensors based on Au-thiol-linked molecular architectures // Microchemical Journal. – 2024. – Vol. 207. – Art.111972. https://doi.org/10.1016/j.microc.2024.111972

11. Şavk A., Aydın H., Cellat K., Şen F. A novel high performance non-enzymatic electrochemical glucose biosensor based on activated carbon-supported Pt-Ni nanocomposite // Journal of Molecular Liquids. – 2020. – Vol. 300. – Art. 112355. https://doi.org/10.1016/j.molliq.2019.112355

12. Henry O.E., Hitler L., Udochukwu C.G., Stephen A.A., Ernest C.A., Adedapo S.A. Single-metal (Cu, Ag, Au) encapsulated gallium nitride nanotube (GaNNT) as glucose nonenzymatic nanosensors for monitoring diabetes: Perspective from DFT, visual study, and MD simulation // Journal of Molecular Liquids. – 2023. – Vol. 384. – Art.122209. https://doi.org/10.1016/j.molliq.2023.122209

13. Tuan D.V., Ngan D.T.T., Thao D.V.P., Nguyet N.T., Thuy N.T., Thuy N.P., Thu V.V., Hung V.P., Tam P.D. High-performance nonenzymatic electrochemical glucose biosensor based on AgNP-decorated MoS_2 microflowers // Current Applied Physics. – 2022. – Vol. 43. – Pp. 116-123. https://doi.org/10.1016/j.cap.2022.09.001

14. Mubarakali A., Gopinath S., Parthasarathy P., Kumar U. A., Basha A. A. Highly efficient and sensitive non-enzymatic glucose biosensor based on flower-shaped CuO-colloid nanoparticles decorated with graphene-modified nanocomposite electrode // Measurement. – 2023. – Vol. 217. – Art. 113145. https://doi.org/10.1016/j.measurement.2023.113145

15. Markhabayeva A.A., Moniruddin Md., Dupre R., Abdullin K.A., Nuraje N. Designing of $WO_3@Co_3O_4$ heterostructures to enhance photoelectrochemical performances // The Journal of Physical Chemistry A. – 2020. – Vol. 124. – Pp. 486-491. https://doi.org/10.1021/acs.jpca.9b09173

16. Kalkozova Z.K., Balgimbayeva U.A., Gabdullin M.T., Gritsenko, L.V., Suo G., Abdullin K.A. A facile method for synthesizing cobalt oxide nanoparticles to create a highly sensitive non-enzyme glucose sensor // *Biosensors*. – 2025. – Vol. *15*. – Art. 235. https://doi.org/10.3390/bios15040235

17. Li W.W., Qi H., Wang B.G., Wang Q.Y., Wei S.T., Zhang X.L., Wang Y., Zhang L., Cui X.Q. Ultrathin $NiCo_2O_4$ nanowalls supported on a 3D nanoporous gold coated needle for non-enzymatic amperometric sensing of glucose // Microchim Acta. – 2018. – Vol. 185. – Pp. 1-9. https://doi.org/10.1007/s00604-017-2663-8

18. Ma G.R., Yang M., Li C.Y., Tan H.Y., Deng L., Xie S., Xu F.G., Wang L., Song Y.H. Preparation of spinel nickel-cobalt oxide nanowrinkles/reduced graphene oxide hybrid for nonenzymatic glucose detection at physiological level // Electrochim Acta. – 2016. – Vol. 220. – Pp. 545-553. https://doi.org/10.1016/j.electacta.2016.10.163

19. Yong-Yu L., Ping K., Hong-Qi H., Zhong-Gang L., Gang L., Zheng G., Xing-Jiu H. Porous CuO nanobelts assembly film for nonenzymatic electrochemical determination of glucose with High fabrication repeatability and sensing stability // Sensors and Actuators B: Chemical. – 2020. – Vol. 307. – Art. 127639. https://doi.org/10.1016/j.snb.2019.127639

20. Tian L., He G., Cai Y., Wu S., Su Y., Yan H., Yang C., Chen Y., Li L. Co_3O_4 based non-enzymatic glucose sensor with high sensitivity and reliable stability derived from hollow hierarchical architecture // Nanotechnology. – 2018. – Vol. 29. – Art. 075502. https://doi.org/10.1088/1361-6528/aaa1d2

21. Liu L.J., Wang Z.H., Yang J.H., Liu G.L., Li J.J., Guo L., Chen S.L., Guo Q.H. $NiCo_2O_4$ nanoneedle-decorated electrospun carbon nanofiber nanohybrids for sensitive non-enzymatic glucose sensors // Sens Actuator B Chem. – 2018. – Vol. 258. – Pp. 920-928. https://doi.org/10.1016/j.snb.2017.11.118

22. Xinxin D., Kaili L., Yan X., Mengting Y., Ting G., Jun W. Nonenzymatic electrochemical glucose biosensor constructed by $NiCo_2O_4$@Ppy nanowires on nickel foam substrate // Sensors & Actuators B Chemical. – 2019. – Vol. 292. – Pp.121-128. https://doi.org/10.1016/j.snb.2019.04.107

23. Shewale P.S., Yun K.-S. RGO decorated N-doped $NiCo_2O_4$ hollow microspheres onto activated carbon cloth for high-performance non-enzymatic electrochemical glucose detection // Heliyon. – 2023. – Vol. 9 – Art. e17200. https://doi.org/10.1016/j.heliyon.2023.e17200

24. Kim T.W., Woo M.A., Regis M., Choi K.S. Electrochemical synthesis of spinel type $ZnCo_2O_4$ electrodes for use as oxygen evolution reaction catalysts // J Phys Chem Lett. – 2014. – Vol. 5. – Pp. 2370-2374. https://doi.org/10.1021/jz501077u

25. Li H., Wang L., Guan Y., Su Y., Mu J., Che H., Liu A. Guo Z. Facile solvothermal synthesis of $ZnCo_2O_4/MnO_2$ nanosheets composite with enhanced electrochemical properties as supercapacitor electrodes // Appl. Phys. A. – 2018. –Vol. 124. – Art. 485. https://doi.org/10.1007/s00339-018-1894-9

26. Minaj M.F., Satyajeet S.P., Pramod S.P., Appasaheb P.T. Unleashing the potential of binder-free hydrothermally synthesized marigold-like $ZnCo_2O_4$ for supercapacitors // Journal of Energy Storage. – 2023. – Vol. 74. – Art. 109490. https://doi.org/10.1016/j.est.2023.109490

27. Siyu W., Ning D., Dandan H., Ping W., Yupeng D., Pengcheng X., Yanwei S., Yen W. Synergistic effect of fluorine doping and oxygen vacancies on electrochemical performance of $ZnCo_2O_4$ for advanced supercapacitors and Zn-ion batteries // Acta Materialia. – 2023. – Vol. 257. – Art. 119190. https://doi.org/10.1016/j.actamat.2023.119190

28. Vignesh G., Ranjithkumar R., Devendran P., Nallamuthu N., Sudhahar S., Krishna Kumar M. Nitrogen doped reduced graphene oxide/$ZnCo_2O_4$ nanocomposite electrode for hybrid supercapacitor application // Materials Science and Engineering B. – 2023. – Vol. 290. – Art. 116328. https://doi.org/10.1016/j.mseb.2023.116328

29. Silambarasan M., Ramesh P.S., Geetha D., Ravikumar K., Elhosiny A.H., Algarni H., Soundhirarajan P., Chandekar K.V., Shkir M. A facile preparation of zinc cobaltite ($ZnCo_2O_4$) nanostructures for promising supercapacitor applications // J. Inorg. Organomet. Polym. – 2021. – Vol. 31. – Pp. 3905-3920. https://doi.org/10.1007/s10904-021-02077-z

30. Kedruk Y.Y., Contestabile A., Zeng J., Fontana M., Laurenti M., Gritsenko L.V., Cicero G., Pirri C.F., Abdullin K.A. Morphology effects on electro- and photo-catalytic properties of zinc oxide nanostructures // Nanomaterials. –2023. – Vol. 13. – Art. 2527. https://doi.org/10.3390/nano13182527

31. Tolubayeva D.B., Kedruk Y.Y., Gritsenko L.V. Influence of plasma and heat treatments on the properties of ZnO nanorods // Physical Sciences and Technology. – 2022. – Vol. 9, No. 3-4. – Pp.11-17. https://phst.kaznu.kz/index.php/journal/article/view/287/248

32. Tuan D.V., Ngan D. T.T., Thuy N.T., Lan H., Nguyet N.T., Thu V.V., Hung V.-P., Tam P.D. Effect of nanostructured MoS_2 morphology on the glucose sensing of electrochemical biosensors // Current Applied Physics. – 2020. – 20. – Pp. 1090-1096. https://doi.org/10.1016/j.cap.2020.06.027

33. Abdullin Kh.A., Cicero G., Gritsenko L.V., Kumekov S.E., Markhabaeva A.A. Effect of annealing and hydrogen plasma treatment on the luminescence and persistent photoconductivity of polycrystalline ZnO films // Journal of Applied Physics. – 2017. – 121. – Pp. 245303-1–245303-6. https://doi.org/10.1063/1.4989826

34. Mussabek G., Zhylkybayeva N., Baktygerey S., Yermukhamed D., Taurbayev Y., Sadykov G., Zaderko A.N., Lisnyak V.V. Preparation and characterization of hybrid nanopowder based on nanosilicon decorated with carbon nanostructures // Applied Nanoscience. – 2023. – Vol. 13. – P. 6709–6718. https://doi.org/10.1007/s13204-022-02681-6

35. Mussabek G., Zhylkybayeva N., Lysenko I., Lishchuk P.O., Baktygerey S., Yermukhamed D., Taurbayev Ye., Sadykov G., Zaderko A.N., Skryshevsky V.A., Lisnyak V.V., Lysenko V. Photo- and radiofrequency-induced heating of photoluminescent colloidal carbon dots // Nanomaterials. -2022. -Vol.12. – Art. 2426. https://doi.org/10.3390/nano12142426

36. Mussabek G., Baktygerey S., Taurbayev Ye., Yermukhamed D., Zhylkybayeva N., Zaderko A.N., Diyuk V. E. Afonin S., Yar-Mukhamedova G., Mariychuk R.T., Grishchenko L. M., Kanuchova M., Lisnyak V.V. Surface chemistry and catalytic activity in H_2O_2 decomposition of pyrolytically fluoralkynated activated carbons // RSC Advances. – 2024. – Vol.14. – Art. 29052. https://doi.org/10.1039/d4ra04883k

37. Paltusheva Zh.U., Kedruk Y.Y., Gritsenko L.V., Tulegenova M.A., Syritski V., Abdullin Kh.A. The influence of synthesis parameters and thermal treatment on the optical and structural properties of zinc oxide-based nanomaterials// Physical Sciences and Technology. – 2024. – Vol.11, No.1-2. – Pp. 49-57. https://doi.org/10.26577/phst2024v11i1a6

38. Dmitrieva E.A., Lebedev I.A., Grushevskaya E.A., Murzalinov D.O., Fedosimova A.I., Kemelbekova A.E., Kemelbekova A.E., Kazhiev, Zh. Sh., Zhaysanbayev, Zh. K., Temiraliyev A.T. The effect of deposition technique on formation of transparent conductive coatings of SnO_2 // Physical Sciences and Technology. – 2022. – 9. – Pp. 37-44. https://doi.org/10.26577/phst.2022.v9.i1.05

39. Markhabayeva A.A., Dupre R., Nemkayeva R., Nuraje N. Synthesis of hierarchical WO_3 microspheres for photoelectrochemical water splitting application // Physical Sciences and Technology. – 2023. – 10. – Pp. 33-39 https://doi.org/10.26577/phst.2023.v10.i2.04

40. Tolubayeva D.B., Gritsenko L.V., Kedruk Y.Y., Aitzhanov M.B., Nemkayeva R.R., Abdullin K.A. Effect of hydrogen plasma treatment on the sensitivity of ZnO based electrochemical non-enzymatic biosensor // Biosensors. – 2023. –13. – Art. 793. https://doi.org/10.3390/bios13080793

41. Dong X.C., Xu H., Wang X.W., Huang Y.X., Chan-Park M.B., Zhang H., Wang L.H., Huang W., Chen P. 3D graphene–cobalt oxide electrode for high-performance supercapacitor and enzymeless glucose detection // ACS Nano. – 2012. – Vol. 6. – Pp. 3206–3213. https://doi.org/10.1021/nn300097q

Information about authors:

Gritsenko Lesya Vladimirovna (corresponding author) – PhD, Professor at the Satbayev University (Almaty, Kazakhstan, e-mail: l.gritsenko@satbayev.university).

Kalkozova Zhanar Kanievna – Candidate of Physical and Mathematical Sciences, Associate Professor at the Al-Farabi Kazakh National University (Almaty, Kazakhstan, e-mail: zhanar.kalkozova@kaznu.edu.kz).

Kedruk Yevgeniya Yuryevna – PhD, Assistant Professor at the School of Natural and Social Sciences of the Kazakh-British Technical University (Almaty, Kazakhstan, e-mail: y.kedruk@kbtu.kz).

Paltusheva Zhaniya Urazgalievna – PhD, Senior Lecturer at the Satbayev University (Almaty, Kazakhstan, e-mail: zhaniya.paltusheva@gmail.com).

Mussakhanov Madi Nurzhanuly – student of the Kazakh-British Technical University (Almaty, Kazakhstan, e-mail: madimussakhanov@gmail.com).

Abdullin Khabibulla Abdullaevich – Doctor of Physical and Mathematical Sciences, Professor at the Al-Farabi Kazakh National University (Almaty, Kazakhstan, e-mail: kh.abdullin@physics.kz).

IRSTI 53.43.35 https://doi.org/10.26577/phst20251226

Prediction of the pitting corrosion rates in AISI 304 steel heat exchangers in industrial circulating waters

O.E. Narivs'kyi[1, 2], N.A. Solidor[1], T.V. Pulina[1*] and G.V. Snizhnoi[1]

[1]National University "Zaporizhzhya Polytechnic", Zaporizhzhya, Ukraine
[2]LCC "Ukrspetsmash", Berdyansk, Ukraine
*e-mail: pulinatv@ukr.net

(Received October 7, 2025; received in revised form November 27, 2025; accepted December 11, 2025)

A predictive methodology was developed to estimate the pitting growth rate on AISI 304 steel surfaces operating in industrial circulating waters. The approach is based on the observation that most pits formed near oxide inclusions are metastable and repassivate within minutes; therefore, corrosion losses of Cr, Ni, and Fe are attributed primarily to stable pits. Stable pits were identified using selective dissolution coefficients for chromium (ZCr) and nickel (ZNi). Second-order regression models were established to correlate corrosion losses (ΔCr, ΔNi, ΔFe) with steel composition, structural features, and water parameters such as chloride concentration and pH. Results show that ΔCr is mainly influenced by chloride content and microstructural factors, including the number of oxides (1.98–3.95 μm), average austenite grain size, and δ-ferrite volume. Factors reducing ΔFe losses follow the order: chloride concentration < Ni content < acidity < grain size < number of 1.98–3.95 μm oxides; whereas smaller oxides, inter-oxide spacing, and δ-ferrite promote higher losses. ΔNi primarily depends on structural heterogeneity rather than chemical composition or water parameters. The resulting model enables prediction of average pitting growth rates on AISI 304 steel in circulating waters with an accuracy of ±19%, providing a practical tool for assessing corrosion resistance in heat exchanger applications.

Keywords: pittings growth rate, model circulating waters, corrosion losses of metals in pittings.
PACS number(s): 81.65.Kn; 82.45.Bb.

1. Introduction

Nowadays, heat exchange equipment is widely used in various technological processes for the production of industrial products [1]. Therefore, many designs of heat exchangers have been developed by engineers and researchers, with different materials selected depending on the corrosive aggressiveness of the media. In practice, circulating waters containing chlorides and other anions are often used for cooling technological products. The heat exchange components of such equipment are made from stainless austenitic steels of the 18-10 type [2–4] and the alloy 06KhN28MDT (analogue to AISI 904L steel) [5, 6]. These materials are resistant to general corrosion in many media but can be susceptible to pitting corrosion in chloride-containing media, particularly in industrial circulating waters [7, 8]. It is generally known [9, 11] that passivated steels and alloys often undergo pitting in the presence of chlorides in the media. Therefore, the assessment and prediction of their resistance to pitting corrosion during equipment operation is a relevant issue. In low-mineralized solutions, such as industrial circulating waters, the resistance of stainless steels and alloys to pitting corrosion is evaluated based on their critical pitting temperatures [2–4, 12, 13]. This parameter characterizes the resistance of passive films on the surface of steels and alloys to pitting corrosion at a given chloride concentration and medium acidity. It is very convenient for practical use during the operation of heat exchangers, since by adjusting the flow rate of circulating water, it is possible to influence this parameter, provided that the chloride concentration increases or the acidity of the circulating water changes. Such an approach makes it possible to counteract pitting corrosion of steels during the operation of heat exchangers in recirculating water systems in the event of parameter changes. However,

this may contribute to a reduction in production efficiency, since their operating modes are altered. Therefore, during the operation of heat exchangers in industrial process lines at enterprises, even in the event of pitting corrosion caused by changes in recirculating water parameters, it is not possible to immediately change their operational regimes. Thus, a question arises in industrial practice: "How much time remains until perforation of heat exchange elements (plate, tube) of specified thickness (from 0.2 to 2.0 mm)?". To answer this question, a methodology has been developed for calculating the pitting growth rate on the surface of AISI 304 steel in model circulating waters. This methodology is based on previously established patterns and mechanisms of pitting corrosion of austenitic stainless steels and chromium-nickel-molybdenum alloys in chloride-containing media [2–8, 14], as well as on widely known information about the theory of localized corrosion [15–20].

2. Materials and methods

To develop a methodology for calculating the pitting corrosion growth rate on the surface of AISI 304 stainless steel exposed to model circulating waters with pH values ranging from 4 to 8 and chloride concentrations between 300 and 600 mg/L, mathematical models were constructed based on experimental data on corrosion losses of chromium (ΔCr), nickel (ΔNi), and iron (ΔFe) associated with pitting corrosion [21,22].

The developed mathematical models were based on second-order regression dependencies. In particular, the mathematical model (1) can be written in the form:

$$Y(\Delta Cr;\Delta Ni;\Delta Fe) = M_0 + \sum_{j=1}^{N} M_j \times x_j + \sum_{j=1}^{N} M_{(N+j)} \times x_j^2, \quad (1)$$

where: Y is the corrosion loss ΔCr, ΔNi or ΔFe of AISI 304 steel in pittings, mg for 240 hours of testing in model recycled water with pH 4-8 (x_1) and chloride concentration (x_2) of 300 and 600 mg/l [21, 22]. Here M is a mass coefficient of components x_j, and x_j is variables, in particular: x_3 – V_{ox}, vol. %; x_4 – the number of oxides up to 1.98 μm in size at 100 fields of view of an optical microscope (×320) in steel, pcs; x_5 – the number of oxides from 1.98 up to 3.95 μm in size, pcs; x_6 – L_{ox}, μm (mean distance between oxides in steel); x_7 – d_g, μm (mean grain diameter of austenite in steel); x_8 – volume of δ-ferrite vol. %; x_9 – C, wt. % (carbon content in steel); x_{10} – Mn; x_{11} – Si; x_{12} – Cr; x_{13} – Ni; x_{14} – N; x_{15} – Ti; x_{16} – S; x_{17} – P; x_{18} – χ_0, m^3/kg (specific magnetic susceptibility of steel). The chemical composition and structural constituents of the investigated AISI 304 steel heats were determined previously [23]. The specific paramagnetic susceptibility of austenite and the volume fraction of δ-ferrite were established in [24].

To build the second-order regressions (1), we used the analysis of the influence of individual factors $X = \{x_1, x_2, ..., x_{18}\}$ on the resultant (output – $Y = \{y_1, y_2, ..., y_7\}$ indicators [25, 26]. The dependent variables are: Y_1 = ΔCr, mg (10^{-5}) – chromium loss in pittings, Y_2 = ΔFe, mg (10^{-5}) – iron loss in pittings, Y_3 = ΔNi, mg (10^{-5}) – nickel loss in pittings,

$$Y_4 = \frac{Y_1}{Y_2} = Z_{Cr}, \quad (2)$$

where: Y_4 is the coefficient of selective dissolution of Cr in pittings,

$$Y_5 = (Y_4 \geq 1) = \left\{ 1/Y_4 \geq 1 \right\}, \quad (3)$$

- if $Z_{Cr} < 1$, then steel in a solution with such parameters (variables (x_1 (pH);) x_2 (C_{Cl^-}, mg/l)) undergoes pitting corrosion with the formation of stable pittings, otherwise, steel in a solution with such parameters (variables x_1, x_2) pits with the formation of metastable pittings [22].

The coefficient of selective nickel dissolution from pittings, Z_{Ni}, is determined according to equation (4):

$$Y_6 = \frac{Y_3}{Y_2} = Z_{Ni}, \quad (4)$$

$$Y_7 = (Y_6 \geq 1) = \left\{ 1/Y_6 \geq 1 \right\}. \quad (5)$$

If $Z_{Ni} < 1$, then the pittings are growing intensively, otherwise, the pittings are not growing intensively [22].

The developed mathematical models based on the second-order regressions $Y = \{y_1, y_2, \ldots, y_7\}$ were used to determine the corrosion losses ΔCr, ΔN, and and ΔFe in pittings, identify metastable and stable pittings, and the intensity of their growth. At the same

time, $Y_1 - Y_5$ were used to determine the rate of growth of stable pittings on the surface of AISI 304 steel in model recycled water with pH 4-8 and chloride concentration from 300 up to 600 mg/l, based on established approaches and analytical dependencies for determining the coefficients of participationof inclusions in pitting of steel [27].

The main approaches to calculating the average growth rate of pittings on the surface of AISI 304 steel are based on the fact that pittings nucleate and develop in the vicinity of inclusions [8, 28–30]. They are predominantly metastable and, therefore, repassivate within several minutes [31]. Consequently, it was assumed that all corrosion losses, ΔCr, ΔNi, and ΔFe, are concentrated only in stable pittings. These were identified using the coefficients of selective chromium dissolution from pittings (Z_{Cr}) [22]. It was also assumed that stable pittings form in the vicinity of inclusions located at the intersections with austenite grain boundaries in AISI 304 steel.

The quality of the developed methodology for calculating the growth rate of stable pittings on the surface of AISI 304 steel during pitting in model circulating waters with pH values from 4 up to 8 and chloride concentrations ranging from 300 up to 600 mg/l was evaluated using equation (6), based on the sum of squared instantaneous errors [32].

$$E = \sum_{S=1}^{S} \left(y^S - y^{S*} \right)^2, \qquad (6)$$

where: y^S is the actual depth of stable pittings measured with an MMP-2R optical microscope, μm; y^{S*} is the calculated depth of stable pittings on the surface of AISI 304 steel, μm.

The quality of each developed mathematical model (1–5) was evaluated based on the sum of squared errors (SSE) and the mean squared error (MSE) [32].

3. Results and discussion

To calculate the average growth rate of pittings on the surface of AISI 304 steel, it is proposed to use the calculated values of ΔCr, ΔNi, and ΔFe from pittings (1–5), depending on the parameters of the model circulating waters within the pH range of 4 up to 8 and chloride concentrations from 300 up to 600 mg/l.

In particular, for the mathematical model Y_1 (ΔCr) (1), based on data [21-24, 27, 33, 34], the regression coefficients were determined (Table 1).

Table 1 – Regression coefficients for Y_1.

M_2 (x_1)	$-499081 \cdot 10^{-6}$
M_9 (x_8)	$-1454{,}943182 \cdot 10^{-6}$
M_{20} (x^2)	$36285 \cdot 10^{-6}$
M_{21} (x_2^2)	$-1{,}52682 \cdot 10^{-6}$
M_{23} (x_4^2)	$-3{,}26616 \cdot 10^{-6}$
M_{24} (x_5^2)	$2771 \cdot 10^{-6}$
M_{25} (x_6^2)	$-1904 \cdot 10^{-6}$
M_{26} (x_7^2)	$12033 \cdot 10^{-6}$
M_{32} (x_{13}^2)	$329880 \cdot 10^{-6}$

According to the data (Table 1), it was established that chromium corrosion losses (ΔCr) from pitting of AISI 304 steel decrease with increasing alkalinity of model recirculating waters, δ-ferrite volume fraction, and average spacing between oxide inclusions. In particular, it was found that the ΔCr parameter of AISI 304 steel from pitting decreases by 20×10^{-6} mg with an increase in pH of model recirculating waters from 4 up to 8. It should be noted that the effect of δ-ferrite volume fraction in the investigated steel on its ΔCr from pitting was considerably less pronounced, as these values decreased by 0.00083×10^{-6} mg with an increase in its volume from 50×10^{-3} up to 168×10^{-3} vol. %. However, it can be stated that the size of oxide inclusions in AISI 304 steel has the greatest effect on its ΔCr from pitting. Indeed, these increase by 487.3×10^{-6} mg with an increase in average spacing between oxide inclusions from 150 up to 173 μm. From the analysis of regression coefficients M_{21} (x_2^2) and M_{23} (x_4^2), it follows that ΔCr of AISI 304 steel from pitting weakly depends on chloride concentration (x_2) in model recirculating waters and the quantity of fine oxides (x_4) therein. It was revealed that ΔCr of steel from pitting increases by 9797×10^{-5} mg with an increase in chloride concentration in model recirculating waters within the investigated range. In this case, the indicators of structural heterogeneity of AISI 304 steel have an effect that is more than an order of magnitude smaller on this parameter. Indeed, it was determined that ΔCr of AISI 304 steel from pitting increases by only 160×10^{-5} mg with

increasing quantity of oxides sized 1.98 … 3.95 μm within the investigated range and by 89×10^{-5} mg with an increase in average austenite grain diameter from 49 up to 86 μm. At the same time, it has been proven that the chemical composition of the investigated steel practically does not affect chromium corrosion losses in pitting within the investigated model recirculating waters.

Summarizing the foregoing, it can be noted that ΔCr of AISI 304 steel from pitting depends mainly on the media parameter (x_2) and its structural heterogeneity. Moreover, parameter (x_2) has 32.9 times stronger effect on ΔCr from pitting than x_5, x_7, x_8 taken together.

For the mathematical model Y_2 (ΔFe), based on data [21-24, 27, 33, 34], its coefficients were established (Table 2). From the analysis of data (Table 2), it can be noted that Y_2 decreases with increasing pH (x_1) of model recirculating waters, chloride concentration therein (x_2), quantity of oxides in steel sized from 1.98 up to 3.95 μm (x_5), mean austenite grain diameter (x_7), and nickel content therein.

Table 2 – Coefficients of mathematical model Y_2.

M_2 (x_1)	$-4765640\cdot10^{-6}$
M_9 (x_8)	$1536023300\cdot10^{-6}$
M_{20} (x_1^2)	$38068\cdot10^{-6}$
M_{21} (x_2^2)	$-2{,}37036\cdot10^{-6}$
M_{23} (x_4^2)	$83{,}3358\cdot10^{-6}$
M_{24} (x_5^2)	$-2800\cdot10^{-6}$
M_{25} (x_6^2)	$2420\cdot10^{-6}$
M_{26} (x_7^2)	$-12540\cdot10^{-6}$
M_{32} (x_{13}^2)	$-443110\cdot10^{-6}$

According to the analysis of Eq. (1) and data (Table 2), it has been established that ΔFe losses from pitting in steel decrease by 19.063×10^{-5} mg with an increase in pH (x_1) of the media from 4 up to 8, by 0.6367×10^{-5} mg with an increase in chloride concentration (x_2) within the range of 300–600 mg/l, by 155.4×10^{-5} mg with an increase in the quantity of oxides of the aforementioned size (x_5) in the steel, by 62.7×10^{-5} mg with an increase in the mean austenite grain diameter (x_7) from 49 up to 86 μm, and by 9.7×10^{-5} mg with an increase in nickel content (x_{13}) in the steel from 8.1 up to 9.3 wt. %. It should be noted that ΔFe of steel from pitting increases with increasing pH (x_1), volume of δ-ferrite inclusions (x_8), quantity of oxides sized up to 1.98 μm (x_4), and mean distance between oxides (x_6) (Table 2). Calculation of the effect of $X = \{x_1, x_4, x_6, x_8\}$ on ΔFe showed that ΔFe of AISI 304 steel from pitting increases by 18.2726×10^{-5} mg with increasing pH (x_1) of the media from 4 up to 8, by 7.5523×10^{-5} mg with increasing quantity of fine oxides (x_4) from 300 up to 425, by 18×10^{-5} mg with increasing mean distance between oxides (x_6) from 150 up to 173 μm, and by 152.4×10^{-5} mg with increasing volume of δ-ferrite inclusions (x_8) from 0.014 up to 0.113 vol. %.

Summarizing the effect of parameters $X = \{x_1, x_2, x_4, x_5, x_6, x_7, x_8, x_{13}\}$ on ΔFe of AISI 304 steel from pitting, it should be noted that the significance of factors causing a decrease in Y_2 increases in the following sequence: x_2, x_{13}, x_1, x_7, x_5, while those causing an increase in Y_2 are: x_4, x_6, x_1, x_8. Thus, it can be noted that the parameters of model recirculating waters – pH (x_1) and chloride content therein (x_2) – have weak effect on ΔFe of AISI 304 steel from pitting. However, the structural constituents of AISI 304 steel primarily determine corrosion losses ΔFe from pitting. These decrease with increasing quantity of oxides sized 1.98 up to 3.95 μm, mean austenite grain diameter, and increase if the mean distance between oxide inclusions and volume of δ-ferrite inclusions in steel increase. A hypothesis has been proposed that stable pittings nucleate and grow in the vicinity of large oxides at their intersection with austenite grain boundaries. Indeed [22], it has been established that the greater the quantity of large-sized oxides in whose vicinity pittings nucleate and grow, the lower the current density of anodic currents therein due to their redistribution among pittings and the lower the intensity of ΔFe dissolution. Obviously, the greater the mean distance between oxides, the larger they are. According to the data presented in reference [22], in the vicinity of larger inclusions, there are more structural defects in the steel, which accelerates selective dissolution of ΔFe.

It should be noted that ΔCr from pitting of AISI 304 steel depends more on the parameters of model recirculating waters (x_1, x_2) than on the constituents of its structure $X = \{x_3 \ldots x_8\}$, whereas ΔFe correlates predominantly with the elements of its structure $X = \{x_5, x_6, x_7, x_8\}$. Most likely, this is related to the more negative value of the standard electrode potential of Cr compared to Fe [31].

For mathematical model Y_3 (1), using data $Y = Y_3$ [24] and $X = \{x_1 \ldots x_{18}\}$ [26], regression coefficients for Y_3 were established (Table 3).

Table 3 – Coefficients of mathematical model Y_3.

M_2 (x_1)	$-3977620 \cdot 10^{-6}$
M_9 (x_8)	$-2367054950 \cdot 10^{-6}$
M_{20} (x_{12}^2)	$278768 \cdot 10^{-6}$
M_{21} (x_2^2)	$1{,}94385 \cdot 10^{-6}$
M_{23} (x_4^2)	$3{,}74289 \cdot 10^{-6}$
M_{24} (x_5^2)	$-3397620 \cdot 10^{-6}$
M_{25} (x_6^2)	$2980 \cdot 10^{-6}$
M_{27} (x_7^2)	$278770 \cdot 10^{-6}$
M_{32} (x_{13}^2)	$1{,}94385 \cdot 10^{-6}$

Analysis of Table 3 data demonstrates that Y_3 (ΔNi) decreases with increasing pH (x_1) of model recirculating waters, volume of δ-ferrite inclusions in AISI 304 steel (x_8), quantity of oxide inclusions sized 1.98–3.95 μm (x_5), and with decreasing chloride content in model recirculating waters (x_2), number of oxides sized up to 1.98 μm (x_4), mean distance between oxides (x_6), mean diameter of austenite grains (x_7), and Ni concentration (x_{13}). Assessment of the significance of parameters $X = \{x_1, x_2, x_4, x_5, x_6, x_7, x_{13}\}$ on Y_3 was performed using mathematical model (1), with utilization of data from Table 3 and results from references [22, 24]. It was established that Y_3 decreases by 13.59×10^{-5} mg upon increasing pH (x_1) of recirculating waters from 4 up to 8, by 26.01×10^{-5} mg upon increasing volume of δ-ferrite inclusions in steel from 0.050 up to 0.168 vol. %, by 1.88513×10^{-3} mg upon increasing the number of inclusions sized 1.98–3.95 μm from 46 up to 240 per 100 microscope fields of view (×320). At the same time, it was calculated that Y_3 increases by 8.92×10^{-5} mg upon increasing pH (x_1) from 4 up to 8, by 0.35×10^{-5} mg upon increasing chloride concentration (x_2) from 300 up to 600 mg/l, by 0.2×10^{-5} mg upon increasing the number of fine oxides sized up to 1.98 μm (x_4) from 300 up to 425, by 22.14×10^{-5} mg upon increasing mean distance between oxides (x_6) from 150 up to 173 μm, by 1.3924×10^{-3} mg upon increasing mean austenite grain diameter (x_7) from 49 up to 86 μm, and by 47.43×10^{-11} mg upon increasing Ni content in steel (x_{13}) from 8.09 to 9.34 wt. %.

Based on the analysis performed, the significance of parameters $X = \{x_1, x_5, x_8\}$ that contribute to the decrease in Y_3 upon their increase is arranged in the following order: x_1, x_8, x_5, whereas parameters that contribute to the increase in Y_3, $X = \{x_1, x_2, x_4, x_6, x_7, x_{13}\}$, are: x_{13}, x_4, x_7. This demonstrates that Y_3 in AISI 304 steel decreases upon increasing the number of large oxide inclusions sized 1.98–3.95 μm, in the vicinity of which stable pittings nucleate at their intersection with austenite grain boundaries, upon increasing volume of δ-ferrite inclusions, and upon decreasing the mean austenite grain diameter.

Summarizing the foregoing, it can be stated that corrosion losses ΔNi from pitting are determined predominantly by the structural heterogeneity of the steel and are practically independent of changes in its chemical composition within standard ranges and parameters of model recirculating waters that promote pittings formation.

To identify metastable and stable pittings on the surface of the investigated AISI 304 steel in model recirculating waters, mathematical model (2) was developed, whose regression coefficients are presented in Table 4.

Analysis of Table 4 data demonstrates that the selective dissolution coefficient of Cr from pitting decreases with increasing chloride concentration (x_2), quantity of oxide inclusions sized up to 1.98 μm (x_4), mean distance between them (x_6), volume of δ-ferrite inclusions in AISI 304 steel (x_7), and with decreasing quantity of oxides sized 1.98–3.95 μm (x_5) and Ni concentration therein. At the same time, it should be emphasized that the regression coefficients M_2 (x_1) and M_{20} of model (2) are 7.107 and –11.8736, respectively. Thus, the coefficient Z_{Cr} decreases with increasing pH (x_1) of model recirculating waters from 4 up to 8 by only 4.77.

Table 4 – Coefficients of mathematical model $Y_4 = Z_{Cr}$.

M_2 (x_1)	$7276907 \cdot 10^{-6}$
M_9 (x_8)	$-1020086466 \cdot 10^{-6}$
M_{20} (x_1^2)	$-593681 \cdot 10^{-6}$
M_{21} (x_2^2)	$-4{,}02701 \cdot 10^{-6}$
M_{23} (x_4^2)	$-6{,}66467 \cdot 10^{-6}$
M_{24} (x_5^2)	$1834 \cdot 10^{-6}$
M_{25} (x_6^2)	$-1790 \cdot 10^{-6}$
M_{26} (x_7^2)	$-8099 \cdot 10^{-6}$
M_{32} (x_{13}^2)	$280000 \cdot 10^{-6}$

Thus, pH (x_1) of the media has practically no effect on the coefficient Z_{Cr}. At the same time, based on the results of analysis of the effects of parameters $X = \{x_1, x_2, x_4, x_5, x_6, x_7, x_8, x_{13}\}$ on Y_4, it was

established that these decrease by 101; 19; 1.09; 6.04; 13.3; 40.45 upon increasing volume of δ-ferrite inclusions in steel (x_8), chloride concentration in model recirculating waters (x_2), quantity of oxide inclusions sized up to 1.98 μm (x_4), mean distance between oxides (x_6), and mean diameter of austenite grains (x_7) within the specified ranges indicated above. At the same time, Y_4 increases by 101.76 and 6.08 upon increasing in the steel the quantity of oxides sized 1.98–3.95 μm (x_5), and by 6.08 upon increasing the Ni content therein within the aforementioned ranges.

Based on the analysis performed, it can be stated that the coefficient Z_{Cr} decreases with increasing volume of δ-ferrite inclusions (x_8) in steel, mean diameter of austenite grains (x_7), and with decreasing quantity of oxide inclusions sized 1.98–3.95 μm, in the vicinity of which pittings nucleate at their intersection with austenite grain boundaries. Thus, the results of previous investigations and the hypothesis regarding the effect of volume of δ-ferrite inclusions in steel on selective dissolution of metals from stable pittings are confirmed. In this connection, it is important to note that the specific magnetic susceptibility of austenite (χ_{18}) has no effect on the process of selective metal dissolution in pittings.

To identify metastable and stable pittings on the surface of AISI 304 steel, using computer processing $Y_5 = (Y_4 \geq 1) = \{1/Y_4 \geq 1\}$ as a function of variables $X = \{x_1, x_2, ..., x_{18}\}$, a mathematical model was constructed that is based on formula (3) and data from references [21, 27, 35]. The calculated coefficients of this mathematical model are presented in Table 5.

The proposed mathematical model (3) (Table 5) provides the ability to very rapidly calculate Z_{Cr} and assess the nature of pittings on the surface of AISI 304 steel as a function of recirculating water parameters and steel properties.

Table 5 – The coefficients of mathematical model $Y_5 = (Y_4 \geq 1) = \{1/Z_{Cr} \geq 1\}$.

M_2 (x_1)	$1966477 \cdot 10^{-6}$
M_9 (x_8)	$293560606 \cdot 10^{-6}$
M_{20} (x_2^1)	$-159659 \cdot 10^{-6}$
M_{21} (x_2^2)	$-1{,}18519 \cdot 10^{-6}$
M_{23} (x_4^2)	$-93{,}15195 \cdot 10^{-6}$
M_{24} (x_5^2)	$-581 \cdot 10^{-6}$
M_{25} (x_6^2)	$269 \cdot 10^{-6}$
M_{26} (x_7^2)	$-2465 \cdot 10^{-6}$
M_{32} (x_{13}^2)	$-63424 \cdot 10^{-6}$

To determine the coefficient Z_{Ni} for selective dissolution of nickel from pitting, a mathematical model was constructed using formula (4), and the established coefficients of this model are presented in Table 6.

Table 6 – The coefficients of mathematical model $Y_6 = \frac{Y_3}{Y_2} = Z_{Ni}$.

M_2 (x_1)	$16792025 \cdot 10^{-6}$
M_9 (x_8)	$-14718238697 \cdot 10^{-6}$
M_{20} (x_2^1)	$-1374383 \cdot 10^{-6}$
M_{21} (x_2^2)	$-16{,}2513 \cdot 10^{-6}$
M_{23} (x_4^2)	$-246 \cdot 10^{-6}$
M_{24} (x_5^2)	$27576 \cdot 10^{-6}$
M_{25} (x_6^2)	$-20603 \cdot 10^{-6}$
M_{26} (x_7^2)	$120672 \cdot 10^{-6}$
M_{32} (x_{13}^2)	$3481913 \cdot 10^{-6}$

According to the data in Table 6, Y_6 (Z_{Ni}) decreases by 1471.82; 4.39; 22.29; 156.06 with increasing parameters $X = \{x_3, x_2, x_4, x_6\}$ within the ranges specified above. At the same time, Y_6 (Z_{Ni}) increases by 1530.02; 602.76; 8983 with increasing parameters $X = \{x_5, x_7, x_{13}\}$ within the ranges specified above.

Summarizing the foregoing, it can be noted that the coefficients Z_{Ni} depend predominantly on variables x_8, x_5, x_6, x_7, x_{13}. Moreover, their influence increases in the following sequence: x_{13}, x_6, x_7, x_8, x_5. At the same time, the effect of x_7, x_8, x_5 is most substantial; therefore, volume of δ-ferrite inclusions, mean austenite grain diameter, and quantity of large oxides have the greatest effect on the process of selective nickel dissolution from pitting.

A mathematical model (5) was constructed that enables assessment of the intensity of pittings propagation on the surface of AISI 304 steel in model recirculating waters. The coefficients of mathematical model (5) are presented in Table 7.

Summarizing the foregoing, it can be noted that by applying information technologies and mathematical model (5), it is possible to rapidly assess the intensity of pitting propagation on the surface of AISI 304 steel. At the same time, analysis of model (5) showed that the Z_{Ni} coefficients of AISI 304 steel decrease with increasing volume of δ-ferrite inclusions (x_8) and with decreasing mean austenite grain diameter (x_7) and quantity of oxides (1.98–3.95 μm) (x_5). The influence of parameters

$X = \{x_5, x_7, x_8\}$ on Z_{Ni} was found to be most significant, while the influence of parameters $X = \{x_1, x_2, x_4, x_6, x_{13}\}$ was found to be insignificant.

Table 7 – Coefficients of the mathematical model (5).

M_2 (x_1)	$1525000 \cdot 10^{-6}$
M_9 (x_8)	$-416666667 \cdot 10^{-6}$
M_{20} (x_1^2)	$-125000 \cdot 10^{-6}$
M_{21} (x^2_2)	$-5{,}92596 \cdot 10^{-7}$
M_{23} (x^2_4)	$-1{,}85183 \cdot 10^{-5}$
M_{24} (x^2_5)	$765 \cdot 10^{-6}$
M_{25} (x^2_6)	$-659 \cdot 10^{-6}$
M_{26} (x^2_7)	$3418 \cdot 10^{-6}$
M_{32} (x^2_{13})	$116313 \cdot 10^{-6}$

Analysis of the indicated models demonstrates that ΔCr from pitting depends primarily on chloride concentration in model recirculating waters and such steel parameters as oxide quantity, mean austenite grain diameter, and δ-ferrite content. A hypothesis has been proposed that pitting nucleation and propagation are caused by the intensity of chloride ion adsorption on structural imperfections of AISI 304 steel in the vicinity of these oxides at their intersection with austenite grain boundaries. It was established that ΔFe from pitting decreases with increasing oxide quantity in the steel (sized 1.98…3.95 μm), mean austenite grain diameter, and increases when δ-ferrite quantity and mean distance between steel oxides increase. It has been proven that ΔNi from pitting decreases with increasing oxide quantity in the steel (1.98…3.95 μm) and δ-ferrite content, and with decreasing mean austenite grain diameter. It was established that coefficients Z_{Cr} decrease with increasing δ-ferrite quantity in the steel, mean austenite grain diameter, and with decreasing oxide quantity (sized 1.98…3.95 μm). This may also contribute to the transition of metastable pittings to stable pittings. It was found that coefficients ΔNi decrease with increasing oxide and δ-ferrite quantity, and mean austenite grain diameter of the steel. At the same time, it was established that media pH, steel chemical composition within standard ranges, fine oxides, their volume, and specific paramagnetic susceptibility do not affect selective dissolution of ΔCr, ΔFe, and ΔNi from pitting on AISI 304 steel. The proposed models provide the ability to assess the pitting character of AISI 304 steel, calculate ΔCr, ΔFe, ΔNi from pitting and their propagation rates, which is important in heat exchanger operation.

Taking into account the approaches mentioned above and the constructed mathematical models (1–5), the determination of the average pittings growth rate on the surface of AISI 304 steel has been justified using formula (7):

$$v_p = \frac{h}{\tau}, \quad (7)$$

where: v_p is mean pittings growth rate, μm/h; h is mean pitting depth, μm; τ is a test time, hours (is a constant value equal to 240 hours).

The average pitting depth h is calculated using the next equation:

$$\overline{h} = R \Big/ N_{s.p.}. \quad (8)$$

where: R is the radius of the conditional layer of metal dissolved from the steel during the test, μm; $N_{s.p.}$ is the number of stable pittings on the steel surface.

The parameter R is proposed to be determined by relation:

$$R = \sqrt[3]{\frac{3V}{4\pi}}, \quad (9)$$

where V is a volume of metal dissolved in pittings, μm^3.

The volume of metal dissolved in pittings is determined by:

$$V = V_{Fe} + V_{Cr} + V_{Ni}, \quad (10)$$

where $V_{(Fe, Cr, Ni)}$ is a volume of Fe, Cr, Ni dissolved on the pittings surface of, μm^3.

The volume of metals dissolved from the pitting surface is determined by equation (11):

$$V_{(Cr,Ni,Fe)} = m_{(Fe,Ni,Fe)} \Big/ \rho_{(Cr,Ni,Fe)}, \quad (11)$$

where $m_{(Cr, Ni, Fe)}$ is the mass of Cr, Ni, Fe dissolved on the surface of the pittings, g; $\rho_{(Fe, Cr, Ni)}$ is the density of Fe, Cr, Ni, $g/\mu m^3$.

According to [36], with densities $\rho_{Fe} = 7.874 \cdot 10^{-12}$ $g/\mu m^3$, $\rho_{Cr} = 7.19 \cdot 10^{-12}$ $g/\mu m^3$, $\rho_{Ni} = 8.9 \cdot 10^{-12}$ $g/\mu m^3$, the values $m_{(Cr, Fe, Ni)}$ can be identified with ΔCr, ΔFe, and ΔNi of steel from stable pittings, the calculation of which is performed using mathematical model (1).

As shown above, formation of stable pittings on the surface of the investigated AISI 304 steel occurs predominantly in the vicinity of the largest oxide inclusions sized up to 4 μm at their intersection points with austenite grain boundaries. Around smaller oxides (up to 1.98 μm), metastable pittings predominantly nucleate, characterized by rapid repassivation. In connection with this, the coefficients of oxide participation in the pitting-forming process of AISI 304 steel were determined exclusively for stable pittings with size exceeding 5 μm [37]. It was previously established [22] that the coefficients of oxide inclusion participation in pitting of AISI 304 steel do not depend on variations in its chemical composition within standard ranges, but are determined by pH and chloride concentration in chloride-containing recirculating waters. Thus, the role of oxides in pitting formation of AISI 304 steel correlates with the pitting potential. Based on this, to calculate the coefficients of oxide participation in pitting of AISI 304 steel in model recirculating waters with pH 4–8 and chloride concentration 300–600 mg/l, the following relationships (12–16) are proposed:

$$K = 0{,}341 - 3{,}7 \cdot 10^{-4} C_{Cl^-}, \text{ at pH 8;} \quad (12)$$

$$K = 0{,}081 + 1{,}20 \cdot 10^{-4} C_{Cl^-}, \text{ at pH 7;} \quad (13)$$

$$K = 0{,}082 + 1{,}42 \cdot 10^{-4} C_{Cl^-}, \text{ at pH 6;} \quad (14)$$

$$K = 0{,}085 + 1{,}40 \cdot 10^{-4} C_{Cl^-}, \text{ at pH 5;} \quad (15)$$

$$K = 0{,}048 + 2{,}10 \cdot 10^{-4} C_{Cl^-}, \text{ at pH 4.} \quad (16)$$

Where C_{Cl^-} is a concentration of chloride ions in the model recirculating water.

Relationships (12–16) enable determination of the fraction of oxide inclusions in AISI 304 steel that participate in the pitting-forming process. Calculations are conducted on a defined metal area, namely on 100 fields of view of an optical microscope (×320). In this case, the total number of oxides on the surface of AISI 304 steel is determined by metallographic analysis method [38]. It should be noted that modern optical microscopes are equipped with software that allows more rapid and more accurate determination of the quantity and size of inclusions in steels and alloys.

In model recirculating waters with pH 4–8 and chloride concentration 300–600 mg/l, fine oxide inclusions (up to 1.98 μm) in AISI 304 steel participated in the pittings-forming process in the range of 8.53–11.68 % of their total number on the sample surfaces, whereas oxides sized 1.98–3.95 μm were involved in pitting in the amount of 3.1–5.76 % of their total quantity [39]. Simultaneously, pittings that form in the vicinity of fine oxides rapidly repassivate because their sizes do not exceed 2 μm [40-45]. As a result, the parameters ΔFe, ΔCr, ΔNi obtained from such pittings are not taken into account in the calculation of the volume (V) of metal dissolved from stable pittings (10).

It is important to note that on mean, 4.43 % of oxide inclusions sized 1.98–3.95 μm were involved in nucleation of stable pittings. Taking this into account, the number of stable pittings per area of 100 microscope fields of view (×320) is recommended to be calculated using formula (17):

$$N_{s,p} = 0{,}0443 \times K \times N_{ox}, \quad (17)$$

where K is the participation of oxides involved in pitting, determined by formulas (12-16); N_{ox} is the total amount of oxides on the surface of AISI 304 steel per 100 microscope fields of view (×320).

Based on the analysis performed, it can be stated that the application of formulas (1–17) enables calculation of the mean growth rate of stable pittings on the surface of AISI 304 steel in model recirculating waters with pH 4–8 and chloride content 300–600 mg/l. At the same time, it should be emphasized that the pitting propagation rates of stable pittings on the surface of AISI 304 steel in recirculating waters calculated in this manner are characterized by a mean error of up to ±19 %. This finds confirmation in the results of laboratory studies and practical experience in heat exchanger equipment operation. This is due to the stochastic nature of the processes of pitting nucleation, development, and repassivation. Despite this, the proposed methodology for calculating the pitting propagation rate on the surface of AISI 304 steel in model recirculating waters enables prediction of the time to achieve perforation of heat transfer elements of heat exchangers in the event of their pitting.

4. Conclusion

The main approaches for calculating the average growth rate of pittings on the surface of AISI 304 steel in model circulating waters with pH values ranging from 4 up to 8 and chloride concentrations between 300 and 600 mg/l have been developed.

These approaches are based on the assumption that pittings nucleating and growing in the vicinity of oxide inclusions are predominantly metastable and, therefore, repassivate within several minutes. Consequently, it was assumed that all corrosion losses, ΔCr, ΔNi, and ΔFe, are concentrated only in stable pittings. It was proposed to identify them using the coefficient of selective chromium dissolution (Z_{Cr}). Second-order regression-based mathematical models were developed to establish the relationships between the corrosion losses of Cr, Ni, and Fe from pittings, the coefficients Z_{Cr} and Z_{Ni}, and the steel's chemical composition, structural constituents, and circulating water parameters. A method for calculating the growth rate of pittings on the surface of AISI 304 steel during the operation of heat exchangers in circulating water systems was developed and implemented in production. This method is based on the calculated values of corrosion losses ΔCr, ΔNi, and ΔFe from pittings and on the participation coefficients of oxide inclusions in pitting corrosion, determined using empirical formulas. It was shown that the sum of squared instantaneous errors for the average pitting growth rate determined by calculation and measurement is E = 0.250718, and the mean error is ± 19 %.

References

1. A. M. Demin A.M., Gorchakova A. A., Naumenko A. P., Odinets A. I. Condition monitoring of heat-exchange equipment of the diesel fuel hydrotreatment processes // AIP Conference Proceedings. – 2019. – Vol. 2141 (1). https://doi.org/10.1063/1.5122145

2. Narivskyi O.E., Subbotin S.O., Pulina T.V., Leoshchenko S.O., Khoma M.S., Ratska N.B. Modeling of pitting of heat exchangers made of 18/10 type steel in circulating waters // Materials Science. – 2023. – Vol. 58(5). – Pp. 1-7. https://doi.org/10.1007/s11003-023-00725-y

3. Narivskyi O.E., Subbotin S.O., Pulina T.V., Leoshchenko S.O., Khoma M.S., Ratska N.B. Mechanism of pitting corrosion of austenitic steels of heat exchangers in circulating waters and its prediction // Materials Science. – 2024. – Vol. 59(5). – Pp. 275-282. http://dx.doi.org/10.1007/s11003-024-00773-y

4. Narivskyi O.E., Subbotin S.O., Pulina T.V. Corrosion behaviour of austenitic steels in chloride-containing media during the operation of plate-like heat exchangers // Physical Sciences and Technology. – 2023. – Vol. 10(3-4). – Pp. 48-56. https://doi.org/10.26577/phst.2023.v10.i2.06.

5. Dzhus A. V., Narivskyi O. E., Subbotin S. A., et. al. Influence of components of 06XH28МДТ alloy (analogue of AISI904L steel) and parameters of model chloride-containing recycled water of enterprises on its pitting resistance // Metallophysics and Advanced Technologies. – 2024. – Vol. 46 (4) – Pp. 371-383. https://doi.org/10.15407/mfint.46.04.0371.

6. Dzhus A. V., Narivskyi O. E., Snizhnoi G. V., Pulina T. V., & Snizhnoi V. L. The effect of the specific magnetic susceptibility of the 06KhN28MTD alloy (similar to AISI 904L steel) on Its corrosion behaviour in the circulating water of enterprises // Metallophysics and Advanced Technologies. – 2024. – Vol. 46. – Pp. 739-753. https://doi.org/10.15407/mfint.46.08.0739.

7. Narivskiy A., Yar-Mukhamedova G., Temirgalieyva E., Mukhtarova M., Yar-Mukhamedova Y. Corrosion losses of alloy O6KhN28MDT in chloride-containing commercial waters // International Multidisciplinary Scientific GeoConference Surveying Geology and Mining Ecology Management, SGEM. – 2016. – Vol. 1. – Pp. 63–70.

8. Narivs'kyi, O.E. Corrosion fracture of platelike heat exchangers // Mater Sci. – 2005. – Vol. 41. – Pp. 122–128. https://doi.org/10.1007/s11003-005-0140-8

9. Alonso C., Castellote M., Andrade C. Chloride threshold dependence of pitting potential of reinforcements // Electrochim. Acta. – 2002. – Vol. 47. – Pp. 3469–3481. https://doi.org/10.1016/S0013-4686(02)00283-9

10. Zhang Q., Wang, R., Kato, M., Nakasa, K. Observation by atomic force microscope of corrosion product during pitting corrosion on SUS 304 stainless steel // Scripta Materialla. – 2005. – Vol. 52(3). – Pp. 227–230

11. Fukutsuka T., Anzai F. Kaneda,M. Matsuo Y., Sugie Y., Fukaura K. Preparation of high nitrogen containing stainless steels by mechanical alloying method and their localized corrosion behaviour // J. Soc. Mat. Sci. – 2004. – Vol. 53. – Art. 1175. https://doi.org/10.2472/jsms.53.1175

12. Sakhnenko N.D, Kapustenko P.A, Ved M.V, Zhelavsky S.G. Study of the susceptibility of non-cutting steels to pitting corrosion in hot water supply systems (Izuchenie sklonnosti nerezaveyushchikh staley k pittingovoy korrozii v sistemakh goryachego vodosnabzheniya) // Zhurnal prikladnoy khimii. – 1998. – Vol. 1. – Pp. 80–83. (In Russian).

13. Sakhnenko N.D, Kapustenko P.A, Ved M.V, Zhelavsky S.G. Analysis of pitting resistance of non-cutting steels in hot water supply systems (Analiz pittingostoykosti nerezaveyushchikh staley v sistemakh goryachego vodosnabzheniya) // Zashchita metallov. – 1998. – Vol. 34(4). – Pp. 378–383. (In Russian).

14. Dzhus A., Subbotin S., Pulina T., Snizhnoi G. Modeling the resistance of plate-like heat exchangers made of 06khn28mdt alloy (analogous to AISI904l steel) to crevice corrosion in recycled water enterprises // Physical Sciences and Technology. – 2024. – Vol. 11(3-4). – Pp. 58–66. https://doi.org/10.26577/phst2024v11i2b07

15. Krawiec H., Vignal V., Heintz O., Oltra R. Influence of the dissolution of MnS inclusions under free corrosion and potentiostatic conditions on the composition of passive films and the electrochemical behavior of stainless steels // Electrochim. Acta. – 2006. – Vol. 510 – Pp. 3235–3243. https://doi.org/10.1016/j.electacta.2005.09.015

16. Suter T., Webb E. G., Böhni H. & Alkire R. C. Pit Initiation on Stainless Steels in 1 M NaCl with and without Mechanical Stress // Journal of The Electrochemical Society. – 2001. – Vol. 148(5). – Pp. 174-185. https://doi.org/10.1149/1.1360204

17. Park J. O., Matsch S. and Böhni H. Effects of temperature and chloride concentration on pit initiation and early pit growth of stainless steel // Journal of The Electrochemical Society. – 2002. – Vol. 149. – Pp. 34-39. https://iopscience.iop.org/article/10.1149/1.1430415/

18. Ha H. Y., Kwon H. Effects of Cr_2N on the pitting corrosion of high nitrogen stainless steels // Electrochimica Acta. – 2007. – Vol. 52. – Pp. 2175–2180. https://doi.org/10.1016/j.electacta.2006.08.034

19. Zhang Q., Wang R., Kato M., Nakasa K. Observation by atomic force microscope of corrosion product during pitting corrosion on SUS 304 stainless steel // Scripta Materialla. – 2005. – Vol. 52 (3). – P. 227–230.

20. Guo Y., Li M., Yang L., Liu G. Study on corrosion behavior and mechanism of Fe-Cr alloy in chloride-containing environments based on reactive molecular dynamics // Electrochimica Acta. – 2025. – Vol. 543. -Art. 147576. https://doi.org/10.1016/j.electacta.2025.147576.

21. Dzhus A., Snizhnoi G. Prediction the durability of heat exchangers made of 06KhN28MDT alloy (analogous to AISI904L steel) to crevice corrosion during their operation in recycled water. Physical Sciences and Technology. – 2023. – Vol. 10(3-4). – Pp. 57–67. https://doi.org/10.26577/phst.2023.v10.i2.07

22. Zellele D. M., Yar-Mukhamedova G. S., Rutkowska-Gorczyca M. A review on properties of electrodeposited nickel composite coatings: Ni-Al_2O_3, Ni-SiC, Ni-ZrO_2, Ni-TiO_2 and Ni-WC // Materials. – 2024. – Vol. 17(23). – Art. 5715. https://doi.org/10.3390/ma17235715

23. Greshta, V. Effect of copper in silver coatings on the corrosion behavior of NZ30K–0.1 wt.% Ag alloy in Ringer–Locke solution // Physical Sciences and Technology. – 2025. – Vol. 12(1-2). – P. 95–102. https://doi.org/10.26577/phst20251219

22. Davíðsdóttir S., Gunnarsson B. G., Kristjánsson K. B., Ledésert B. A., & Ólafsson D. I. Study of corrosion resistance properties of heat exchanger metals in two different geothermal environments // Geosciences. – 2021. – Vol. 11(12). – Art. 498. https://doi.org/10.3390/geosciences11120498

23. Chen, X., Liu, H., Sun, X., Zan, B., & Liang, M. Chloride corrosion behavior on heating pipeline made by AISI 304 and 316 in reclaimed water // RSC advances. – 2021. – Vol. 11(61). – Pp. 38765-38773. https://doi.org/10.1039/D1RA06695A

24. Shit G. Improvement of pitting corrosion resistance of AISI type SS 304L in chloride medium // Bulletin of Materials Science. – 2025. – Vol. 48(4). – Art. 116. https://doi.org/10.1007/s12034-025-03477-4

25. Farhat N. Optoelectronic neural networks and learning machines // IEEE Circuits and Devices Magazine. – 2003. – Vol. 5(5). – P. 32-41. https://doi.org/ 10.1109/101.34898

26. Nacedal J.and Wright S. Numeral Optimisation // Springer-Verlag. – 2006. – 664 p.

27. Klapper H. S., Menendez C., Jesse S. Pitting corrosion resistance influencing corrosion fatigue behavior of an austenitic stainless steel in chloride-containing environments // Corrosion. – 2020. – Vol. 76(4). – Pp. 398-410. https://doi.org/10.5006/3353

28. Schmuki P., Hildebrand H., Friedrich A., Virtanen S. The composition of the boundary region of MnS inclusions in stainless steel and its relevance in triggering pitting corrosion // Corrosion Science. – 2005. – Vol. 47. – Pp. 1239–1250. https://doi.org/10.1016/j.corsci.2004.05.023.

29. Webb E. G., Alkire R. C. Pit initiation at single sulfide inclusions in stainless steel // J. Electrochem. Soc. – 2002. – Vol. 149 (6). – P. 286–295. https://doi.org/10.1149/1.1474430

30. Williams D.E., Zhu Y.Y. Explanation for initiation of pitting corrosion of stainless steels at sulfide inclusions // Journal of The Electrochemical Society. – 2000. – Vol. 147(5). – Pp. 1763-1766. https://iopscience.iop.org/article/10.1149/1.1393431/meta.

31. Greshta V., Narivskyi O., Dzhus A., Vynar V., Yar-Mukhamedova G., Mukashev K., Beissen N., Mussabek G., Imanbayeva A., Zelele D., Atchibayev R., & Kemelzhanova A. Corrosion behaviour of magnesium alloys NZ30K and NZ30K alloyed with silver in the model solution of the osteosynthesis process // Eurasian Physical Technical Journal. – 2024. – Vol. 21(3(49). – Pp. 29–36. https://doi.org/10.31489/2024No3/29-36

32. Freedman D.A. Statistical models: Theory and practice // Cambridge University Press. – 2005. – 458 p.

33. Spiegelhalter D. The Art of Statistics: How to Learn from Data // Basic Books. – 2019. – 448 p. https://doi.org/10.5038/1936-4660.13.1.7

34. Bruce P., Andrew B. Practical statistics for data scientists: 50+ essential concepts using R and Python // O'Reilly Media. – 2020. – 318 p.

35. Montgomary D.C., Reck E.A., Vineng G.G. Applied Statistics and Probability for Engineers // Jonh Wiley and Sons. – 2012. – 672 p.

36. Zschunke, A. (Ed.). Reference materials in analytical chemistry: a guide for selection and use // Springer Science & Business Media. – 2000. – Vol. 40. https://doi.org/10.1007/978-3-642-56986-9

37. Ibrahim M. A., Abd El Rehim S. S., Hamza M. M. Corrosion behavior of some austenitic stainless steels in chloride environments // Materials Chemistry and Physics. – 2009. – Vol. 115(1). – Pp. 80-85. https://doi.org/10.1016/j.matchemphys.2008.11.016

38. Kazakov A., Zhitenev A., & Ryaboshuk S. Interpretation and classification of non-metallic inclusions // Materials Performance and Characterization. – 2016. – Vol. 5(5). – Pp. 535-543. https://doi.org/10.1520/MPC20160040

39. Ali M., Ul-Hamid A., Khan T., Bake A., Butt H., Bamidele O. E., & Saeed A. Corrosion-related failures in heat exchangers // Corrosion Reviews. – 2021. – Vol. 39(6). – Pp. 519-546. https://doi.org/10.1515/corrrev-2020-0073

40. Burstein G.T., Moloney J.J. Cyclic thermammetry // Electrochem. Commun. – 2004. – Vol. 6. – Pp. 1037–1041. https://doi.org/10.1016/j.elecom.2004.08.006

41. Abd El Meguid E.A., Mahmoud N.A., Abd El Rehim S.S. The effect of some sulphur compounds on the pitting corrosion of type 304 stainless steel // Mater. Chem. Phys. – 2000. – Vol. 63. – Pp. 67–74. https://doi.org/10.1016/S0254-0584(99)00206-0

42. Abd El Meguid E. A., Abd El Latif A.A. Critical pitting temperature for type 254 SMO stainless steel in chloride solutions // Corrosion Science. – 2007. – Vol. 49. – Pp. 263–275. https://doi.org/10.1016/j.corsci.2006.06.011

43. Nenastina T., Sakhnenko M., Oksak S., Yar-Mukhamedova G., Zellele D., Mussabek G., & Imanbayeva A. Study of Complexation Patterns in the System Ni^{2+}, MoO_4^{2-}, $P_2O_7^{4-}$, Cit^{3-} for the development of poly-ligand electrolytes (study of complexation patterns) // Eurasian Chemico-Technological Journal. – 2024. – Vol. 26(3). – Pp. 155–160. https://doi.org/10.18321/ectj1638

44. Yar-Mukhamedova G. S., Zellele D. M., Rutkowska-Gorczyca M., Makhambet I., Mussabek G., Atchibayev R., Kemelzhanova A. Advancements in coating methods and properties of titanium-based composite coatings: A review // ES Materials and Manufacturing. – 2025. – Vol. 28. – Art. 1569. http://dx.doi.org/10.30919/mm1569

45. Zhilkashinova A., Skakov M., Zhilkashinova A., Abilev, M., Prokhorenkova N. Features of structural-phase states of Co-Cr-Al-Y composite coatings after heat treatment // Physical Sciences and Technology. – 2022. – Vol. 9(1-2). – Pp. 45–54. https://doi.org/10.26577/phst.2022.v9.i1.06

Information about authors:

Oleksii Eduardovich Narivs'kyi – Doctor of Sciences (Physics and Mathematics), Professor at the National Technical University "Kharkiv Polytechnic Institute" (Kharkiv, Ukraine, e-mail: amz309@ukr.net).

Natalia Arkadiivna Solidor – Candidate of Sciences (Physics and Mathematics), Associate Professor at the National Technical University "Kharkiv Polytechnic Institute" (Kharkiv, Ukraine, e-mail: natalysolidor@gmail.com).

Tetyana Veniaminivna Pulina – Doctor of Sciences (Physics and Mathematics), Professor at the National Technical University "Kharkiv Polytechnic Institute" (Kharkiv, Ukraine, e-mail: pulinatv@ukr.net).

Gennadii Valentinovich Snizhnoi – Doctor of Sciences (Physics and Mathematics), Professor at National Technical University "Kharkiv Polytechnic Institute" (Kharkiv, Ukraine, e-mail: snow@zp.edu.ua).

IRSTI 29.19.27, 53.47.23 https://doi.org/10.26577/phst20251227

Study of thermoelectric properties of tungsten silicides

A.T. Mamadalimov[1], M.Sh. Isaev[2, 3*], S.R. Qodirov[4], N.K. Khakimova[1] and I.A. Mengliev[5]

[1]Institute of Semiconductor Physics and Microelectronics, Tashkent, Uzbekistan
[2]National University of Uzbekistan named after Mirzo Ulugbek, Tashkent, Uzbekistan
[3]Cyber University of Uzbekistan, Tashkent, Uzbekistan
[4]Urgench State University, Urgench, Uzbekistan
[5]Tashkent State University of Transport, Tashkent, Uzbekistan
*e-mail: isayevmahmud02@gmail.com

(Received September 22, 2025; received in revised form December 11, 2025; accepted December 15, 2025)

This work presents a comprehensive investigation of the temperature-dependent electrical and thermal transport properties of tungsten silicides, including mono-, di-, and higher-order phases. A comparative analysis of experimental data is performed with particular emphasis on electronic structure, charge-carrier characteristics, and phase-dependent transport behavior. The results indicate that di- and higher-order tungsten silicides exhibit semiconductor-like properties, with electrical resistivities in the range of 50–85 μΩ·cm at 300 K. Nuclear magnetic resonance spectroscopy was employed to examine the local electronic environment of tungsten atoms and their interaction with surrounding silicon nuclei, revealing structural imperfections such as defects, grain boundaries, and secondary-phase inclusions that influence charge transport. The temperature dependences of electrical conductivity, thermal conductivity, Seebeck coefficient, and thermoelectric quality factor were systematically studied over the temperature range of 300–800 K. The analysis demonstrates that higher-order tungsten silicides exhibit the most favorable thermoelectric characteristics among the investigated phases, highlighting their potential for use in high-temperature thermoelectric energy conversion and sensing applications, as well as their promise for further optimization through controlled doping strategies.

Keywords: tungsten silicide, diffusion, phase analytics, electrical conductivity, thermal conductivity, thermoEMF.
PACS number(s): 72.20.Pa, 72.15.Jf, 72.80.Ga.

1. Introduction

Tungsten silicides synthesized via diffusion doping of monocrystalline silicon are promising materials for applications in micro- and nanoelectronics as well as solar engineering, owing to their high thermal stability, excellent electrical conductivity, and strong resistance to oxidation [1–4]. Transition metal silicides, particularly those based on tungsten, constitute an important class of intermetallic compounds that are widely employed in silicon-based technologies due to their compatibility with standard fabrication processes, chemical stability, and favorable electronic properties.

Beyond their established use in electrical contacts and Schottky barrier structures, tungsten silicides have attracted increasing interest as potential thermoelectric materials. The performance of thermoelectric materials is commonly evaluated using the dimensionless figure of merit Q=ZT, which depends on the Seebeck coefficient α, electrical conductivity σ and thermal conductivity æ, and is expressed as:

$$Q = \frac{\alpha^2 \sigma T}{æ}. \quad (1)$$

A deep understanding of the thermoelectric behavior of tungsten silicides is essential for the development of miniaturized temperature sensors and solid-state energy conversion devices [5].

Among the wide range of thermoelectric materials investigated, transition metal silicides–particularly tungsten silicide phases such as WSi_2 and W_5Si_3 have garnered special attention. These materials offer several advantages, including high-temperature sta-

bility, resistance to oxidation, relatively low cost, and environmental compatibility compared with conventional thermoelectric compounds based on tellurium or lead [6–8].

Despite these advantages, the thermoelectric properties of tungsten silicides remain insufficiently explored. Improving their thermoelectric efficiency requires a detailed analysis of their electronic structure and thermal transport behavior, as well as an understanding of the influence of phase composition, microstructure, and doping. In this paper, we investigate the thermoelectric properties of various tungsten silicide phases to evaluate their potential for application in high-temperature thermoelectric energy converters [9–12].

Tungsten silicides are promising materials for high-temperature thermoelectric applications due to their unique combination of structural stability, electronic properties, and thermal characteristics. Despite numerous studies on individual properties of tungsten silicides, there remains a lack of comprehensive understanding of how their crystal structure, defect states, and electronic environment collectively influence their thermoelectric performance [13-15].

The aim of this study is a comprehensive investigation of the formation, structure, defect states, and electronic properties of mono-, di-, and higher-order tungsten silicides, as well as their thermoelectric characteristics, with the goal of identifying the phases most promising for high-temperature thermoelectric converters.

The novelty of this work lies in its integrated approach: we simultaneously investigate the formation, crystalline structure, microstructural defects, electronic conductivity, and thermoelectric properties of various tungsten silicides. By correlating structural features and electronic behavior with thermoelectric performance, this study provides a detailed understanding of the material's behavior and identifies the specific tungsten silicide phases most suitable for high-temperature thermoelectric devices.

This research therefore bridges the gap between fundamental materials characterization and applied thermoelectric performance, offering new insights into the design of advanced materials for high-temperature energy conversion.

2. Experimental

Tungsten silicides of different stoichiometries (WSi, WSi_2, and W_5Si_3) were synthesized by solid-state diffusion between high-purity tungsten and single-crystal silicon substrates. The samples were prepared in a horizontal diffusion furnace (SUOL-4 type). The diffusion process was carried out at temperatures between 1000 and 1200 °C for 40–45 hours, conditions chosen to ensure the formation of monosilicide, disilicide, and higher silicide phases, as observed in previous studies of tungsten–silicon phase interactions. After diffusion annealing, the samples were cooled to room temperature inside the furnace to minimize thermal stresses.

The phase composition and crystal structure of the synthesized silicides were investigated using X-ray diffraction (XRD) using Cu Kα radiation. Diffraction patterns were collected in the 2θ range of 20–80°. Lattice parameters for each phase were refined using the Rietveld method. The obtained structural characteristics were found to correlate directly with the differences in thermal and electronic transport properties discussed later, particularly the increased structural complexity of the W_5Si_3 phase, which contributes to enhanced phonon scattering and, consequently, reduced thermal conductivity.

To analyze the local chemical environment of silicon atoms within each phase, ^{29}Si Nuclear Magnetic Resonance (NMR) spectroscopy was performed. The spectra were recorded at room temperature using a standard solid-state NMR setup with magic-angle spinning (MAS). Distinct chemical shifts and line broadening were used to distinguish between silicon sites in WSi, WSi_2, and W_5Si_3. Broadened lines in the higher silicide phase indicated the presence of multiple non-equivalent silicon sites and structural defects, which later manifested in enhanced phonon scattering and reduced thermal conductivity.

Electrical conductivity (σ) was measured in the temperature range 300–800 K using the standard four-probe technique. Rectangular specimens were prepared from the reacted silicide layers, and platinum leads were attached using high-temperature silver paste. Temperature stability during measurements was maintained within ±1 K. The resulting temperature dependence of σ confirmed metallic behavior for WSi and semiconducting behavior for WSi_2 and W_5Si_3, in agreement with their respective electronic structures.

Thermal conductivity (κ) was determined using the laser flash analysis (LFA) method. The thermal diffusivity (æ) was measured directly, while thermal conductivity was calculated according to

$$k = æ \cdot \rho \cdot C_p \quad (2)$$

where ρ is the density (determined by Archimedes' method) and C_p is the heat capacity (measured using differential scanning calorimetry, DSC).

This technique enabled accurate measurement of the temperature dependence of κ for all phases, revealing the lowest thermal conductivity for W_5Si_3 due to its complex tetragonal structure and higher defect concentration.

The Seebeck coefficient (α) was measured simultaneously with electrical conductivity using a differential DC method. A temperature gradient of approximately 10–15 K was applied across the sample, and the resulting thermoelectric voltage was recorded. Measurements were repeated during heating from 300 to 800 K.

In solid-state NMR spectroscopy, chemical shift (δ) is a sensitive indicator of the electron density around the nucleus. A strongly negative δ value typically corresponds to high levels of shielding, characteristic of metallic systems. A broad spectral line indicates electron inhomogeneity, as well as the influence of shielding anisotropy. The structures of W_5Si_2 and W_5Si_3 belong to different types of intermetallic compounds, resulting in different environments for the silicon atoms. The study was conducted using a Varian Mercury VX-400 NMR system.

This approach captured the expected monotonic increase of α with temperature and showed the highest Seebeck coefficient in W_5Si_3, consistent with its semiconducting nature and enhanced density of states near the Fermi level.

3. Results and discussion

The electrical conductivity, thermal conductivity and coefficient of thermo-EMF were measured in the temperature range of 300-800 K using standard techniques.

Fig. 1 shows the temperature dependence of the electrical conductivity of mono-, di- and higher silicides of tungsten. A noticeable decrease in electrical conductivity is observed for all tungsten silicide phases in Fig. 1. This trend is consistent with the expected increase in phonon scattering at elevated temperatures, which reduces charge-carrier mobility and thus lowers the overall conductivity.

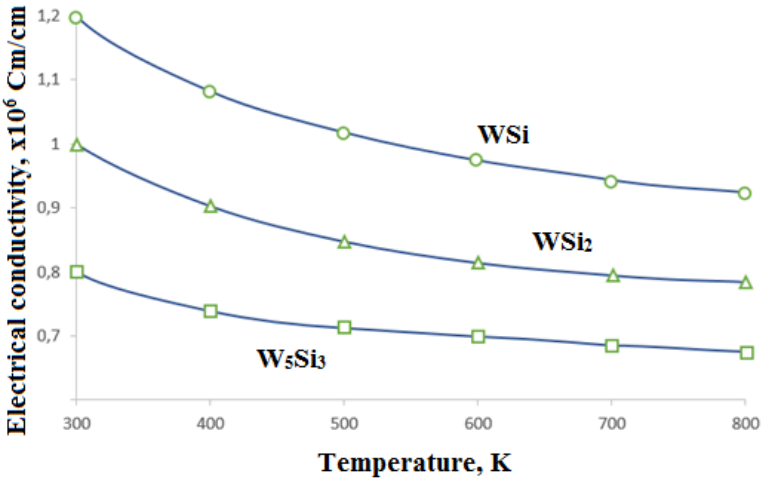

Figure 1 – Temperature dependences of electrical conductivity of various phases of tungsten silicides.

Tungsten monosilicide has the highest electrical conductivity, which is due to its metallic nature and dense crystal lattice [16]. The tungsten dilicide behaves as a semiconductor and takes an intermediate value between the electrical conductivity of the mono- and higher tungsten silicide. The highest tungsten silicide has a minimum electrical conductivity, characteristic of a more silicon phase with semiconductor properties [17,18].

Fig. 2 shows the temperature dependence of thermal conductivity of various phases of tungsten silicides. In all three phases, a decrease in thermal conductivity with an increase in temperature is observed due to increased phonon-phonon scattering [19].

Monosilicide has the highest thermal conductivity (æ = 80 W/m • K at T = 300 K) – a dense crystalline structure and high contribution of the electronic component. The smallest thermal conductivity (æ = 24 W/m • K at T = 300 K) is also observed in higher tungsten silicide.

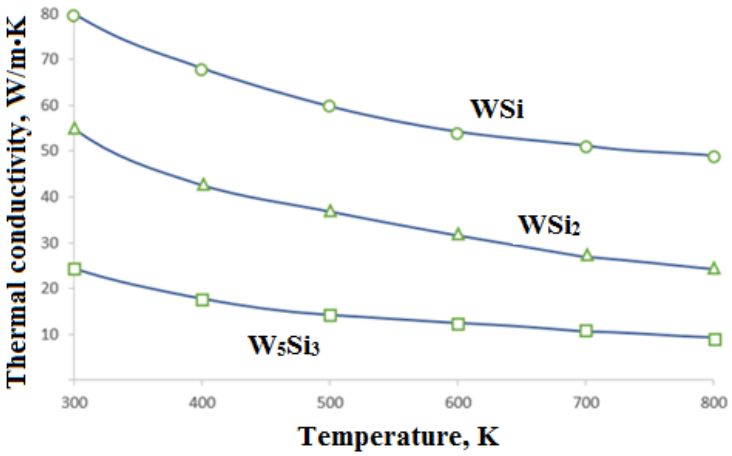

Figure 2 – Temperature dependences of thermal conductivity various phases of tungsten silicides.

The disilicide of the tungsten is æ = f (t) occupies an intermediate value (æ = 56 W/m • K at T = 300 K). Less thermal conductivity of the di- and higher tungsten silicide is due to their complex structure and an increase in scattering at the phonons, on grains boundaries and defects of the crystal lattice [20,21].

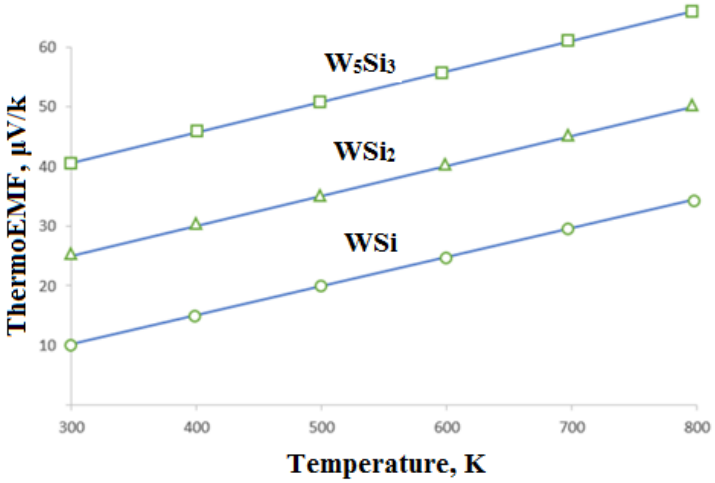

Figure 3 – Temperature dependences of the coefficient of thermoEMF of various phases of tungsten silicides.

Fig. 3 shows the temperature dependence of the coefficient of thermoEMF of various phases of tungsten silicides. With an increase in temperature, the thermoEMF coefficient increases, which is typical for semiconductors and metals with a high density of states at the level of Fermi. The highest silicide of tungsten α = 40 to 60 μV/k, which is associated with its more pronounced semicon-

ductor properties [22]. The tungsten dilicide has α = 25 μV/k (at T = 300 K) to 48 μV/k (at T = 800 K). Monosilicide demonstrates the smallest coefficient: α = 25 μV/k (at T = 300 K) up to 30 μV/k (at T = 800 K), which is characteristic of metal phases [23].

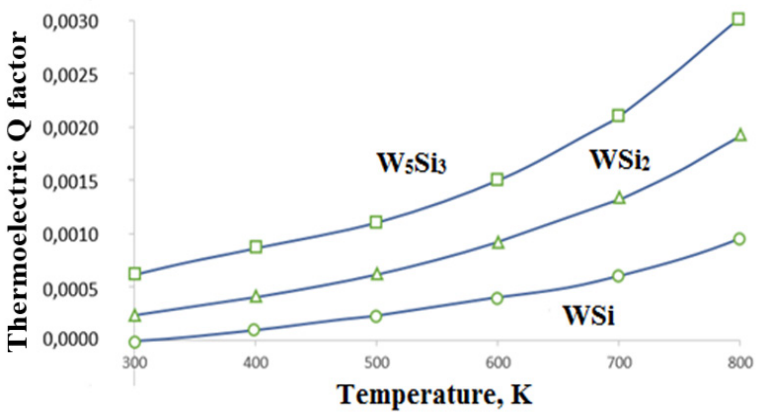

Figure 4 – Temperature dependencies of thermoelectric Q factor for various phases of tungsten silicides.

Fig. 4 shows the temperature dependence of thermoelectric Q factor Q = ZT. This parameter depends on the coefficient of thermoEMF, electrical conductivity and thermal conductivity. The maximum value of thermoelectric quality is observed in the highest silicide of the tungsten [24,25]. In this phase of tungsten silicides, despite the low electrical conductivity (Fig. 1), the high Seebeck coefficient (Fig. 3) and low thermal conductivity (Fig. 2) provides improved thermoelectric properties. The highest values of the Seebeck coefficient are observed in the highest silicide of the tungsten due to the fact that it increases the energy gap and density of states near the level of farm. This phase is a promising material for thermoelectric converters. The monosilicide of the tungsten shows the low values of Q-due to the low coefficient of thermoEMF and high thermal conductivity.

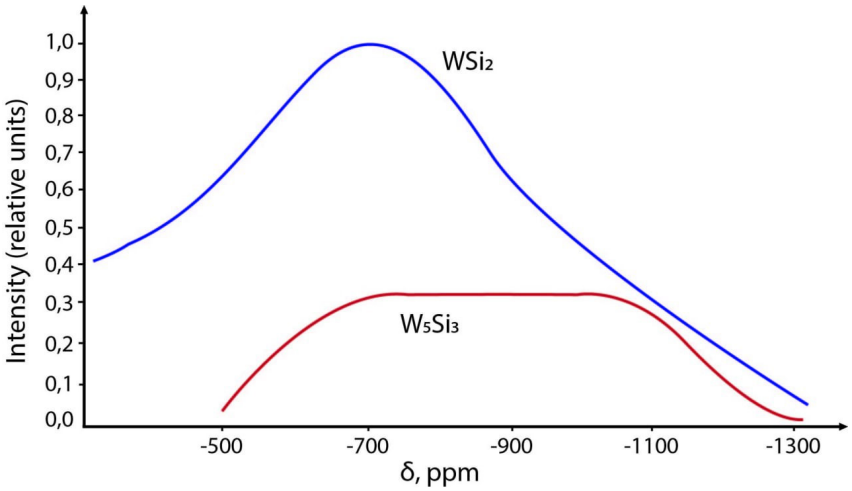

Figure 5 – NMR spectra of WSi_2 and W_5Si_2.

Fig.5 shows the relative signal intensity (Y-axis) as a function of the chemical shift δ (ppm, X-axis) for two tungsten silicides. The solid-state ^{29}Si NMR spectra clearly distinguish the silicon environments in the phases WSi_2 and W_5Si_3, allowing their structural and electronic features to be compared. The spectrum of WSi_2 exhibits a pronounced and relatively symmetric maximum in the region of –700 to –900 ppm, with high relative intensity. This indicates a narrow distribution of local electronic environments around silicon, consistent with a well-ordered crystal structure and the predominance of a single crystallographic Si site. The negative chemical shift is governed by a substantial Knight shift contribution, resulting from the high density of conduction electrons associated with tungsten.

In contrast, the spectrum of W_5Si_3 appears as a broad, asymmetric band extending toward –1100 to –1200 ppm, with substantially lower intensity. Such line broadening reflects the presence of multiple non-equivalent Si sites and a pronounced heterogeneity of local electronic states. The more negative chemical shift values indicate an enhanced metallic character of this phase, leading to a stronger Knight shift contribution. The overall broad signal width confirms a wide distribution of electron density on silicon atoms, which is characteristic of silicides with higher degrees of metal–metal interaction.

Thus, the comparative analysis of the spectra shows that WSi_2 possesses a more ordered structure with a narrower shielding distribution, while W_5Si_3 exhibits significant electronic and structural heterogeneity, resulting in substantial line broadening and a shift of the resonance toward more negative values.

Solid-state ^{29}Si NMR spectroscopy is a powerful tool for probing the local electronic environments in transition-metal silicides, where the chemical shift is strongly influenced by conduction-electron density, metal–metal bonding, and the number of crystallographically distinct Si sites. Previous systematic studies [26] have shown that ^{29}Si isotropic shifts in such compounds may span a remarkably wide range, from moderately negative values (−200 to −600 ppm) in weakly metallic silicides to highly negative shifts reaching −1000 ppm or more in phases with pronounced metallic behavior. This broad variation is primarily attributed to the Knight shift, which reflects the Fermi-contact interaction between the conduction electrons of the transition metal and the silicon nuclei. Consequently, heavy transition-metal silicides containing W, Mo, Re, or Ru typically exhibit the most negative shifts, along with significant line broadening.

The present NMR results align well with these established trends. The ^{29}Si spectrum of WSi_2 shows a relatively sharp and symmetric resonance centered between −700 and −900 ppm. Such a line shape is characteristic of phases with a well-ordered crystal structure and a single dominant Si site, resulting in a narrow distribution of local electronic environments. Comparable chemical-shift magnitudes have been reported for structurally ordered disilicides such as $MoSi_2$ and $RuSi_2$, which also exhibit moderate Knight-shift contributions while retaining a relatively uniform electronic environment.

In contrast, the spectrum of W_5Si_3 displays a broad, asymmetric resonance extending to much more negative values (approximately −1100 to −1200 ppm). This behavior is fully consistent with earlier observations for higher-order transition-metal silicides [27,28], where multiple non-equivalent Si sites, enhanced metallicity, and strong metal–metal interactions lead to a large Knight shift as well as substantial broadening of the spectral line. Such a broadened resonance typically reflects a wide distribution of conduction-electron density at the Si sites, arising from both intrinsic structural complexity and electronic heterogeneity. Furthermore, studies employing temperature-dependent ^{29}Si NMR [29] have demonstrated that highly metallic silicides often exhibit pronounced shift anisotropy and strong sensitivity to structural defects, grain boundaries, and site disorder–features also consistent with the line broadening observed in W_5Si_3.

The obtained results are consistent with the general understanding of charge and heat transport mechanisms in transition-metal silicides and agree well with previously published data [30-32]. The measured temperature dependence of electrical conductivity shows a monotonic decrease of σ with increasing temperature for all phases studied. This behavior is typical for materials in which phonon scattering dominates at elevated temperatures. Similar σ(T) trends were previously reported for $MoSi_2$, $TaSi_2$, and WSi_2 by [30], confirming the universal nature of phonon-limited transport in silicides with rigid crystal lattices.

The metallic behavior of monosilicide WSi can be attributed to the presence of dense d-bands near the Fermi level, which ensure high carrier mobility. According to earlier studies on monosilicides of transition metals (WSi, MoSi, TiSi), these phases typically exhibit very low Seebeck coefficients due to the predominant electronic contribution to conductivity [30,31]. Our results fully support these findings: the

Seebeck coefficient of WSi remains within 25–30 μV/K over the 300–800 K temperature range.

Tungsten disilicide WSi_2 shows behavior characteristic of a narrow-band semiconductor. The performed NMR analysis reveals a highly symmetric silicon environment and broader spectral lines compared to WSi, in agreement with literature data on partially ordered silicon sublattices in disilicides [31]. As previously noted by [31], semiconductor-like disilicides display an increase in the Seebeck coefficient with temperature. This trend is also observed here: α increases by nearly a factor of two between 300 and 800 K.

The most noteworthy behavior is observed in the higher tungsten silicide W_5Si_3. According to the results, this phase exhibits the lowest thermal conductivity and the highest Seebeck coefficient among the materials studied. A similar effect was reported by [32] for Nb- and Ta-doped W_5Si_3, where reduced thermal conductivity was attributed to the complexity of the crystal structure and enhanced phonon scattering at structural defects. Our NMR data, showing multiple nonequivalent silicon sites and broadened spectral lines, also indicate defect-rich local environments, which likely contribute to the observed suppression of lattice thermal conductivity.

A promising direction for further improvement of the thermoelectric performance of WSi_2 and W_5Si_3 is doping with transition metals such as Nb, Ta, or Re. Previous studies [32] have shown that doping enhances phonon scattering and can significantly increase ZT. The defect-related features revealed by our NMR measurements also suggest that controlled manipulation of structural disorder and point defects could serve as an effective tool for optimizing the thermoelectric properties of tungsten silicides.

4. Conclusion

In this study, the formation and properties of tungsten silicides were comprehensively investigated. Using X-ray diffraction, scanning electron microscopy, and nuclear magnetic resonance techniques, the formation of mono-, di-, and higher-order tungsten silicides was confirmed during diffusion annealing at temperatures ranging from 850 to 1000 °C. The study demonstrated the formation of intermetallic compounds, specifically identifying mono-, di-, and higher tungsten silicides, with their crystalline structures characterized and lattice parameters determined.

The electronic properties of these silicides were also examined. It was found that the di- and higher-order tungsten silicides exhibit semiconductor-type conductivity, with specific resistances measured at 50–85 μΩ·cm at 300 K. Nuclear magnetic resonance (NMR) spectra provided insights into the influence of the tungsten electronic environment on the silicon nucleus, revealing the presence of defects, grain boundaries, and inclusions. These structural imperfections were reflected in the spectral lines, contributing to the understanding of the material's microstructure.

Thermoelectric performance was evaluated through temperature-dependent measurements of electrical conductivity, thermal conductivity, the Seebeck coefficient, and thermodynamic volume in the range of 300–800 K. Among the tungsten silicides studied, the highest-order silicide exhibited the most favorable thermoelectric properties, indicating its potential as a promising candidate for high-temperature thermoelectric energy conversion applications. The WSi_2 phase exhibits a relatively narrow and symmetric resonance in the region of –700 to –900 ppm, indicating a more ordered silicon environment with a single dominant crystallographic site. In contrast, the spectrum of W_5Si_3 is significantly broader and shifted toward more negative chemical shift values (down to –1200 ppm), reflecting a higher degree of structural and electronic heterogeneity and multiple non-equivalent Si positions.

Overall, the results provide a detailed understanding of the structural, electronic, and thermoelectric characteristics of tungsten silicides, highlighting their suitability for advanced thermoelectric devices operating at elevated temperatures.

References

1. Utamuradova Sh.B., Rakhmanov D.A., Tuan P.L., Doroshkevich A.S., Isayev R.Sh., Abiyev A.S. Studying the influence of proton irradiation on the distribution profile of Pt and Cr in surface layers n-Si⟨Pt⟩, n-Si⟨Cr⟩ using ellipsometric spectroscopy // Advanced Physical Research. – 2024. – Vol. 6(2). – Pp. 83–89. https://doi.org/10.62476/apr62.83

2. Isaev M.Sh., Bozarov I.T., Tursunov A.I. Investigation of thermally stimulated conductivity of cobalt silicide // E3S Web of Conferences. – 2023. – Vol. 402. – Art. 14019. https://doi.org/10.1051/e3sconf/202340214019

3. Tursunov M.O., Iliev Kh.M., Ismaylov B.K. High-temperature analysis of silicon properties with manganese–oxygen binary complexes // Physical Sciences and Technology. – 2024. – Vol. 11(1–2). – Pp. 4–12. https://doi.org/10.26577/phst2024v11i1a1

4. Utamuradova Sh.B., Daliev Sh.Kh., Rakhmanov D.A., Samadov S.F., Doroshkevich A.S. Investigation of radiation defect formation of irradiated n-Si⟨Pt⟩ // Advanced Physical Research. – 2023. – Vol. 5(3). – Pp. 183–191.

5. Daliev K.S., Khusanov Z.M. Properties of single crystal silicon doped with vanadium // East European Journal of Physics. – 2024. – No. 1. – Pp. 366–369. https://doi.org/10.26565/2312-4334-2024-1-35

6. Daliev K.S., Utamuradova Sh.B., Khamdamov J.J., Bekmuratov M.B., Yusupov O.N., Norkulov Sh.B., Matchonov Kh.J. Defect formation in MIS structures based on silicon with an impurity of ytterbium // East European Journal of Physics. – 2024. – No. 4. – Pp. 301–304. https://doi.org/10.26565/2312-4334-2024-4-33

7. Kenzhaev Z.T., Iliev Kh.M., Ismailov K.A., Mavlonov G.Kh., Koveshnikov S.V., Ismaylov B.K., Isamov S.B. Physical mechanisms of gettering properties of nickel clusters in silicon solar cells // Physical Sciences and Technology. – 2024. – Vol. 11(1–2). – Pp. 13–22. https://doi.org/10.26577/phst2024v11i1a2

8. Utamuradova Sh.B., Rakhmanov D.A., Abiyev A.S. Influence of gamma rays on electrophysical properties of silicon doped with palladium atoms // Physics AUC. – 2024. – Vol. 34. – Pp. 198–203.

9. Azamatov Z.T., Yuldoshev M.A., Bazarbayev N.N., Bakhromov A.B. // Physics AUC. – 2023. – Vol. 33. – P. 139–145.

10. Utamuradova Sh.B., Rakhmanov D.A., Doroshkevich A.S., Genov I.G., Tuan P.L., Kirillov A. Processes of defect formation in silicon diffusionally doped with platinum and irradiated with protons // Eurasian Physical Technical Journal. – 2023. – Vol. 20(3). – Pp. 35–42. https://doi.org/10.31489/2023No3/35-42

11. Ayupov K.S., Zikrillaev H.F., Saitov E.B., Abdullaeva N.U., Umarkhojayeva Z.N., Yakhyayev M.M. Auto-oscillations of current in injection structures p^+–p(Si) based on heavily compensated silicon // Physical Sciences and Technology. – 2024. – Vol. 11(3–4). – Pp. 49–57. https://doi.org/10.26577/phst2024v11i2b06

12. Utamuradova Sh.B., Rakhmanov D.A., Abiyev A.S. Influence of different types of radiation on the crystal structure of silicon monocrystals n-Si // East European Journal of Physics. – 2024. – No. 2. – Pp. 380–383. https://doi.org/10.26565/2312-4334-2024-2-47

13. Abdullayev J.Sh., Sapaev I.B. Modeling and calibration of electrical features of p–n junctions based on Si and GaAs // Physical Sciences and Technology. – 2024. – Vol. 11(3–4). – Pp. 39–48. https://doi.org/10.26577/phst2024v11i2b05

14. Utamuradova Sh.B., Daliev Sh.Kh., Rakhmanov D.A., Khamidjanov I.Kh., Doroshkevich A.S., Mezentseva Zh.V., Tatarinova A. Influence of gamma rays on electrophysical properties of silicon doped with palladium atoms // Advanced Physical Research. – 2025. – Vol. 7(3). – Pp. 166–173. https://doi.org/10.62476/apr.73166

15. Ismaylov B.K., Zikrillayev N.F., Ismailov K.A., Kenzhaev Z.T. Clusters of impurity nickel atoms and their migration in the crystal lattice of silicon // Physical Sciences and Technology. – 2023. – Vol. 10(1–2). – Pp. 13–18. https://doi.org/10.26577/phst.2023.v10.i1.02a

16. Utamuradova Sh.B., Daliev Kh.S., Daliev Sh.Kh., Muzafarova S.A., Fayzullaev K.M., Muzafarova G.A. // E3S Web of Conferences. – 2024. – Vol. 583. – Art. 04006. https://doi.org/10.1051/e3sconf/202458304006

17. Nematov D., Kholmurodov Kh., Stanchik A., Fayzullaev K., Gnatovskaya V., Kudzoev T. On the optical properties of the $Cu_2ZnSn[S_1–xSe_x]_4$ system in the IR range // Trends in Sciences. – 2023. – Vol. 20(2). – Art. 4058. https://doi.org/10.48048/tis.2023.4058

18. Utamuradova Sh.B., Daliyev Sh.Kh., Khamdamov J.J., Matchonov Kh.J., Utemuratova Kh.Y. Research of the impact of silicon doping with holmium on its structure and properties using Raman scattering spectroscopy methods // East European Journal of Physics. – 2024. – No. 2. – Art. 274. https://doi.org/10.26565/2312-4334-2024-2-28

19. Mamadalimov A.T., Isaev M.Sh., Atamirzaev T.U., Ernazarov S.N., Karimov M.K. CVC structure of PtSi–Si⟨Pt⟩–M in a wide range of temperatures // East European Journal of Physics. – 2024. – No. 2. – Pp. 358–361. https://doi.org/10.26565/2312-4334-2024-2-43

20. Utamuradova Sh.B., Rakhmanov D.A., Tuan P.L., Doroshkevich A.S., Kinev V.A., Tatarinova A., Isayev R.Sh., Abiyev A.S. Influence of alpha particles on technological impurities in silicon doped with platinum // New Materials, Compounds and Applications. – 2025. – Vol. 9(1). – Pp. 50–57. https://doi.org/10.62476/nmca.9150

21. Dynys F.W., Sayir A., Mackey J., Sehirlioglu A. Thermoelectric properties of WSi_2–Si_xGe_{1-x} composites // Journal of Alloys and Compounds. – 2014. – Vol. 604. – Pp. 196–203. https://doi.org/10.1016/j.jallcom.2014.04.171

22. Rogacheva E. et al. Thermoelectric performance of silicides // Journal of Materials Science. – 2015.

23. Ohsumi S., Sato Y.J., Okazaki R. Transverse thermoelectric conversion in the mixed-dimensional semimetal WSi_2 // PRX Energy. – 2024. – Vol. 3. – Art. 043007. https://doi.org/10.1103/PRXEnergy.3.043007

24. Tao X., Jund P., Colinet C., Tedenac J. First-principles study of the structural, electronic and elastic properties of W_5Si_3 // Intermetallics. – 2010. – Vol. 18. – Pp. 688–693. https://doi.org/10.1016/j.intermet.2009.11.008

25. Isaev M.Sh., Khudayberdieva A.I., Mamatkulov M.N., Asatov U.T., Kodirov S.R. The surface layer morphology of Si⟨Cr⟩ samples // East European Journal of Physics. – 2024. – No. 4. – Pp. 297–300. https://doi.org/10.26565/2312-4334-2024-4-32

26. Benndorf C., Eckert H., Kösters J., Pöttgen R. Equiatomic transition metal (T) silicides TT′Si: systematics of ^{29}Si NMR Knight shifts // Zeitschrift für Naturforschung B. – 2024. – Vol. 79(12). – Pp. 583–594. https://doi.org/10.1515/znb-2024-0015

27. Benndorf C., Eckert H., Pöttgen R. ^{29}Si, ^{47}Ti, ^{49}Ti and ^{195}Pt solid-state MAS NMR spectroscopic investigations of ternary silicides TPtSi, germanides TPtGe (T = Ti, Zr, Hf) and stannide TiPtSn // Dalton Transactions. – 2016. – Vol. 45(19). – Pp. 8215–8223. https://doi.org/10.1039/C6DT00861E

28. Ponomarev I., Kroll P. ^{29}Si NMR chemical shifts in crystalline and amorphous silicon nitrides // Materials. – 2018. – Vol. 11. – Art. 1646. https://doi.org/10.3390/ma11091646

29. Stebbins J.F., Kelsey K.E. Anomalous resonances in ^{29}Si and ^{27}Al NMR spectra of pyrope ($[Mg,Fe]_3Al_2Si_3O_{12}$) garnets: effects of paramagnetic cations // Physical Chemistry Chemical Physics. – 2009. – Vol. 11. – Pp. 6906–6917. https://doi.org/10.1039/B904731J

30. Luković J. et al. Tungsten disilicide (WSi_2): synthesis, characterization and properties // Zeitschrift für Anorganische und Allgemeine Chemie. – 2017. – Vol. 643. – Pp. 329–337. https://doi.org/10.1002/zaac.201700329

31. Stoetzel J. et al. Microstructure and thermoelectric properties of Si–WSi_2 nanocomposites // Journal of Applied Physics. – 2017. – Vol. 121. – Art. 095101. https://doi.org/10.1063/1.4976836

32. Zhang S., Buchta R., Östling M. A study of silicide formation from LPCVD-tungsten films: film texture and growth kinetics // Journal of Materials Research. – 2001. – Vol. 16. – P. 88–96. https://doi.org/10.1557/JMR.2001.88

Information about authors:

Abduqodir T. Mamadalimov – Doctor of Physical and Mathematical Sciences, Academician, Head of the "Radiation Physics of Solids" Laboratory at the Institute of Semiconductor Physics and Microelectronics, National University of Uzbekistan named after Mirzo Ulugbek (Tashkent, Uzbekistan, e-mail: mamadalimov.edu@mail.ruMakhmudhodzha).

Makhmud Sh. Isaev – Doctor of Physical and Mathematical Sciences, Professor at the Department of Physics of National University of Uzbekistan named after Mirzo Ulugbek (Tashkent, Uzbekistan, e-mail: isayevmahmud02@gmail.com).

Sardor R. Kodirov – Lecturer at the Department of Interfaculty General Technical Sciences, Urgench State University (Urgench, Uzbekistan, e-mail: qodirov.sardor@urdu.uz).

Nilufar K. Khakimova – PhD, Senior Researcher at "Radiation Physics of Solids" Laboratory of the Institute of Semiconductor Physics and Microelectronics, National University of Uzbekistan named after Mirzo Ulugbek (Tashkent, Uzbekistan, e-mail: Khakimova_nilufar@mail.ru).

Ismoil A. Mengliev – PhD, Associate Professor at the Department of Applied Mechanics, Tashkent State University of Transport (Tashkent, Uzbekistan, e-mail: ismoilmengliyev399313@gmail.com).

IRSTI 29.03.77 https://doi.org/10.26577/phst20251228

^{3}He neutron detector with Android smartphone integration

A.S. Kussainov[1, 2*], P. Arnqvist[3], N.P. Arnqvist[3],
N.O. Saduyev[1, 2], O. Kalikulov[1, 2], N. Yerezhep[1, 2],
A. Baktoraz[1, 2] and S. Utey[1, 2]

[1]Department of Physics and Technology, Al-Farabi Kazakh National University, Almaty, Kazakhstan
[2]Institute of Nuclear Physics, Almaty, Kazakhstan
[3]Department of Mathematics and Mathematical Statistics, Umeå University, Umeå, Sweden
*e-mail: arman.kussainov@gmail.com

(Received September 22, 2025; received in revised form November 14, 2025; accepted December 5, 2025)

We have developed a homemade neutron flux detection module with ^{3}He tube hot-swap capability and control-rich Android software interface. Real-time data analysis is done by a smartphone with Android application interfaced with the detector via a USB cable. This setup can be used as a neutron and gamma ray background detector or as a compact, mobile ^{3}He tubes calibration tool making it a cheap and easy-to-use alternative for the stationary setups. A fast neutron detection algorithm was implemented as a set of Java scripts and tested for real-time signal analysis. The modular structure of the device allows easy deployment and customization with further software development and regular upgrades. The current prototype was tested at the Nuclear Physics Research Institute under different neutron flux intensity conditions from the VVR-K water-cooled research reactor. Its simplicity and significantly lower cost, compared with conventional detector equipment, make it valuable for easy repetitive tasks with medium requirements for precision and neutron flux intensities.

Keywords: ^{3}He detector, proportional counter, android application, functional clustering, neutron capture, USB interface.
PACS numbers: 07.77.−n, 07.05.Hd, 02.70.−c.

1. Introduction

Personal Android devices provide adequate computational power, availability [1], and comfort of use over stationary computers, contributing to the increasing number of their applications in daily use and in fundamental physics experiments. Fast and reliable interaction between the measurement tool and processing module is important [2]. Android devices could use their own internal sensors, like accelerometers, Hall and infrared sensors, etc, or work with an external hardware coupled through different interfaces to detect fast transient phenomena of varying nature [3].

There are studies reporting the onboard hardware such as smartphone CMOS camera [4] used for particles detection. In more complex cases, to facilitate the efficient interaction of the Android devices together with registration and detection hardware, they are coupled with the separate detectors and/or electronic assemblies through the wireless **[5]** interface or USB cable. Sometimes, the measurements are done at some remote facility equipped with server capability providing the user with internet access with static or dynamically updated records and measurement data. The typical example for the last one is the global cosmic ray neutron monitor networks supported by various institutions worldwide, see, for example, the range of neutron monitor stations maintained by the University of Delaware Bartol Research Institute [6].

With the particular hardware and experimental problem in mind, the individual solution is usually implemented within this range of choices. Although some components and modules, such as registration devices, signal amplifiers, ADCs, USB or wireless interfaces, etc, remain the same, the custom software finalizes them into a single measurement tool to complete the desired experiment objective.

Neutron physics was and still remains the import part of modern tool of fundamental research as well as a practical tool in material studies [7]. Nuclear and

ionizing radiation detectors provide vital information about the environment and transient process around [8], We employed the modular neutron/gamma ray detection setup, provided by the Cosmic Rays Physics Laboratory [6] at the Nuclear Physics Institute, Almaty, Kazakhstan. In this setup, the detector is equipped with an electronic hardware interface consisting of an amplifier, an ADC, and a USB 2.0 bus for data exchange between the electronics and Android devices (smartphone). The smartphone is used for data storage and processing. The ADC generates digital output for every neutron and neutron-like, usually gamma ray, detection event in a proportional ^{3}He-filled SNC-18 (Slow Neutron Counter) detector tube; see Figure 1. These SNC-18 tubes are widely used in different stationary and mobile setups and can be found in old and new conditions in stock. High detection efficiency and low background noise are the benefits of using these Helium-3 detectors. ^{3}He interaction with neutron flux is the separate part of the contemporary nuclear physics research [9].

In our case, the ADC is designed to sample the signal output from the detector amplifier at the rate of 5000 times per second [10]. The detector module's electronics receive the high-voltage power from any connected Android device configured in the USB host mode. The USB host mode [11] had been conveniently added to Android devices version 3.1 and higher.

As a further development, we completed the provided setup with custom Android software for data flow registration, processing, and storage. The set of Java scripts is used for the USB bus signal HEX to decimal conversion, basic shape recognition routines and events counting as well as for the processed data formatting and subsequent storage. Additional work has been done for developing R scripts [12] for retrospective signal patterns classification and filtering.

The assembled device, with the ^{3}He detector tube attached to the electronics housing, and the smartphone, has a relatively compact and portable dimension of less than 50 cm; see Figure 2.

Figure 1 – SNC18 Slow neutron counter tube.

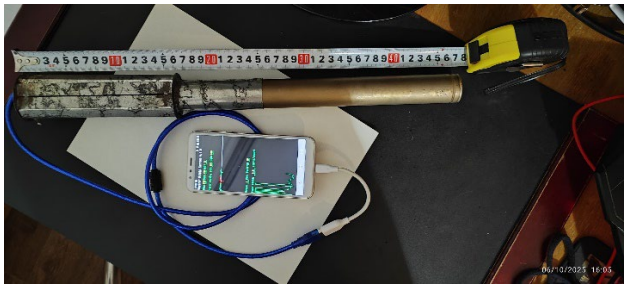

Figure 2 – Assembled experimental setup running the data acquisition.

As a result of this project, a low-cost and simple neutron flux detection device is implemented. The open source software with algorithms for specific signal shapes' detection and recognition and the clean and efficient interface for user communication and measurement control are developed. Consistent measurement data were collected under different conditions. The future work for detection algorithms and device versatility improvements is outlined.

2. Materials and methods

2.1 Signal shapes and events counting

Figure 3 (a)-(b) shows the typical shapes that could be seen in the amplifier-generated signal, digitized by the ADC. It is sent further down the USB cable to a smartphone as the raw hexadecimal data sequence and ultimately received and converted by the software to the decimal representation. If not hidden by the noise and other unclassified events, the meaningful data event contains the well-noticeable voltage drop from about 500 a.u. value baseline, see Figure 3 (a). This drop is caused by the two heavy ions, triton and proton, from the reaction of neutron capture, see Eq. 1, producing the fast ionization of the detector gas

$$^3He + n \rightarrow {}^3H + p + 0.754MeV \quad (1)$$

Thus, the energy of the reaction goes to the kinetic energies of the proton and triton ions moving in the opposite direction and leaving a heavy trail of ion pairs. Their drift to the anode and cathode results in the following transient electric current in the detector's circuitry [13]. Unlike a single electron event produced by gamma-ray Compton scattering or photo-effect, the amplitude of a signal from a neutron capture is well above the noise level. The difference in amplitudes of gamma ray and neutron detection events is regularly used to discriminate between them in counting. Under a better resolution, for this shape, one could potentially see the two overlapping peaks from ^{3}H and p ions [14]. We observe similar patterns, see Figure 3(b), but ours are primarily from the overlapping of two separate events, like the simultaneous detection of two neutrons or one neutron and one gamma quantum.

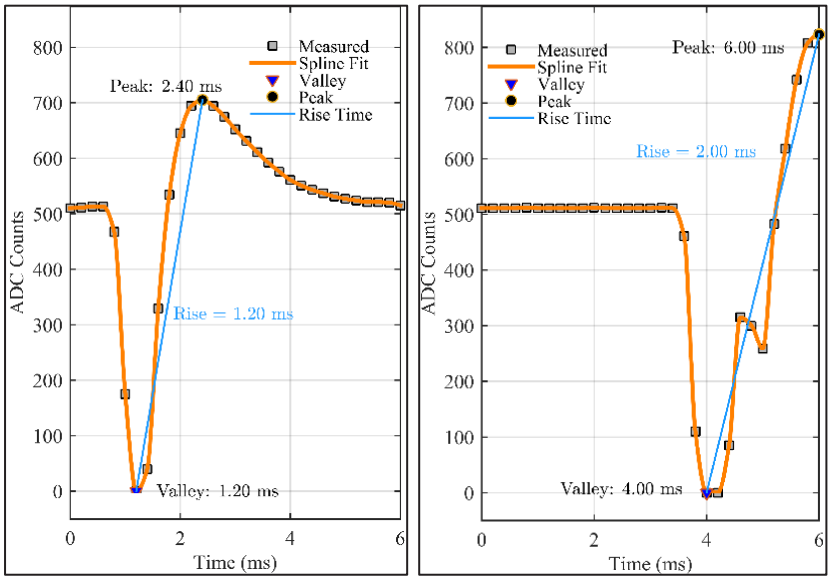

(a) (b)

Figure 3 – (a) Typical signal shapes recorded from a neutron detection event in a ^{3}He proportional counter. (b) Matlab generated plot for the data piece on the left with a 5-point moving average of 50 seconds.

The sampling frequency of our ADC is just not high enough to see the triton and proton events separately. Thus, depending on the event's location around the detector's physical volume and the detector's state after the previous event discharge, multiple events' shapes overlap and vary drastically in amplitudes, duration, and scaling factor.

Next, after the signal drop down almost to the zero level, the preamp shapes the electronics' response for the free charge surge dissipation, leading to the equally fast signal recovery with slight overshoot above the baseline. Subsequent return to the equilibrium is caused by the ion/electron drift and recombination processes being mediated by electronics and exhibited in the signal shape as an exponential decay.

The X axis on the Figure 3 (a)-(b) is spanned by the value of the buffer size supported by the hardware and software drivers. Documented by the software driver's manual and correlated with the transmission rate and other parameters, the buffer size, set in the app by default, is 62 of the 8-byte words. The buffer is arranged as 31 couples of hexadecimal values. That is the ADC splits the three-digit voltage value into a pair of 8-byte words. Backwards concatenation of these two parts in a single 3-digit value is implemented in our app.

The ADC's 5000 sec^{-1} fixed rate for the voltage sampling makes this buffer size equal to the 6.2 $msec$ period. Rather crude estimate for the count speed of the events of comparable amplitude, even without referring to the Raleigh criterion, gives us about 6 events per buffer size, or per 6.2 $msec$, that is about 1000 counts per second. This value is greatly reduced by the gas-filled detector tube recovery times and multiple other issues.

To provide the stand-alone detector setup with a data analysis module and implement the counting procedure, we have developed an Android application to process and record the data HEX sequence from the detector in real time. The free public drivers' library [15] was used to read the HEX data flow. Running on Android 3.1 version of the operating system and newer, it provides a communication interface with Arduinos and other USB serial hardware on Android. An extended list of the features provided for supported FTDI chip (our setup is using the one) devices includes open, close, setParameters, read and write, as well as many other flow control features.

Thus, the three parts of the waveform of interest are given by a) a sudden drop in a signal level below the baseline, followed by b) its rather speedy recovery above the average baseline level, usually half as high as the signal drop, completed by c) exponential-like decay.

We chose the event detection criteria based on the most prominent sudden drop below the noise level, corresponding to the transient current in the detector scheme. As soon as the data comes from a single 6.2 $msec$ buffer, the app searches through the voltage values sequence and finds the first available local minimum in the data. Further on it tests the presence of the fast recovery while staying well below the nose level. If all selected conditions and flags are satisfied, the event is classified as a neutron hit. As has been told, the neutron and gamma-ray pulse shapes have rather similar forms, though a definite distinction could be made depending on detector type, energy and other major parameters of the particle, see for example [16].

2.2. Graphical user interface

The app's user interface, as seen in Figure 4, provides the following sequence of interactive windows, saving and storage options, and text output.

The first screenshot, see Figure 4 (a), is activated as soon as the supported device with an FTDI chip is plugged in. This functionality is provided by the original driver's package. The minor alterations to the interface were made to suit our needs and to remove redundant, unsupported communications buttons and graphical interfaces.

As soon as the user presses the button with the detected communication chip, the main screen with measurement, display tools and buttons becomes available, see Figure 4(b). Data acquisition starts immediately as soon as the proper voltage levels applied to the gas tube etc.

Figure 4(b) shows the two main parts of the graphical interface. The top subwindow displays the captured signal shapes colored in green and red intermittently and plotted one by one in the order of detection. This was done to show that these are the different captured buffers selected from a data stream with the neutron detection event and they do not necessarily follow each other. The buffers with data pieces containing noise and signal, which do not meet the selection criteria, are discarded and are not displayed.

The bottom part of the graphical data display is the current count speed. The size of the time window is default 2 minutes but could be changed anytime by a user in interface. All the data fields above are interactive and, if changed, they affect the scale of the signal, the shapes' visibility, and the detection sensitivity of the algorithm. Besides, any part of the dynamically updated graphical interface could be turned off to help to free CPU and GPU load.

The next screenshot, see Figure 4 (c)-(d), shows the system's data storage default path and file's name containing unique time series identifier and timestamp. The last one, see Figure 4 (d), is the selected buffers data saved in decimal form as a text file. Alternatively, as seen in Figure 5(a)-(b), one can opt for the count speed vs. time output. This type of the data is vital in pulse shape and time series analysis [17]. At the present stage of development, it is hardcoded in order to avoid overcrowded user graphical interface.

The conversion of hex to decimal data is built around internal Java functions. As mentioned, by original design, the three-digit number corresponding to the signal level is split by ADC into two parts and sent to the Android device, one part after another, in a single buffer of 32 numbers. Upon receiving, the two parts of a single data point are concatenated together, see *HexDump* part of the package, and sent for a further processing, that is the pattern search, see the event detection criteria discussed above.

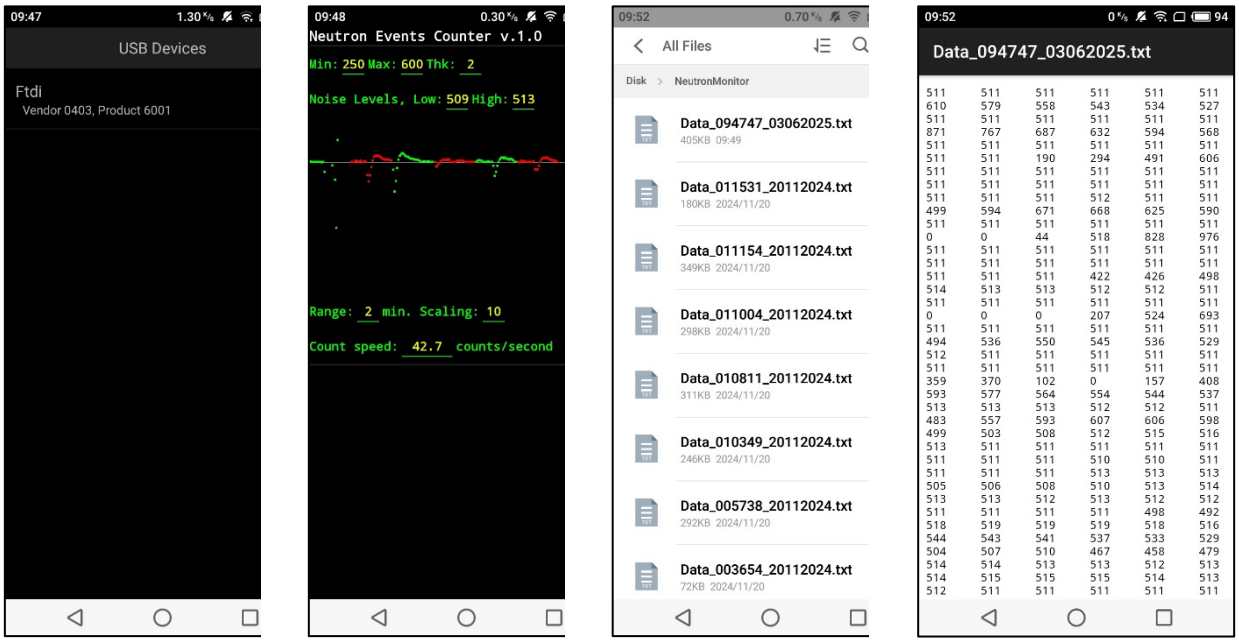

(a) (b) (c) (d)

Figure 4 – (a)-First window after the FTDI chip was detected and program is waiting to proceed to data acquisition; (b)-Main active acquisition window, with preselected by algorithm signal shapes, counting speed and options for different acquisition parameters; (c) – automatically generated file names with the time stamp; (d) - the content of the data file.

As discussed previously, the data processing is built around a single or several features selected as the neutron detection event. The whole buffer is scanned in a loop, and multiple events could be detected in a single buffer. A buffer with at least one event is displayed on the screen for control purposes. The micro USB port throughput of 480 Mbps for USB 2.0 is well above the required speed of the data flow. For the in depth analysis of the buffers with multiple detection events as well as for the overall data sequence statistics, we devised the functional clustering of recorded signal buffers.

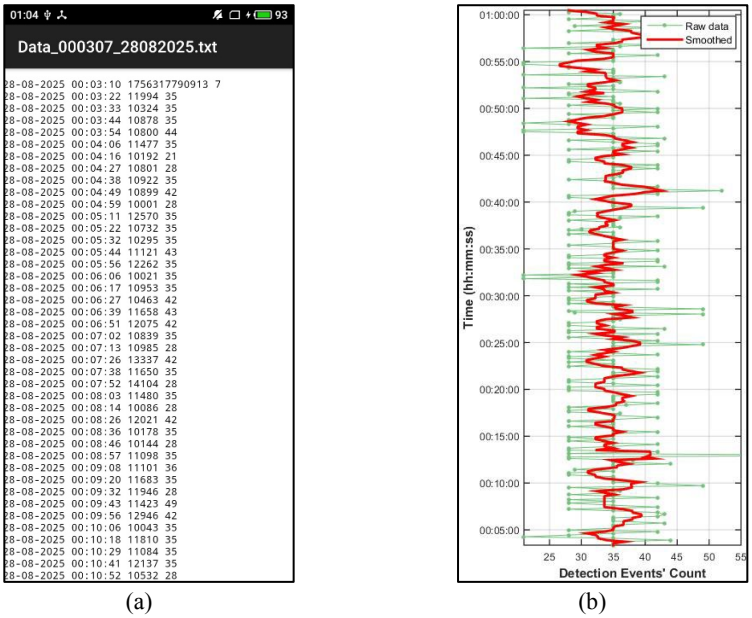

(a) (b)

Figure 5 – (a) Optional, data format for count speed vs time. (b) Matlab generated plot for the data piece on the left with 5-point moving average of 50 seconds.

2.3. Functional clustering approach

The clustering of the neutron detection signals is performed using a model-based functional clustering approach, as described in [18]. This method incorporates functional data analysis techniques to classify signal waveforms into homogeneous groups, ensuring an accurate distinction between neutron-induced events and background noise.

2.3.1. Model formulation

Let N be the number of detected signal events, where each event i is represented by a function $g_i(t)$ observed at discrete time points $t_{i1}, \dots, t_{in_i}$. The clustering model assumes that the data originate from a mixture of G underlying groups, each characterized by a distinct functional pattern and potentially different covariance structures.

The observed signal values y_{ij} at time t_{ij} are modeled as:

$$y_{ij} = g_i(t_{ij}) + \epsilon_{ij}, i = 1, \dots, N, j = 1, \dots, n_i, \quad (2)$$

where ϵ_{ij} represents the normally distributed measurement noise: $\epsilon_{ij} \sim N(0, \sigma^2)$.

Each function $g_i(t)$ is expressed using a basis expansion:

$$g_i(t) = \phi_i^T(t)\eta_i, \quad (3)$$

where $\phi_i(t) = \left(\phi_{i1}(t), \dots, \phi_{ip}(t)\right)^T$ denotes a $p-$ longitudinal vector of the values of the known basis functions of B lines, and η_i is a $p-$vector of unknown random coefficients. These coefficients are assumed to follow a Gaussian mixture model:

$$\eta_i = \mu_{z_i} + \gamma_i, \eta_i \vee z_i = k \sim N_p(\mu_k, \Gamma_k), \quad (4)$$

where z_i is the latent cluster membership variable with prior probabilities $P(z_i = k) = \pi_k$ for $k = 1, \dots, G$, γ_i represents signal-specific within-cluster variability. The variability within each cluster is modelled through the covariance matrix Γ_k, allowing for differences in structure across clusters. We use the R package fdaMocca [19, 20] to perform this model-based clustering method.

2.3.2. Inference and estimation

The model parameters $\theta = \{\pi_k, \mu_k, \Gamma_k, \sigma^2\}$ are estimated via the Expectation-Maximization (EM) algorithm, which iteratively updates cluster assignments and maximizes the observed likelihood. Given a fitted model, each event is assigned to the cluster that maximizes the posterior probability:

$$P(z_i = k \vee y_i, \theta) \propto f_k(y_i, \theta)\pi_k, \quad (5)$$

where $f_k(y_i, \theta)$ denotes the normal density given membership in cluster k.

The optimal number of clusters is chosen using criteria such as the Bayesian Information Criterion (BIC) or the Akaike Information Criterion (AIC). The performance of the clustering model is assessed using entropy-based measures and cross-validation.

3. Results and discussion

The software was initially built for Android version 9.0 and lower (Lollipop), with the possibility of upgrading to a higher version following the recent changes in the security policies for the Android software. It performs well with moderate count speed values. Nevertheless, as expected, the events tend to overlap as soon as the neutron flux increases; see Figure 3(b). This puts a rough estimate of the count speed as 1000 events per second, based on the length of the transmitted buffer. Overlapping, caused by the digitizing hardware specification is aggravated by an extended hardware geometry that could register the multiple events simultaneously. In this case, the other counting algorithm is under development designated to analyze the overlapping signal shapes and increase the potential counting speed of the device. Additionally, the clustering analysis is offered to classify these events retrospectively or on the fly.

It was found that, in long-run experiments, it is practical not to rely on the internal battery capacity of the Android device but on an extra power supply connected through a USB split cable connected to the main power supply.

In the regime where only counting speed is of interest, the counted event data is dampened for every 10 seconds or faster, which is not a problem for internal memory or for micro-SD card read/write speed.

In the case of older devices with limited memory and graphics processing power, the graphical output for the registered signal shape could also be disabled. In addition to counting performance, a preliminary clustering analysis was performed to explore the structure of the recorded signal shapes.

Nuclear physics experiment also relies on the historic data postprocessing, if the experiment is irreproducible, one-of-a-lifetime or for some other reasons, when some efforts are made to clean the data, classify the observed patterns or correct the data acquisition artefacts [21,22].

The cluster analysis of the recorded signals, see Figure 6, resulted in the identification of the eight groups that reflect different types of the signal patterns. The number 8 of the clusters, as an input parameter, has been selected as a preliminary guess to observe the set of the features that could be found in the signal. At this stage these features include but not limited to the combinations of the full signals of different amplitudes or their parts, rear or head, for the classical neutron or gamma ray hit detection events plus the noise. Shape and amplitude analysis are available in the method making it a good tool to differentiate between gamma and neutron events.

Although this is a preliminary analysis, a general grouping can be observed. Some clusters correspond to typical neutron-like signals with a sharp drop followed by recovery, others capture low-amplitude events more consistent with background noise or gamma interactions, and a few clusters represent overlapping or mixed signals where two events occur close in time. The future work will target the overlapped signals decomposition as well.

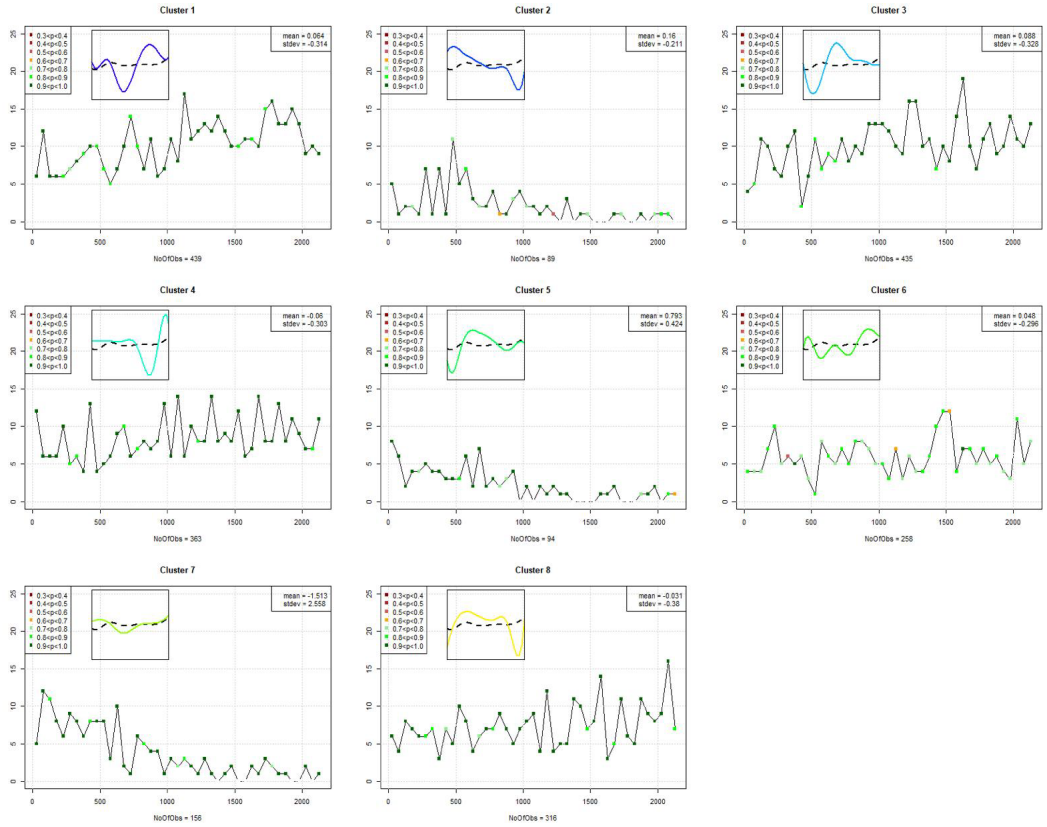

Figure 6 – Estimated dynamics of the eight clusters of standardized signals. The posterior probabilities illustrate the uncertainty in cluster assignment and frequency over time. The colored curves in the sub-window plots represent the cluster-specific mean signals, while the dashed curve denotes the overall mean signal. The upper-right box provides the average of the mean and standard deviation of the signals within each cluster. The p-values are posterior probabilities showing the likelihood that a particular observation belongs to a cluster. Circumstantial visual interpretation of the clusters is the following, from left to the right, from top to bottom: 1. Cluster comprises signals with a sharp initial drop followed by a stable recovery, corresponding to well-formed neutron-like events; 2. Cluster includes moderate-amplitude signals with periodic fluctuations near the baseline, typical of background oscillations or low-energy interactions; 3. Cluster contains short-duration pulses with a distinct early peak and rapid decay, representing fast transient detections; 4. Cluster displays nearly constant low-amplitude traces with minimal variance, interpreted as background noise or incomplete events; 5. Cluster groups high-intensity pulses characterized by steep leading edges and pronounced recovery tails, consistent with strong single neutron captures; 6. Cluster shows overlapping waveforms of mixed amplitude, indicating partially superposed or coincident events within the buffer; 7. Cluster gathers a small number of very high-variance signals with large positive excursions, reflecting saturated or composite detections from simultaneous neutron and gamma interactions; 8. Cluster consists of weak, symmetric pulses oscillating around the baseline, most likely representing residual electronic noise or minor after-pulses of the detector circuit.

Although the exact assignment of clusters to physical processes requires further validation, preliminary results indicate that the method can successfully separate signal shapes into meaningful groups. This provides an important step toward distinguishing neutron-induced events from noise and composite signals, improving the interpretability of the data, and laying the groundwork for a more refined classification in future studies.

Estimated dynamics of the five clusters of standardized signals. The posterior probabilities illustrate the uncertainty in cluster assignment and frequency over time. The colored curves in the sub-window plots show the cluster mean signals, and the dashed curve is the overall mean signal. The upper right box gives the average of the mean and standard deviation of the signals in the cluster.

4. Conclusions

We combined the low-cost and universally available components such as ^{3}He detector tubes, ADC boards, and USB interfaces with Android drivers and our software, for data transfer and handling, to produce a simple and reliable measurement tool with a flexible interface and objectives.

The neutron flux, transformed by a detector tube into an electrical signal, is digitized and sent through the data cable to a smartphone. The raw data, after being received from a signal buffer, is searched simultaneously for the characteristic shapes of the neutron detection event and treated further for hits counting or signal amplitude measurements to produce the power spectrum (yet to be implemented).

Additionally, by employing the robust estimation approach, the model effectively differentiates neutron signal patterns from background noise and gamma ray events, ensuring accurate classification and enhanced detection performance. At present, this advanced retrospective analysis is done, using the R language, separately on a PC. Nevertheless, it could be ported to an Android device for on-the-fly or retrospective data filtering and signal analysis in future development.

Acknowledgments. This research has been funded by the Science Committee of the Ministry of Education and Science of the Republic of Kazakhstan (Grant No. BR21881930).

References

1. Ishikawa N., Nadeem, Nomura H., Yoda Y., Uetsuki O., Fukunaga K., Nagoya S., Sawara J., Ishihata H., Senoguchi J. High-performance distributed computing with smartphones // In: Zeinalipour D. et al. (eds.) Euro-Par 2023 International Workshops, Limassol, Cyprus, August 28–September 1, 2023, Revised Selected Papers, Part II. – Cham: Springer, 2024. – (Lecture Notes in Computer Science; Vol. 14352). – Pp. 229–232. https://doi.org/10.1007/978-3-031-48803-0

2. Temirzhanov A., Sadykov B., Zholdybayev T., Duisebayev B., Ussabayeva G., Kerimkulov Z. STM32F407 microcontroller based multichannel analyzer for spectroscopy // Physical Sciences and Technology. – 2024. – Vol. 11, No. 3–4. – Pp. 21–28. https://doi.org/10.26577/phst2024v11i2b03

3. Budden B. S., Stonehill L. C., Dallmann N., Baginski M. J., Best D. J., Smith M. B., Graham S. A., Dathy C., Frank J. M., McClish M. A. A Cs_2LiYCl_6:Ce-based advanced radiation monitoring device // Nuclear Instruments and Methods in Physics Research Section A: Accelerators, Spectrometers, Detectors and Associated Equipment. – 2015. – Vol. 784. – Pp. 97–104. https://doi.org/10.1016/j.nima.2014.11.051

4. Bourbeau J., Campos F., Gallay B., Meehan M., Morgan R., Peacock J., Pizzuto A., Schneider C., Simons A. L., Vandenbroucke J., Winter M. Particle identification in smartphone camera images using the Distributed Electronic Cosmic-ray Observatory // In: Proceedings of the 36th International Cosmic Ray Conference (ICRC 2019), Madison, USA, July 24–August 1, 2019. – PoS(ICRC2019)390. – Published online: August 17, 2025. – https://pos.sissa.it/PoS(ICRC2019)390

5. Bee Research Pty Ltd. ^{3}He Neutron Detector GS-Neutron-3: High-Efficiency ^{3}He Neutron Tube with Built-in Bluetooth [Electronic resource]. – Sydney, Australia: Gammaspectacular. – Available at: https://www.gammaspectacular.com/blue/gamma-spectroscopy/neutron-detectors/gs-neutron-3 (Available on December 16, 2025).

6. University of Delaware, Bartol Research Institute. BARTOL Neutron Monitors Program. – Available at: https://neutronm.bartol.udel.edu/Welcome.html (Available on December 16, 2025).

7. Muhametuly B., Duysebayev A. CCD camera in a neutron imaging system for real time and tomography investigations // Physical Sciences and Technology. – 2016. – Vol. 2, No. 2. – Pp. 18–27. https://doi.org/10.26577/2409-6121-2015-2-2-18-27

8. Dyachkov V. V., Zaripova Y. A., Yushkov A. V., Shakirov A. L., Bigeldiyeva M. T., Abramov K. E. Periodic variations in time of atmospheric alpha and beta radioactive nanoparticles // Physical Sciences and Technology. – 2019. – Vol. 6, No. 1–2. – Pp. 11–17. https://doi.org/10.26577/phst-2019-1-p6

9. Kunakov S. K., Shapiyeva A. Fission fragments and primary electrons' energy distribution in helium-3 plasma irradiated by neutron flux // Physical Sciences and Technology. – 2019. – Vol. 5, No. 3–4. – Pp. 78–82. https://doi.org/10.26577/phst-2018-2-160

10. Saduev N. Study of the Processes of interaction of neutrons and charged particles with beryllium nuclei [Master's thesis, electronic resource]. – Al-Farabi Kazakh National University, 2014. – 116 p.

11. Android Developers. USB Host Overview [Electronic resource]. – 23 May 2025. – Available at: https://developer.android.com/develop/connectivity/usb/host (accessed 16.12.2025).

12. R Core Team. R: A Language and Environment for Statistical Computing [Electronic resource]. – Vienna, Austria: R Foundation for Statistical Computing, 2025. – Available at: https://www.R-project.org/ (accessed 16.12.2025).

13. Shalev S., Hopstone P. Empirical expressions for gas multiplication // Nuclear Instruments and Methods. – 1978. – Vol. 155, No. 1–2. – P. 237–247. https://doi.org/10.1016/0029-554X(78)90209-4

14. Vasilyev I. A., Djilkibaev R. M., Hlustin D. V. Investigation of the pulse shape in a ^{3}He counter under neutron irradiation // Instruments and Experimental Techniques. – 2020. – Vol. 63, No. 2. – P. 146–153. https://doi.org/10.1134/S0020441220010236

15. Wakerly M., Morich K. Usb-serial-for-android: Android USB Host Serial Driver Library for CDC, FTDI, Arduino and Other Devices [Software, electronic resource]. – GitHub, Version 3.9.0, 10 March 2025. – Available at: https://github.com/kai-morich/usb-serial-for-android (Available on December 16, 2025).

16. Lee D. W., Stonehill L. C., Klimenko A., Terry J. R., Tornga S. R. Pulse-shape analysis of Cs_2LiYCl_6:Ce scintillator for neutron and gamma-ray discrimination // Nuclear instruments and methods in physics research section A. – 2012. – Vol. 664, No. 1. – Pp. 1–5. https://doi.org/10.1016/j.nima.2011.10.013

17. Yamaki S., Morimoto K., Kaji D., Wakabayashi Y., Takeyama M., Tanaka K., Tanaka T., Baba H., Yamaguchi H., Suzuki T., Morita K. R&D status of pulse shape analysis for short-lived decay of superheavy elements in GARIS-II // Physical Sciences and Technology. – 2017. – Vol. 3, No. 1. – Pp. 12–16. https://doi.org/10.26577/phst-2016-1-88

18. Arnqvist P., Sjöstedt de Luna S. Model Based Functional Clustering of Varved Lake Sediments [Preprint, electronic resource]. – arXiv:1904.10265, 2019. – Available at: https://arxiv.org/abs/1904.10265 (Available on December 16, 2025)

19. Arnqvist P., Sjöstedt de Luna S., Pya N. fdaMocca: an R package for model-based clustering for functional data with covariates // In: Skiadas C. H., Skiadas C. (eds.) Quantitative methods and data Analysis in applied demography. Vol. 2: Data, Models, Risk and Surveys. – Cham: Springer, 2025. – (The Springer Series on Demographic Methods and Population Analysis; Vol. 58). – Pp. 95–108. https://doi.org/10.1007/978-3-031-82279-7

20. Pya N., Arnqvist P., Sjöstedt de Luna S. fdaMocca: Model-Based Clustering for Functional Data with Covariates [Software, electronic resource]. – R package version 0.1-2. – CRAN, 31 March 2025. – Available at: https://CRAN.R-project.org/package=fdaMocca (Available on December 16, 2025).

21. Kussainov A. S., Saduev N. O., Em M. A., Mukhatay M. A., Myrzabek Y. T. Simple, contrast-based compartmentalization in 3D reconstruction from CT images // Physical Sciences and Technology. – 2020. – Vol. 7, No. 1–2. – Pp. 38–42. https://doi.org/10.26577/phst.2020.v7.i1.06

22. Aghabozorgi S., Seyed Shirkhorshidi A., Wah T. Y. Time-series clustering – a decade review // Information Systems. – 2015. – Vol. 53. – Pp. 16–38. https://doi.org/10.1016/j.is.2015.04.007

Information about authors:

Arman S. Kussainov (corresponding author) – Senior Lecturer at the Faculty of Physics and Technology, Al-Farabi Kazakh National University (Almaty, Kazakhstan, e-mail: arman.kussainov@gmail.com).

Per Arnqvist – Associate Professor at the Department of Mathematics and Mathematical Statistics, Umeå University (Umeå, Sweden, e-mail: per.arnqvist@umu.se).

Natalya Pya Arnqvist – Associate Professor, Department of Mathematics and Mathematical Statistics, Umeå University (Umeå, Sweden, e-mail: natalya.pya@umu.se).

Nurzhan Saduyev – Deputy Director General for Science of the Institute of Nuclear Physics (Almaty, Kazakhstan, e-mail: n.sadyev@inp.kz).

Orazaly Kalikulov – Head of Cosmic Ray Physics Laboratory, Institute of Nuclear Physics (Almaty, Kazakhstan, e-mail: o.kalikulov@inp.kz).

Nurzhan Yerezhep – Lecturer at the Physics and Technology Department, Al-Farabi Kazakh National University, Researcher at the Cosmic Ray Physics Laboratory, Institute of Nuclear Physics (Almaty, Kazakhstan, e-mail: n.yerezhep@inp.kz).

Shynbolat Utey – Lecturer at the Faculty of Physics and Technology, Al-Farabi Kazakh National University, Researcher at the Cosmic Ray Physics Laboratory, Institute of Nuclear Physics (Almaty, Kazakhstan, e-mail: sh.utey@inp.kz).

Aliya Baktoraz – Lecturer at the Faculty of Physics and Technology, Al-Farabi Kazakh National University (Almaty, Kazakhstan, e-mail: baktoraz.aliya@kaznu.kz).

IRSTI 29.19.16 https://doi.org/10.26577/phst20251229

Computer simulation of planar bifacial TOPCon solar cells by using Quokka 3 software

I.V. Zhirkov , A.M. Suleimenova ,
A.T. Sultanov* and N.B. Beisenkhanov

Kazakh-British Technical University, Almaty, Kazakhstan
*e-mail: a.sultanov@kbtu.kz

(Received May 8, 2025; received in revised form November 12, 2025; accepted November 26, 2025)

This study presents a comprehensive simulation-based analysis of bifacial Tunnel Oxide Passivated Contact (TOPCon) solar cells using the Quokka 3 software. It investigates the impact of different antireflection coatings and rear albedo variations on device performance. One of the main findings is the significant improvement in optical and electrical properties after applying MgF_2 antireflection coating on top of the cell. Structures with the addition of MgF_2 achieved low, uniform reflectance and increased light absorption across the full solar spectrum. Compared to structures without MgF_2, those with the coating exhibited superior external quantum efficiency (EQE) and reduced reflected photocurrent density (J_R) with the value of 3.38 mA/cm^2. Additionally, simulations revealed that increasing rear albedo values improved short-circuit current density (J_{sc}) and power conversion efficiency (PCE). The highest PCE of 27.37% and J_{sc} of 45.07 mA/cm^2 was obtained from a structure combining MgF_2 and a rear albedo of 0.3 Voc in this case was equal to 0.74V. These results confirm that optimizing both antireflection coatings and rear-side illumination can significantly improve the efficiency of bifacial TOPCon solar cells, offering a viable pathway for enhanced photovoltaic (PV) performance.

Keywords: Si solar cell, TOPCon solar cell, bifacial solar cell, Quokka 3, antireflection coatings.
PACS number(s): 84.60.Jt, 68.65.Ac, 42.70.−a.

1. Introduction

Since the development of silicon (Si)-based solar cells, the photovoltaic industry has undergone rapid growth. Fueled by the increasing global demand for clean and renewable energy, extensive research has been directed toward advancing solar cell technologies. This effort has led to numerous scientific achievements, including the recent emergence of Tunnel Oxide Passivated Contact (TOPCon) Si solar cells. Renowned for their excellent passivation properties, reduced recombination losses, and high-power conversion efficiency (PCE), TOPCon technology represents a promising advancement in the field.

The TOPCon solar cell was first developed by the Fraunhofer Institute for Solar Energy (ISE) Systems in Germany in 2013, showing an efficiency of 23.7%[1]. After several advancements such as optimizing the wafer resistivity and process flow, PCE was further elevated to higher values of ~25.7% and a high fill factor (FF) of ~83.3% in 2017 also at Fraunhofer ISE [2].

The main feature of fabricating TOPCon cells involves inserting a very thin interfacial silicon oxide (SiO_x) layer, typically around 1-2 nm, between doped polycrystalline Si (poly-Si) and crystalline Si (c-Si) layers, enhancing the collection of photogenerated carriers. Several research teams[1–5] have shown that combining a highly doped poly-Si layer with an ultrathin SiO_x layer provides low saturation current density (J_0<5 fA/cm²) and low contact resistivity (ρ_c<1 mΩ·cm²) simultaneously. This results in outstanding surface passivation with minimal recombination losses. The exceptional properties of the TOPCon structure are largely attributed to its key advantage: the c-Si wafer does not come into direct contact with the metal electrodes. This design helps reduce the Fermi level pinning (FLP) effect, thereby improving device performance and stability [3].

Recent developments in TOPCon structures have increased their market share and accelerated large-scale industrial production, supported by improved architecture such as integration with existing PERC lines and compatibility with high-efficiency silicon

tandem cells. Moreover, the configuration of bifacial TOPCon devices, generating energy from both the front and rear sides of the cell, has been actively explored in recent studies [6–9]. The front side functions like a standard solar cell, directly absorbing sunlight and converting it into electricity, while the rear side is designed to absorb light that is reflected off the ground or nearby surfaces, as well as diffused light from the atmosphere. This reflected and diffused solar radiation is measured by the term, called "albedo".

Albedo is the most significant factor for bifacial solar cells as it influences energy production. Surfaces with higher albedo reflect more light, consequently increasing the energy yield. Thus, optimizing the design of bifacial TOPCon cell can further improve energy output and become particularly attractive for large-scale solar power plants. Table 1 presents albedo values for different surfaces.

While experimental characterization of bifacial TOPCon cells requires significant efforts, computer simulations provide versatile and simple way to study this structure. In this context, Quokka 3, a finite-volume-based simulation software, allows full-cell modeling, becoming a valuable tool for analyzing the performance of solar cells [11, 12].

Table 1 – Albedo values for various types of surfaces [10].

Surface	Corrugated roof	Colored paint	Trees	Asphalt	Concrete	Grass	Ice
Albedo	0.1 – 0.15	0.15 – 0.35	0.15 – 0.18	0.05 – 0.2	0.25 – 0.3	0.25 – 0.3	0.3 – 0.5

Surface	Red/Brown roof tiles	Brick/Stone	Oceans	Old snow	White paint	Fresh Snow
Albedo	0.1 – 0.35	0.2 – 0.4	0.05 – 0.1	0.65 – 0.81	0.5 – 0.9	0.81 – 0.88

Computer simulations play a crucial role across all fields of scientific research, providing deeper insights and enabling more accurate predictions of experimental outcomes [13, 14]. In this research, we focus on a computer simulation of a bifacial TOPCon solar cell using Quokka 3 software. Our analysis includes utilization of antireflection coatings (ARC) based on transparent conductive oxides (TCO) such as Indium tin oxide (ITO), aluminum doped zinc oxide (AZO) and ARC based on magnesium fluoride (MgF_2) [15, 16]. Furthermore, we evaluated key performance metrics such as current-voltage (*J-V*) characteristics, reflectance spectra, external quantum efficiency (EQE), photocurrent density measurements and albedo-dependent characteristics of TOPCon solar cells with different ARCs. By comparing structures with different ARC of TOPCon solar cell, this study aims to identify the most efficient design. The findings contribute to a deeper understanding of bifacial TOPCon behavior and offer guidance for future development. By simulating bifacial solar cells, the study aims to highlight the performance advantages of bifacial operation and the influence of rear-side illumination in realistic operating environments.

2. Simulation details

Quokka 3 simulations were employed to demonstrate the performance differences between bifacial and standard TOPCon solar cells. Figure 1 illustrates the simulated geometries of both the bifacial and standard cells within the Quokka 3 software environment. The simulation parameters, which provides a detailed overview of the values used throughout the modeling process are summarized in Table 2. Throughout the study parameters such as ARC layer, rear albedo, and bifacial or standard structure mode were varied. Fixed parameters included bulk wafer properties (200 μm, 1 Ω·cm), poly-Si thickness (30 nm), doping densities, and recombination velocities, which were held constant based on typical literature values. For the bifacial cell simulations, the TOPCon+TCO structures were modeled by incorporating sheet resistance and saturation current density characteristics specific to bifacial designs. In contrast, the standard TOPCon solar cell was simulated using built-in Quokka 3 TOPCon structures for the rear side. This approach allowed for a clear comparison between the two architectures under consistent simulation conditions.

In the TOPCon solar cell structure, both the front and rear sides include poly-Si layers alongside a SiO_x tunneling layer. The poly-Si layer thickness was optimized to 30 nm, as this value was found to balance passivation quality and carrier transport efficiency [6, 17–19]. For the regular structure the rear side of the TOPCon solar cell was covered by silver (Ag) back electrode. A triple-layer coating composed of ITO-AZO-ITO was used as the transparent electrode on the front side. For the bifacial TOPCon solar cell ITO-AZO-ITO transparent electrode was used on both sides of the solar cell. To maximize optical performance of the TOPCon solar cell MgF_2 was used as an ARC on the top of the ITO-AZO-ITO transparent electrode. Figure 2 illustrates different structural combinations of TOPCon solar cells used in this work.

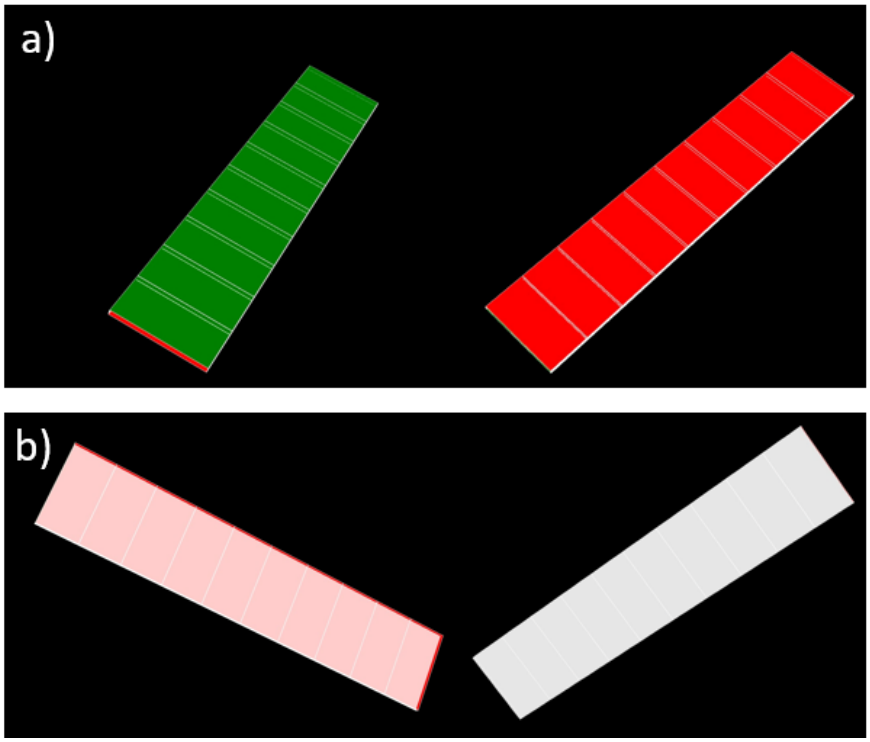

Figure 1 – 3D view of TOPCon solar cell derived from Quokka 3 software program : a) bifacial structure, b) standard structure.

Table 2 – Simulation parameters obtained from Quokka 3: Bulk parameters, external circuit, front n-type TOPCon + TCO layer, rear p-type TOPCon (Standard), rear p-type TOPCon (Bifacial) + TCO parameters.

Bulk parameters	
Dimensions	2
Thickness	200 µm
Width	18000 µm
Resistivity(Bulk)	1 Ohm*cm
Facing angle front/rear	0
Doping type	p-type
Fundamental electron surface recombination velocity(n)	100 cm/s
Fundamental electron surface recombination velocity(p)	100 cm/s
Defect energy relative to intrinsic energy	0 eV
Ilumination spectrum Rear/Front	AM1.5g

Continuation of the table

Ilumination scale Frontside	1
Ilumination scale Rearside	(0,0.3) with step 0.02
External cicuit	
Rseries	0.46 Ohmcm^2
Rshunt	3.5E3 Ohmcm^2
Saturation current density of external diode	0 Acm^{-2}
Ideality factor of external diode	2
front n-type TOPCon +TCO layer	
ConductionType	n-type
Rsheet	90.58 Ohm/square
Non Contacted Recombination *Jo*	2 fA/cm^2
Contacted Recombination	20 fA/cm^2
Thickness(poly-Si)	30nm
DopingDensity	1E20 cm^{-3}
Contact shape	Rectangle
Contact size	30 µm
Contact pitch	1800 µm
Contact repetition	11
Contact Ohmic Resistivity	5E-5 Ohmcm^2
Metal Rsheet	0.003 Ohm
rear p-type TOPCon (standard)	
Conduction type	p-type
DopingDensity	1E19 cm^{-3}
Thickness	30 nm
fundamental electron surface recombination velocity	10 cm/s
fundamental hole surface recombination velocity	10 cm/s
Contact shape	Full
Contact size	18000 µm
Contact Ohmic Resistivity	5E-5 Ohmcm^2
Metal Rsheet	0.003 Ohm
rear p-type TOPCon (Bifacial) +TCO	
Conduction type	p-type
Rsheet	90.58 Ohm/square
NonContactedRecombination *Jo*	2 fA/cm^2
ContactedRecombination	20 fA/cm^2
Thickness(poly-Si)	30nm
DopingDensity	1E20 cm^{-3}
Contact shape	Rectangle
Contact size	30 µm
Contact pitch	1800 µm
Contact repetition	11
Contact Ohmic Resistivity	5E-5 Ohmcm^2
Metal Rsheet	0.003 Ohm

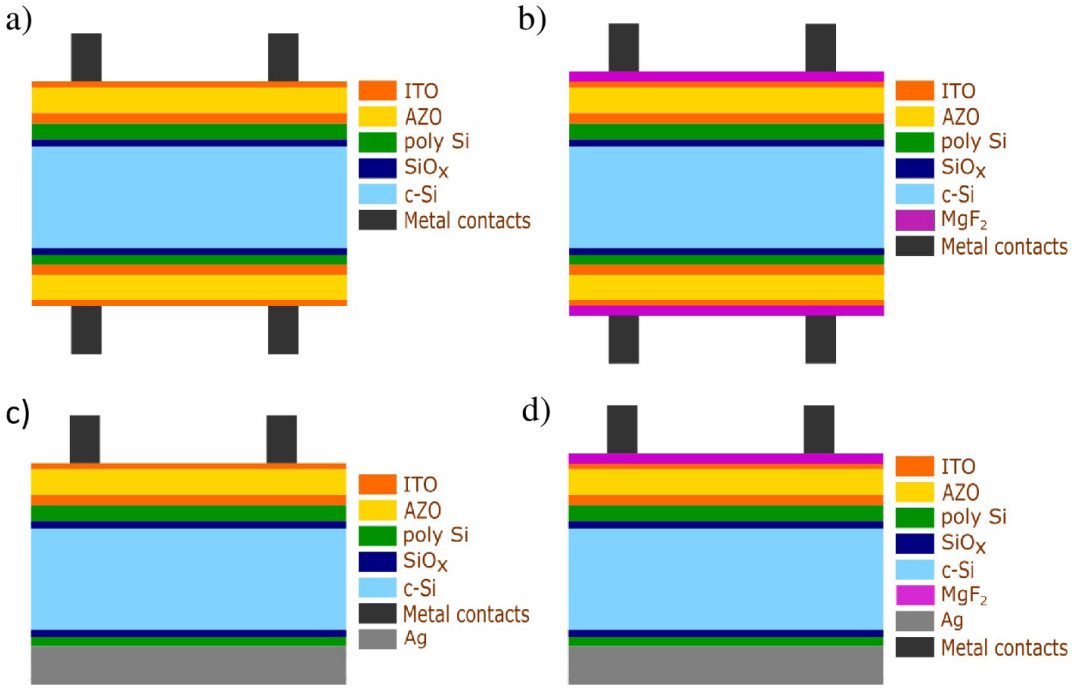

Figure 2 – Two-dimensional schematics of c-Si-based TOPCon solar cell:
a) Simplified cell structure without MgF_2 and Ag, b) Cell structure with MgF_2 on both sides without Ag layer,
c) Simplified cell structure with Ag at the bottom d) Cell structure with MgF_2 on top and Ag at the bottom.

OPAL 2 optical simulator [20] was used to optimize the thickness of the transparent TCO electrode and MgF_2 ARC for improved optical performance. During optimizations the goal was set to achieve maximum photon current absorbed in the active layer. Due to the layer number limitations of the OPAL 2 simulator, the thicknesses of the ITO-AZO-ITO multilayer were initially optimized as a standalone structure. Once the optimal configuration was determined, the MgF_2 layer was optimized separately. To accommodate the simulator's constraints, the previously optimized ITO-AZO-ITO structure was modeled as a single ITO-equivalent layer, with the MgF_2 layer added on top of this simplified model.

To further analyze the optical properties of the considered TOPCon solar cells, reflectance, parasitic absorption, and absorption within the active area were simulated using SCOUT software [21]. The absorption characteristics of each layer were evaluated individually, and the total parasitic absorption was calculated as the sum of absorption in all layers except the substrate.

The optical constants (n and k) for ITO and AZO were taken from the works of [22, 23]. The optical constants for MgF_2 are taken from [24], as linked in the OPAL 2 database. All other layers, including the substrate and back layers, were obtained from the SCOUT software [21].

3. Results and discussion

For accurate modeling and simulation of the optical behavior of the TOPCon solar cell, reliable refractive index (n) and extinction coefficient (k) data are essential. Figure 3 shows the wavelength-dependent optical constants for different materials used in the TOPCon solar cell. AZO exhibits a lower extinction coefficient than ITO, which ensures higher transmittance of ITO-AZO-ITO structure compared to an ITO-only structure. The ITO-AZO-ITO structures were examined in detail in our previous work[25].

Across the entire range, MgF_2 shows minimal extinction coefficient values, highlighting its highly transparent dielectric property. Moreover, it is well established that to minimize reflectance from a solar cell surface, it is essential to use materials with a gradually increasing refractive index from air to the substrate. The optimal refractive index n for the material used as an ARC can be calculated using the formula [26]:

$$r = \left[\frac{n_{air}\, n_s - n^2}{n_{air}\, n_s + n^2}\right]^2, \qquad (1)$$

where n_s is a refractive index of the substrate, n_{air} is a refractive index of air and n is a refractive index of the film.

According to the calculations refractive index of MgF_2 (~1.38) is suitable to reduce reflection from TOPCon solar cell. Thus, in this work, TOPCon solar cell are considered with and without MgF_2 ARC.

Figure 4a shows the simulated reflectance spectra of the TOPCon structures with and without the MgF_2 ARC over the 300–1200 nm wavelength range. For reference, the solar irradiation spectrum is shown in the background. The structure with MgF_2 layer shows relatively low and constant reflectance throughout the spectrum, suggesting effective antireflection behavior. Moreover, it experiences a noticeable decrease in reflectance between 600–700 nm. This reduction in reflectance is attributed to the low refractive index of MgF_2, which reduces the refractive index mismatch between the underlying layers and air. The refractive index of MgF_2 exhibits only minor variation across the entire solar spectrum while other refractive indexes experiencing constant decrease on the most part of spectrum, with the wavelength range of 600–700 nm providing the most noticeable smooth refractive index gradient between the underlying layers and air. However, the structure without MgF_2 demonstrates a sharp reduction of reflectance at around 600 nm, suggesting that careful design of multilayer structure can achieve low reflectance at specific wavelengths. Overall, while the addition of MgF_2 layer provides more consistent antireflective behavior across the broad spectrum, the structure without MgF_2 offers potential for targeted wavelength optimization through multilayer structure engineering.

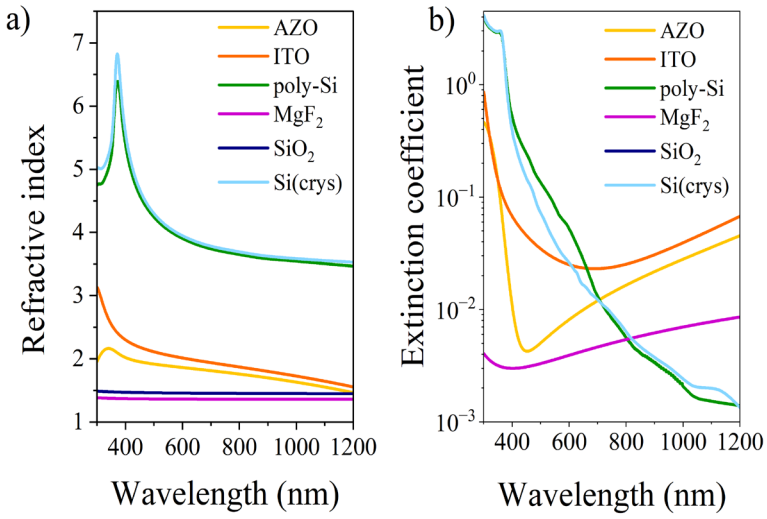

Figure 3 – Optical properties: a) Refractive index and b) extinction coefficient as functions of wavelength for various materials (AZO, ITO, poly-Si, MgF_2, SiO_2, Si).

Figure 4b illustrates the EQE simulations for structures with and without MgF_2, which is significantly influenced by the optical constants n and k, where the refractive index n determines the proportion of photons reflected at the interfaces between layers, while the extinction coefficient k governs the extent to which photons can penetrate into the bulk layer and the fraction that is transmitted without being absorbed. The structure with MgF_2 layer exhibits higher performance across most of the wavelength range compared to the structure without MgF_2. This is also evident in the calculated current density (J), which shows that the final J value for the solar cell with MgF_2 ARC is higher. However, due to the decrease in reflectance between 450 nm and 700 nm, the structure without MgF_2 shows slightly better performance in this region. Overall, the addition of the MgF_2 layer improves the EQE, indicating enhanced light management and reduced reflection due to the antireflective effect provided by MgF_2.

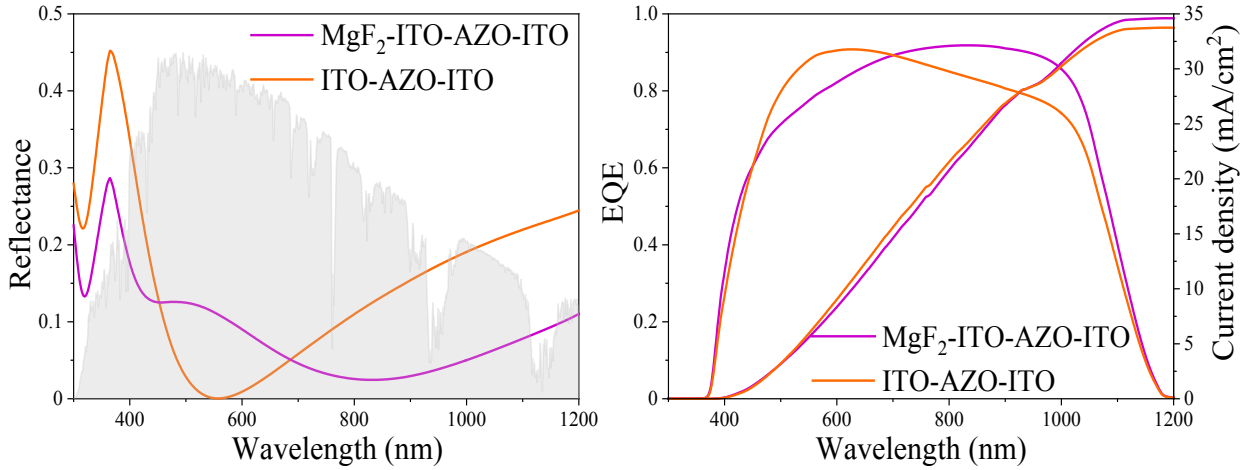

Figure 4 – a) Reflectance spectra of ITO-AZO-ITO and MgF_2-ITO-AZO-ITO structures; b) EQE measurements for standard TOPCon solar cell with ITO-AZO-ITO and MgF_2-ITO-AZO-ITO ARC.

To provide a comprehensive description of the optical properties of the structure, photon current density calculations were performed. 3 main characteristics were calculated: reflected photon current density (J_R), parasitic absorption current density (J_{PA}) and absorbed photon current density in the substrate (J_{Abulk}). As optimizing useful absorption is essential for solar cell performance, the $J_{R,}$ J_{PA} and J_{Abulk} was determined for the wavelength intervals of 300–1200 nm by the following equation [27]:

$$J_x = \int_{\lambda 2}^{\lambda 1} X(\lambda) F(\lambda) q d\lambda, \quad (2)$$

where X (λ) is reflectance, parasitic absorption or absorption in the bulk, F (λ) is the incident photon flux density of AM1.5G irradiation, q is the elementary charge, and λ is the wavelength.

Figure 5 provides J_R, J_{PA}, J_{Abulk} calculations for different structures. Comparing bifacial and standard structures. According to the result all current density values show minimal differences, indicating that the back reflection from the rear Ag electrode is negligible. However, the addition of the MgF_2 layer to the ITO-AZO-ITO structure leads to significant decline of J_R from 5.44 to 3.38 mA/cm², subsequently refining J_{PA} and J_{Abulk} values This suggests that addition of MgF_2 acts effectively, redirecting previously reflected light into the active layer and enhancing useful absorption.

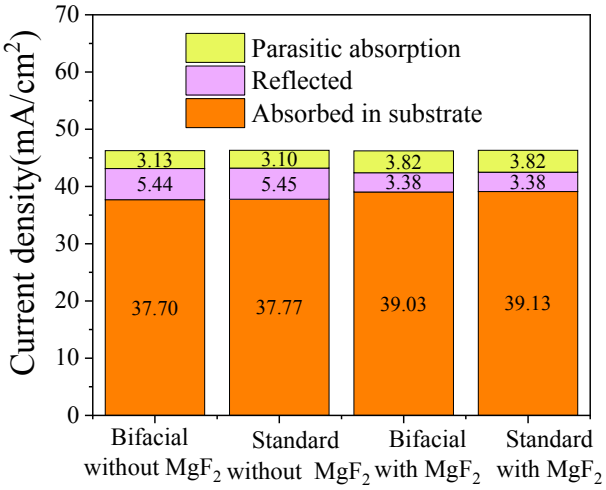

Figure 5 – Photo current density measurements for four configurations (Bifacial (ITO-AZO-ITO); Standard (ITO-AZO-ITO); Bifacial (MgF_2-ITO-AZO-ITO); Standard (MgF_2-ITO-AZO-ITO). Three types of current densities are compared: Reflected current (J_R), parasitic absorption current (J_{PA}), current absorbed in the substrate (J_{Abulk}).

Figure 6 presents the *J–V* characteristics of TOPCon solar cells with and without a MgF_2 ARC under varying rear-side albedo conditions. For clarity, Figures 6a and 6b depict the results for a standard and a bifacial TOPCon solar cell, with albedo intensities varying from 0 to 0.3 suns in 0.1 increments. Even in the absence of rear illumination (0 suns), the bifacial TOPCon solar cell exhibits a PCE of 20.56%, slight-

ly lower than that of the reference structure with a Ag back reflector (20.94%). This trend remains consistent for both MgF_2-coated and uncoated devices. Upon introducing a modest rear albedo of 0.1 suns, the bifacial structure demonstrates an almost 2% absolute increase in PCE, emphasizing the sensitivity of the device to even minor enhancements in rear-side illumination. This improvement is primarily attributed to the significant rise in short-circuit current density (J_{sc}), while the open-circuit voltage (V_{oc}) remains nearly constant across all albedo levels.

Figures 6c and 6d provide a more detailed analysis of the bifacial configuration, displaying the evolution of *J–V* parameters as the albedo varies from 0 to 0.3 suns in finer steps of 0.02. The results show an almost linear increase in J_{sc} with albedo, while V_{oc} changes slightly, from 0.73 to 0.74 V. These findings confirm that the observed PCE enhancement is predominantly governed by the increase in photocurrent. Furthermore, devices incorporating MgF_2 ARC consistently outperform those without it under all albedo conditions. The MgF_2 layer, in conjunction with enhanced rear illumination, improves light trapping and optical coupling, thereby boosting the internal photon generation rate. These outcomes highlight that increasing back albedo, especially when combined with optimized optical coatings, is a highly effective strategy for enhancing the photocurrent and overall performance of TOPCon solar cells.

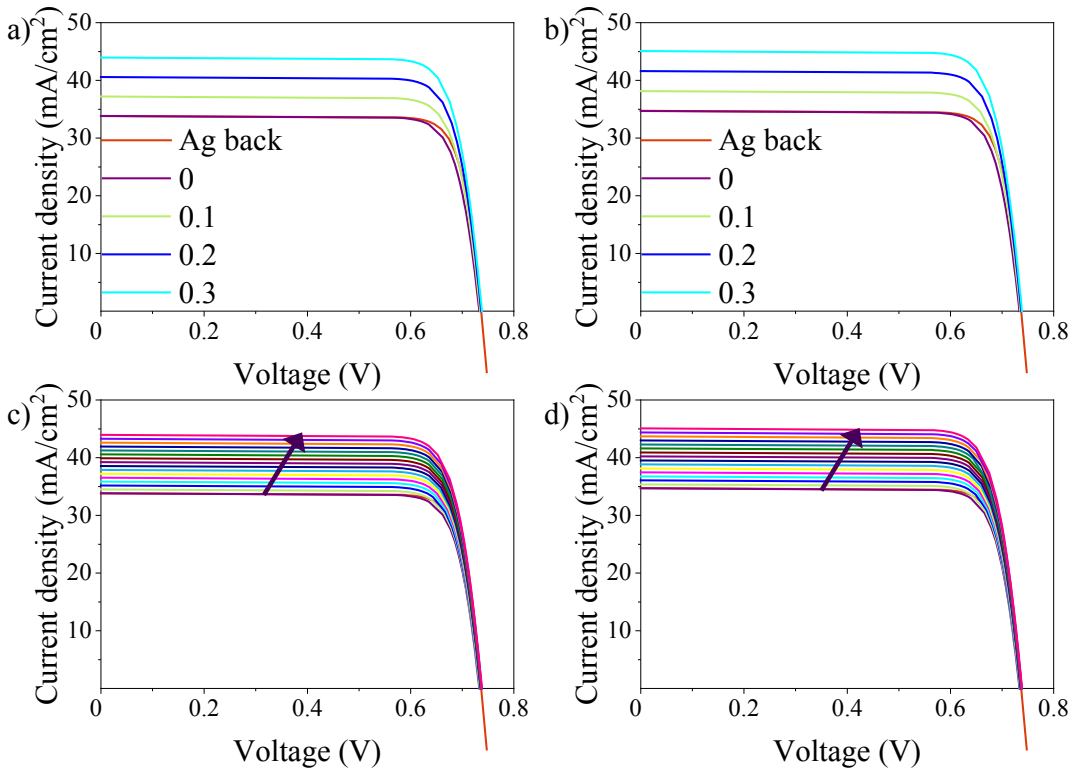

Figure 6 – *J–V* Characteristics Under Varying Back Albedo for structures with MgF_2 on the top and without MgF_2: a),b) shows changes to *J*-V curve of bifacial structure in comparison to standard Ag back solar cells, pictures c),d) shows changes to *J*-V curve with increase of back albedo from 0 to 0.3 with the step of 0.02(arrow show direction of increased albedo).

Tables 3 and 4 presents extensive data results based on Quokka 3 simulation. From previous discussion it was mentioned that J_{sc} increases with increase of back albedo and Tables 3 and 4 proves this for both cases with and without MgF_2. The same is true for PCE. For the structures without MgF_2, the highest value of PCE is achieved at 26.69 %, while TOPCon solar cell with MgF_2 ARC on top show the maximum value of 27.37 %. This results also shows precisely the point where V_{oc} for bifacial solar cell reaches the

value for standard TOPCon solar cell. For TOPCon solar cells without MgF_2 the required albedo is 0.12 suns while with MgF_2 implemented cells 0.08 suns albedo is already enough. Even though bifacial solar cell provides better result for PCE, V_{oc} and J_{sc} it's important to point out that standard solar cells for both cases showed maximum FF while bifacial structure showed decrease in FF with increase of albedo.

Table 3 – Bifacial TOPCon solar cell characteristics: open-circuit voltage (V_{oc}), short-circuit current density (J_{sc}), fill factor (FF), power conversion efficiency (PCE) values for structures without MgF_2.

Optical Rear Illumination Scale Without MgF_2	V_{oc} (V)	J_{sc} (mA/cm^2)	FF (%)	PCE (%)
Ag back	0.74	33.84	83.99	20.94
0	0.73	33.81	82.93	20.56
0.02	0.73	34.49	82.89	20.97
0.04	0.73	35.16	82.85	21.38
0.06	0.73	35.84	82.81	21.79
0.08	0.73	36.51	82.76	22.20
0.1	0.73	37.19	82.73	22.61
0.12	0.74	37.86	82.69	23.02
0.14	0.74	38.54	82.65	23.43
0.16	0.74	39.22	82.60	23.84
0.18	0.74	39.89	82.56	24.25
0.2	0.74	40.57	82.52	24.66
0.22	0.74	41.24	82.47	25.07
0.24	0.74	41.92	82.43	25.47
0.26	0.74	42.59	82.38	25.88
0.28	0.74	43.27	82.34	26.29
0.3	0.74	43.94	82.29	26.69

Table 4 – Bifacial TOPCon solar cell characteristics: open-circuit voltage (V_{oc}), short-circuit current density (J_{sc}), fill factor (FF), power conversion efficiency (PCE) values for structures with MgF_2.

Optical Rear Illumination Scale with MgF_2	V_{oc} (V)	J_{sc} (mA/cm^2)	FF (%)	PCE (%)
Ag back	0.74	34.71	83.94	21.48
0	0.73	34.68	82.88	21.08
0.02	0.73	35.37	82.84	21.51
0.04	0.73	36.06	82.79	21.93
0.06	0.73	36.76	82.75	22.35
0.08	0.74	37.45	82.71	22.77
0.1	0.74	38.14	82.67	23.19
0.12	0.74	38.83	82.63	23.61
0.14	0.74	39.53	82.58	24.03
0.16	0.74	40.22	82.54	24.45
0.18	0.74	40.91	82.49	24.87

Continuation of the table

Optical Rear Illumination Scale with MgF_2	V_{oc} (V)	J_{sc} (mA/cm^2)	FF (%)	PCE (%)
0.2	0.74	41.60	82.45	25.29
0.22	0.74	42.30	82.40	25.70
0.24	0.74	42.99	82.36	26.12
0.26	0.74	43.68	82.31	26.54
0.28	0.74	44.38	82.26	26.95
0.3	0.74	45.07	82.21	27.37

Overall, the findings underscore the significance of combining advanced ARC strategies–such as MgF_2-capped multi-layer designs–with effective utilization of bifacial architectures. The implementation of ARC structure allowed for better energy distribution between used and not used energy. While implementation of rear side illumination explicitly shows increase in J_{sc}. Such integrated optimization not only boosts the efficiency of TOPCon cells but also maximizes their energy yield in real-world operating conditions. The achieved efficiency of 27.37% under a rear albedo of 0.3 with MgF_2 outperforms many reported TOPCon structures in the literature, which typically range between 23–26% [2, 6–8]. Consequently, compared to existing TOPCon approaches, the practical difference of the model lies in integration of MgF_2/ITO/AZO/ITO ARCs and rear albedo effects with a bifacial operation, allowing for simultaneous enhancement of optical and electrical performance. This research reinforces the potential of MgF_2-enhanced bifacial TOPCon solar cells as a viable and efficient solution for next-generation photovoltaic technologies.

It is important to note, however, that our simulations have some limitations. The optical modeling in OPAL 2 considered only the front-side texture and assumed an idealized Lambertian rear reflector, while SCOUT assumed planar, continuous layers. Electrically, Quokka 3 operates in 2D and does not capture all 3D carrier transport effects. Furthermore, all simulations assumed ideal interfaces and material properties; real-world fabrication imperfections may lead to slightly lower performance. Experimental verification of the simulated structures is therefore needed, including MgF_2-coated bifacial TOPCon cells, to confirm the simulation result

4. Conclusions

In conclusion, this study presents a comprehensive simulation-based investigation of bifacial TOPCon solar cells, with modeling conducted using Quokka 3 software. The structural design and optical characteristics of these cells were thoroughly examined with the aid of OPAL 2 and SCOUT softwares, enabling precise analysis of light behavior and internal device parameters. A key focus was placed on evaluating various ARC configurations, specifically triple-layered ITO-AZO-ITO structures, both with and without the inclusion of an MgF_2 top layer. It was found that the refractive index of MgF_2 is suitable for reducing reflection from TOPCon solar cells with ITO/AZO/ITO transparent electrode. The optical modeling revealed that the integration of an MgF_2 layer on top of the ARC significantly enhances the optical response of the solar cell by achieving lower and more uniform reflectance across the spectrum under investigation with a noticeable decrease between 600-700 nm. This improvement in light management leads to better photon absorption, ultimately translating into enhanced electrical performance. The optimized structure demonstrated a measurable gain in EQE. Furthermore, the addition of MgF_2 effectively redirects previously reflected light into the active layer, enhancing useful absorption. As a result, a significant decline in J_R from 5.44 to 3.38 mA/cm² was observed, leading to improved J_{PA} and J_{Abulk} values. Further analysis focused on the impact of rear-side illumination, modeled through varying rear albedo conditions. Back reflection from the rear Ag electrode was found to be negligible. It has been established that at 0 suns albedo, PCE of bifacial solar cells was only slightly lower than of solar cells

with Ag back (20.56 to 20.94% respectively) and this trend was similar for both structures with and without MgF_2 ARC. Results indicated that increasing the albedo positively influences key electrical parameters of the *J-V* curve, notably the J_{sc} and PCE with V_{oc} slightly changing from 0.73 to 0.74. The highest efficiency, recorded at 27.37%, was achieved under a rear albedo of 0.3 when the cell incorporated the MgF_2-enhanced ARC structure. This highlights the critical role of rear-side reflectivity in bifacial solar cell performance, emphasizing the importance of optimizing both front and rear interfaces. Additionally, the computer simulation highlights the need for future experimental validation of the proposed structures, given their outstanding simulated performance.

Acknowledgements. The research was funded by the Science Committee of the Ministry of Science and Higher Education of the Republic of Kazakhstan (Grant No. AP19680267).

References

1. Rohatgi A., Rounsaville B., Ok Y. W., Tam A. M., Zimbardi F., Upadhyaya A. D., Tao Y., Madani K., Richter A., Benick J., Hermle M. Fabrication and modeling of high-efficiency front junction n-type silicon solar cells with tunnel oxide passivating back contact // IEEE Journal of Photovoltaics. – 2017. – Vol. 7. – Pp. 1236–1243. https://doi.org/10.1109/JPHOTOV.2017.2715720

2. Feldmann F., Reichel C., Müller R., Hermle M. The application of poly-Si/SiOx contacts as passivated top/rear contacts in Si solar cells // Solar Energy Materials and Solar Cells. – 2017. – Vol. 159. – Pp. 265–271. https://doi.org/10.1016/j.solmat.2016.09.015

3. Ullah H., Czapp S., Szultka S., Tariq H., Qasim U. Bin, Imran H. Crystalline silicon (c-Si) based tunnel oxide passivated contact (TOPCon) solar cells: A review // Energies. – 2023. – Vol. 16. – Art. 715. https://doi.org/10.3390/en16020715

4. Römer U., Peibst R., Ohrdes T., Lim B., Krügener J., Wietler T., Brendel R. Ion implantation for poly-Si passivated back-junction back-contacted solar cells // IEEE Journal of Photovoltaics. – 2015. – Vol. 5. – Pp. 507–514. https://doi.org/10.1109/JPHOTOV.2014.2382975

5. Peibst R., Römer U., Larionova Y., Rienäcker M., Merkle A., Folchert N., Reiter S., Turcu M., Min B., Krügener J., Tetzlaff D., Bugiel E., Wietler T., Brendel R. Working principle of carrier selective poly-Si/c-Si junctions: Is tunnelling the whole story? // Solar Energy Materials and Solar Cells. – 2016. – Vol. 158. – Pp. 60–67. https://doi.org/10.1016/j.solmat.2016.05.045

6. Wang Q., Peng H., Gu S., Guo K., Wu W., Li B., Li L., Yuan N., Ding J. High-efficiency n-TOPCon bifacial solar cells with selective poly-Si based passivating contacts // Solar Energy Materials and Solar Cells. – 2023. – Vol. 259. – Art. 112458. https://doi.org/10.1016/j.solmat.2023.112458

7. Wu W., Jolywood J. B., Bao J., Ma L., Chen C., Liu R., Qiao Z., Chen J., Liu Z. Development of industrial n-type bifacial TOPCon solar cells and modules // 37th European Photovoltaic Solar Energy Conference and Exhibition. – 2019. – Pp. 100–102. https://doi.org/10.4229/EUPVSEC20192019-2BP.1.5

8. Chen Y., Chen D., Liu C., Wang Z., Zou Y., He Y., Wang Y., Yuan L., Gong J., Lin W., Zhang X., Yang Y., Shen H., Feng Z., Altermatt P. P., Verlinden P. J. Mass production of industrial tunnel oxide passivated contacts (i-TOPCon) silicon solar cells with average efficiency over 23% and modules over 345 W // Progress in Photovoltaics: Research and Applications. – 2019. – Vol. 27. – Pp. 827–834. https://doi.org/10.1002/pip.3180

9. Jain A., Choi W. J., Huang Y. Y., Klein B., Rohatgi A. Design, optimization, and in-depth understanding of front and rear junction screen-printed double-side passivated contacts solar cells // Conference Record of the IEEE Photovoltaic Specialists Conference. – 2020. – Pp. 1339–1343. https://doi.org/10.1109/PVSC45281.2020.9300805

10. Kotak B., Eng Y., Gul BEng M. S., Muneer T., Ivanova S. Investigating the impact of ground albedo on the performance of PV systems // CIBSE Technical Symposium, London, UK, April 16-17, 2015. https://researchportal.hw.ac.uk/en/publications/investigating-the-impact-of-ground-albedo-on-the-performance-of-p/ (available on December 17, 2025).

11. Fell A., Altermatt P. P. A detailed full-cell model of a 2018 commercial PERC solar cell in Quokka3 // IEEE Journal of Photovoltaics. – 2018. – Vol. 8. – P. 1443–1448. https://doi.org/10.1109/JPHOTOV.2018.2863548

12. Kowsar A., Debnath S. C., Shafayet-Ul-Islam Md., Hossain M. J., Hossain M., Chowdhury A. K., Hashmi G., Farhad S. F. U. An overview of solar cell simulation tools // Solar Energy Advances. – 2025. – Vol. 5. – Art. 100077. https://doi.org/10.1016/j.seja.2024.100077

13. Solodovnik A., Kleksin R., Leontyev P., Useinov B., Markova A., Kassimova S. Revealing the noctilucent cloud fields structure by software processing of satellite images // Physical Sciences and Technology. – 2025. – Vol. 12. – Pp. 4–13. https://doi.org/10.26577/phst20251211

14. Vorobyova O., Sokolov D., Korshikov Y. Modeling of thermal distribution on cryosurface for low temperatures // Physical Sciences and Technology. – 2025. – Vol. 12. – No. 1–2. – Pp. 115–120. https://doi.org/10.26577/phst202512111

15. Kemelbekova A., Lebedev I. A., Grushevskaya E. A., Murzalinov D. O., Fedosimova A. I., Kemelbekova A. E., Kazhiev Zh. Sh., Zhaysanbayev Zh. K., Temiraliyev A. T. The effect of deposition technique on formation of transparent conductive coatings of SnO_2 // Physical Sciences and Technology. – 2022. – Vol. 9. – Pp. 37–44. https://doi.org/10.26577/phst.2022.v9.i1.05

16. Chavan G. T., Kim Y., Khokhar M. Q., Hussain S. Q., Cho E.-C., Yi J., Ahmad Z., Rosaiah P., Jeon C.-W. A brief review of transparent conducting oxides (TCO): the influence of different deposition techniques on the efficiency of solar cells // Nanomaterials. – 2023. – Vol. 13. – No. 7. – Art. 1226. https://doi.org/10.3390/nano13071226

17. Grübel B., Nagel H., Steinhauser B., Feldmann F., Kluska S., Hermle M. Influence of plasma-enhanced chemical vapor deposition poly-Si layer thickness on the wrap-around and the quantum efficiency of bifacial n-TOPCon solar cells // Physica Status Solidi (A) Applications and Materials Science. – 2021. – Vol. 218. – Art. 2100156. https://doi.org/10.1002/pssa.202100156

18. Yan X., Suhaimi F. Bin, Xu M., Yang J., Zhang X., Wang Q., Jin H., Shanmugam V., Duttagupta S. Development of ultra-thin doped poly-Si via LPCVD and ex-situ tube diffusion for passivated contact solar cell applications // Solar Energy Materials and Solar Cells. – 2020. – Vol. 209. – Art. 110458. https://doi.org/10.1016/j.solmat.2020.110458

19. Ditsougou J., Desrues T., Kaminski A., Dubois S. Optimization of poly-Si/SiOx passivated contacts for crystalline silicon bottom cells applications // SiliconPV Conference Proceedings. – 2025. – Vol. 2. https://doi.org/10.52825/siliconpv.v2i.1310

20. McIntosh K. R., Baker-Finch S. C. OPAL 2: Rapid optical simulation of silicon solar cells // 38th IEEE Photovoltaic Specialists Conference. – 2012. – Pp. 000265–000271. https://doi.org/10.1109/PVSC.2012.6317616

21. Theiss W. Hard- and software for optical spectroscopy. – Available at: https://www.wtheiss.com/ (available on December 15, 2025).

22. Nussupov K. K., Beisenkhanov N. B., Kusainova A. Z., Shynybayev D. S., Zhirkov I. V., Sultanov A. T. Influence of the RF magnetron sputtering power on the optical and electrical properties of AZO films // Physical Sciences and Technology. – 2023. – Vol. 10. – No. 2. – Pp. 28–32. https://doi.org/10.26577/phst.2023.v10.i2.03

23. Rakhimova A. Zh., Zhirkov I. V., Nussupov K. Kh., Beisenkhanov N. B., Sultanov A. T. Effect of oxygen flow on electrical and optical properties of ITO films synthesized by magnetron sputtering method // Herald of the Kazakh-British Technical University. – 2023. – Vol. 20. – P. 109–117. https://doi.org/10.55452/1998-6688-2023-20-4-109-117

24. Siqueiros J. M., Machorro R., Regalado L. E. Determination of the optical constants of MgF_2 and ZnS from spectrophotometric measurements and the classical oscillator method // Applied Optics. – 1988. – Vol. 27. – Pp. 2549–2553. https://doi.org/10.1364/AO.27.002549

25. Sultanov A., Zhirkov I., Nussupov K., Kusainova A., Abdyldayeva N., Beisenkhanov N. Investigation on optical and electrical properties of multilayer ITO/AZO/ITO transparent conductive oxides // Optical Materials. – 2024. – Vol. 155. – Art. 115850. https://doi.org/10.1016/j.optmat.2024.115850

26. Raut H. K., Ganesh V. A., Nair A. S., Ramakrishna S. Anti-reflective coatings: A critical, in-depth review // Energy and Environmental Science. – 2011. – Vol. 4. – Pp. 3779–3804. https://doi.org/10.1039/C1EE01297E

27. Sultanov A., Mussakhanuly N., Kusainova A., Parkhomenko H. P., Yerlanuly Y., Nussupov K., Ng A., Beisenkhanov N., Jumabekov A. N. Utilizing MoOx-Au-MoOx trilayers as transparent top electrodes in 2-terminal monolithic Si/perovskite tandem solar cells // Applied Physics A: Materials Science and Processing. – 2025. – Vol. 131. – Pp. 1–10. https://doi.org/10.1007/s00339-025-08425-x

Information about authors:

Zhirkov Ilya – Junior Researcher at the "Laboratory of Alternative Energy and Nanotechnology", Master Student at the Kazakh-British Technical University (Almaty, Kazakhstan, e-mail: il_zhirkov@kbtu.kz).

Suleimenova Aiganym – Lab Assistant at the "Laboratory of Alternative Energy and Nanotechnology", Bachelor student at the Kazakh-British Technical University (Almaty, Kazakhstan, e-mail: aiga_suleimenova@kbtu.kz).

Sultanov Asanali – PhD student at the Kazakh-British Technical University, Head of "Laboratory of Alternative Energy and Nanotechnology" at the Kazakh-British Technical University (Almaty, Kazakhstan, e-mail: a.sultanov@kbtu.kz).

Beisenkhanov Nurzhan – Doctor of Physical and Mathematical Sciences, Professor, Member of AAAS and ACS, Chief Researcher, Dean of SMS&GT at the Kazakh-British Technical University (Almaty, Kazakhstan, e-mail: n.beisenkhanov@kbtu.kz).

CONTENTS